Aero-propulsive performance analysis of fuselage for boundary layer ingestion

Pradeep Baskaran

Technische Universiteit Delft

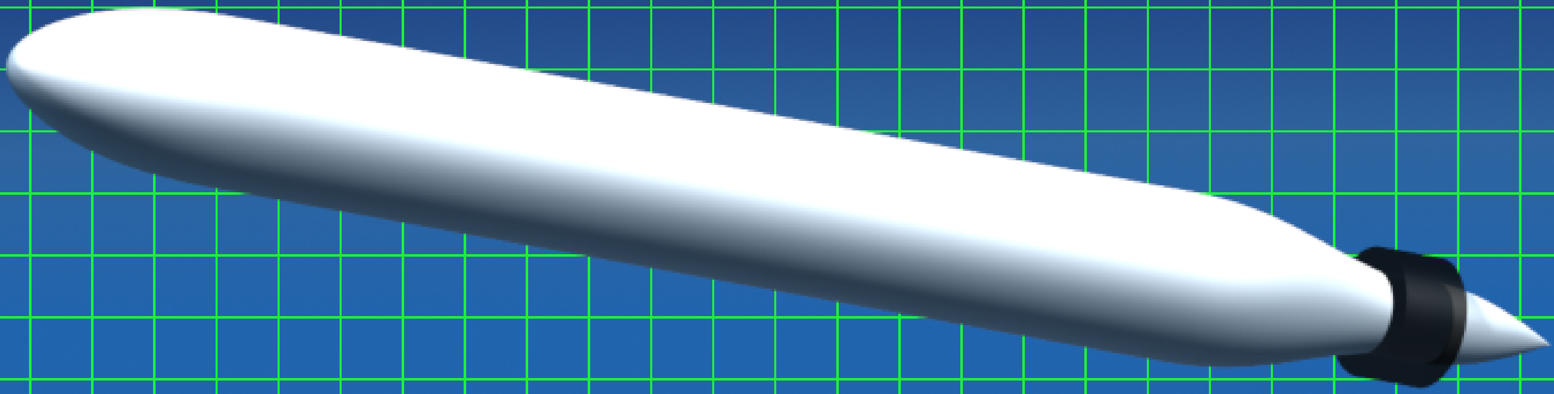

Delft University of Technology

Challenge the future

AERO-PROPULSIVE PERFORMANCE ANALYSIS OF FUSELAGE FOR BOUNDARY LAYER INGESTION

by

Pradeep Baskaran

in partial fulfillment of the requirements for the degree of

Master of Science
in Aerospace Engineering

at the Delft University of Technology,
to be defended publicly on Thursday May 9, 2019 at 1:30 PM.

Student number:	4622499	
Supervisor:	Dr. A.G. Rao,	TU Delft
Thesis committee:	Dr. A.G. Rao,	TU Delft
	Prof. dr. ir. L.L.M. Veldhuis,	TU Delft
	Dr. B.W. van Oudheusden,	TU Delft
	Ir. B. Della Corte,	TU Delft

An electronic version of this thesis is available at http://repository.tudelft.nl/.

Delft
University of
Technology

PREFACE

"*If I have seen further, it is by standing on the shoulders of giants*" are the famous words of Sir Isaac Newton which clearly applies to any research work. Thus, I feel it is imperative to first express my sincere gratitude to all the authors of previous studies without which the present work would not have been possible. Next, I would like to thank Dr.Arvind Gangoli Rao for his patience and guidance during the project. Further, I would like to thank and appreciate the continuous feedback, suggestions, and tips provided by Martijn van Sluis and Biagio Della Corte during the weekly meetings. Last but not least, it is important to give my heartfelt thanks to my parents without whose cooperation, patience, and support, I would have never made it this far.

Pradeep Baskaran
Delft, April 2019

CONTENTS

ACRONYMS

ASO	Aerodynamic shape optimization
AWF	Approximate wake/boundary layer filler
BLI	Boundary layer ingestion/ingesting depending on context
BOR	Body of revolution
BP	Boundary around propulsor
BS	Body surface
CFD	Computational fluid dynamics
CL	Cylinder (refers to a part of the fuselage afterbody)
CV	Control volume
DSE	Design space exploration
EAM	Exergy analysis method
EI	Euler-IBLT flow (refers to the flow field model)
ES	Exit section (refers to a part of the fuselage afterbody)
IBLT	Integral boundary layer theory
ISA	International standard atmosphere
LE	Leading edge
LP	Leading plane
LS	Leading section (refers to a part of the fuselage afterbody)
PBM	Power balance method
PFC	Propulsive fuselage concept
PSC	Power saving coefficient
RANS	Reynolds averaged Navier-Stokes
RVF	Real viscous flow
SP	Side plane
SS	Side surface
TE	Trailing edge
TFP	Trefftz plane
TP	Test plane
UDF	User defined function
WI	Wake ingestion

SYMBOLS

B	Number of blades (as defined for MTFLOW)
b	Local effective body circumference (including the displacement thickness)
$()_{Base}$	Baseline value
C_D	Overall drag coefficient = $\left(=\frac{D}{\frac{1}{2}\rho_\infty V_\infty^2 S_{ref}}\right)$
$C_{\dot{A}S}$	Overall body surface anergy rate coefficient $\left(=\frac{\dot{A}_S}{\rho V_\infty^3 S_{ref}}\right)$(a different nomalization used in the accompanying paper in AIAA journal gives double the value)
C_f	Local friction coefficient $\left(=\frac{\tau_{wall}}{\frac{1}{2}\rho_e V_e^2}\right)$
C_{F_x}	Net x-force coefficient $\left(=\frac{10^4\times F_x}{\frac{1}{2}\rho_\infty V_\infty^2 S_{ref}}\right)$
C_P	Propulsor power coefficient $\left(=\frac{P}{\rho V_\infty^3 S_{ref}}\right)$(a different nomalization used in the accompanying paper in AIAA journal gives double the value)
C_Φ	Local viscous dissipation coefficient $\left(=\frac{\mathscr{D}}{\rho_e V_e^3}\right)$
$C_{\Phi S}$	Overall body surface viscous dissipation coefficient $\left(=\frac{\Phi_S}{\rho V_\infty^3 S_{ref}}\right)$(a different nomalization used in the accompanying paper in AIAA journal gives double the value)
D	Drag or diameter depending on context
δ	Boundary layer thickness or variable uncertainty depending on context
δ^*	Boundary layer displacement thickness
δ^{**}	Boundary layer density-flux thickness $\left(=\frac{1}{\rho_e u_e}\int_0^{y_e}(\rho_e-\rho)u_n.dy_n\right)$
$\dot{A}$	Anergy rate
$\dot{A}_\Phi$	Anergy rate due to viscous heating
$\dot{A}_{thm}$	Thermal mixing Anergy rate
$\dot{E}$	Mechanical energy deposition rate (PBM or EAM)
$\dot{E}_a$	Axial kinetic energy deposition rate (PBM or EAM)
$\dot{E}_p$	Pressure defect energy deposition rate (PBM or EAM)
$\dot{E}_{th}$	Thermal energy deposition rate (EAM)
$\dot{E}_v$	Transverse kinetic energy deposition rate (PBM or EAM)
$\dot{\varepsilon}$	Exergy deposition rate (EAM)
$\dot{\varepsilon}_m$	Mechanical exergy deposition rate (EAM)
$\dot{\varepsilon}_p$	Exergy supply rate of propulsor (EAM)
$\dot{\varepsilon}_\Phi$	Exergy deposition rate due to viscous heating (EAM)
$\dot{\varepsilon}_{th}$	Thermal exergy deposition rate (EAM)

e	Internal energy
$()_e$	Boundary layer edge quantity
η	Efficiency
$()_{EI}$	Euler-IBLT quantity
$()_\infty$	Freestream quantity
F_x	Net x-force
H	Boundary layer shape parameter $= \frac{\delta^*}{\theta}$
h	Enthalpy
H_k	Boundary layer kinematic shape parameter
H^*	Boundary layer kinetic energy shape parameter $= \frac{\theta^*}{\theta}$
H^{**}	Boundary layer density-flux shape parameter $= \frac{\theta^{**}}{\theta}$
$()_{iso}$	Isolated simulation result
L	Length
M	Mach number
$\dot{m}$	Fluid mass flow rate
$\mid \vec{V} \mid$	Meridional velocity $= \sqrt{u^2 + v^2}$
μ	Effective dynamic viscosity
μ_l	Laminar dynamic viscosity
μ_t	Turbulent dynamic viscosity
$()_n$	Boundary layer tangential and normal quantities
ν	Dynamic viscosity
$()_{Optim}$	Optimizer result
P	Power
p	Static pressure
Φ	Viscous dissipation
P_K	Propulsor power term (PBM or EAM)
$()_{ple}$	Propulsor leading edge value
$()_{prop}$	BLI simulation result
P_S	Propulsor power term (PBM or EAM)
P_V	Pressure-volume power term (PBM or EAM)
Q	Some quantity (will be made clear in the respective context)
R, r	Radius
Re	Reynolds number
$()_{ref}$	Reference quantity
ρ	Fluid mass density
$()_{RVF}$	Real viscous flow quantity
$rxxx$	Propulsor radius with percentage size with respect to fuselage radius. r100 for example means that the propulsor radius is equal to (100%) the fuselage radius.

S	Area
s	Entropy
$\bar{\bar{\tau}}$	Complete shear stress tensor
$()_{surf}$	Overall surface value
T	Thrust or Static temperature depending on context
t	Time variable
θ	Boundary layer momentum thickness
θ^*	Boundary layer kinetic energy thickness
$()_0$	Stagnation quantity
T_θ	Circumferential blade Thickness
u	Global axial (or local streamwise in case of boundary layer formulations) velocity
v	Global transverse (or local normal in case of boundary layer formulations) velocity
V	Velocity magnitude
ϑ	Volume
V_θ	Swirl velocity
$\vec{V}$	Velocity vector
X	Design vector
X_0	Initial design vector
x, y, z	Cartesian coordinates

LIST OF FIGURES

LIST OF TABLES

ABSTRACT

Keywords: Boundary layer ingestion, power balance method, exergy analysis method, surface dissipation, surface anergy rate

Aircraft fuel efficiency, noise, and emissions are some of the most important aspects being addressed in the research of novel aircraft configurations for meeting the future requirements of the aviation industry. One concept which has the potential for improving the aircraft fuel efficiency is called the boundary layer ingestion (BLI). Modification of the boundary layer flow using a power supply for favorable aerodynamic and/or propulsive effect, in general, could be called boundary layer ingestion. This method is especially possible when a propulsor is tightly integrated with the airframe which allows the partial recovery of power which is otherwise lost in the wake flows. A tube-wing aircraft fuselage with a boundary layer ingesting propulsor in the aft is a good candidate for the study as the fuselage is the body with the highest length in the streamwise direction resulting in a large potential for power recovery.

The present work involves the numerical assessment of the aero-propulsive performance of tube-wing aircraft fuselage with a boundary layer ingesting propulsor in the aft. This consists of the use of computational fluid dynamics with power balance [1] and exergy analysis [2] methods to analyze the various aspects of the flow in BLI configurations. The study focuses importantly on the design space exploration for analyzing the effect of axisymmetric fuselage geometry and flight conditions on propulsor (modeled as an actuator volume) power consumption. The effect of aircraft wings, propulsor blades, propulsor nacelle, and empennage are not included in the present study. The results are driven more towards understanding the effect of fuselage design on BLI especially in transonic flights. The exploration is followed by constrained design optimization of axisymmetric fuselage geometry for obtaining least fuel burn.

The most important conclusions that can be drawn include the fact that the fuselage surface dissipation (already known from literature) and surface anergy rate are not sensitive to the static pressure changes caused by the BLI propulsor for the wide range of fuselage designs and flight conditions considered. Thus, the power consumed by the BLI propulsor shows the same changes (with respect to a baseline fuselage geometry and flight condition) as the isolated fuselage surface dissipation and anergy rate. Also, the power saving due to BLI when compared to that of the ideal freestream ingesting propulsor shows only minor changes when compared to the changes in fuselage surface dissipation, fuselage surface anergy rate, and BLI propulsor power consumption for different fuselage designs (or flight conditions). These effectively make the isolated body drag analysis suitable for qualitative performance evaluation of fuselage even for BLI applications. Further, these also reduce the BLI fuselage configuration optimization problem to a simple isolated body aerodynamic shape optimization problem.

1

INTRODUCTION

There is a constant effort in the aviation sector to reduce the aircraft fuel burn. Noise and emissions are also an important aspect of aircraft design. Ambitious goals set in the previous decade includes the NASA N+3 program which aims 70% fuel burn, 75% Landing and take-off NOx emission and 71 dB noise reductions by 2035 [3]. Also, targets set by Advisory Council for Aeronautical Research in Europe (ACARE) aim for a CO2 emissions reduction of 75% by 2050 [4]. Novel designs are required to achieve these goals. Various new technologies are being investigated (for example in the NASA N+3 program) and BLI is one among the many which is relevant for reducing the fuel consumption. A quality development function (figure 1.1) for the N+3 propulsion technology clarifies the existence of a strong relationship between aircraft power consumption and BLI (figure 1.1).

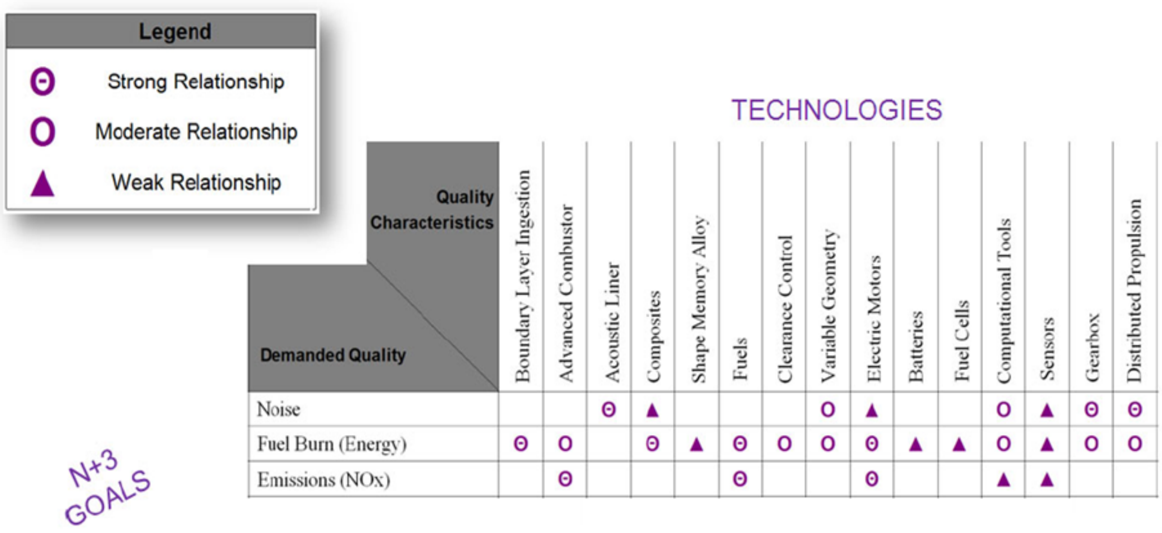

Legend

ʘ Strong Relationship

O Moderate Relationship

▲ Weak Relationship

TECHNOLOGIES

Quality Characteristics / Demanded Quality	Boundary Layer Ingestion	Advanced Combustor	Acoustic Liner	Composites	Shape Memory Alloy	Fuels	Clearance Control	Variable Geometry	Electric Motors	Batteries	Fuel Cells	Computational Tools	Sensors	Gearbox	Distributed Propulsion
Noise			ʘ	▲				O	▲			O	▲	ʘ	ʘ
Fuel Burn (Energy)	ʘ	O		ʘ	▲	ʘ	O	O	ʘ	▲	▲	O	▲	O	O
Emissions (NOx)		ʘ				ʘ			ʘ			▲	▲		

N+3 GOALS

Figure 1.1: Quality development function for N+3 propulsion technology. Reproduced from [3].

One concept which is widely used in marine propulsion for reducing fuel burn is wake ingestion [5]. In the context of tightly integrated propulsion system, wake ingestion (WI) refers to the ingestion of the wake flow from a body by a propulsor. Boundary layer ingestion (BLI), on the other hand, refers to the ingestion of the boundary layer flow from a body. A point of consideration is the static pressure at the location of ingestion. Usually, for a body in general, the static pressure very close to the body trailing edge is not equal to the free stream static pressure (unless no pressure gradient exists). This is usually the case for Boundary layer ingestion.

The possible benefits of BLI/WI can probably be exploited provided the different challenges associated with the actual implementation of the concepts to aircraft are addressed. The benefits and challenges associated with BLI/WI for aircraft are listed next.

Benefits of BLI and WI can be divided into aero-propulsive (engine) benefits and aircraft level benefits. These benefits are listed next:

- Aero-propulsive benefits including the reduced power consumption due to ingestion of energized flow (wake or boundary layer) resulting in reduced airframe and jet mixing loses, and the possible reduction in drag due to the reduced wetted area [6].
- Aircraft level benefits include possible total weight reduction due to the smaller size of a more efficient propulsor, and possibly smaller yaw control surfaces and vertical stabilizers due to closer spacing of propulsor and fuselage symmetry plane.
- Finally, emissions reduction due to reduced fuel burn, and external noise reduction [3] due to the embedding of the engine in some cases are the other possible benefits.

Important limitations which are required to be addressed are:

- Distortion of flow at the propulsor entry which can lead to unwanted stresses on the propulsor fan or other components [3].
- Acoustic problems due to a possible increase in the cabin noise. It should be noted that embedding the propulsor results in the airframe shielding the noise of the propulsor from propagating outside but the cabin noise, on the other hand, is bound to increase [3].
- Off-design propulsor operation also needs consideration. Power saving can mainly be achieved during cruise which is usually the longest phase during any flight. Due to distortion of flow during different flight phases like cruise, take-off or landing (mainly due to different angle of attack and swirl) the propulsor design must be done carefully.
- Interference drag (due to the close spacing of engine nacelle and fuselage) and possibly increased drag due to airframe-propulsor interaction (although this may not have a deteriorating effect as will be understood in the later part of the thesis).
- Another issue to address in case the BLI propulsor is installed at the aft of a tube fuselage is the ground clearance during takeoff.

1.1. STATE OF ART

The theoretical development of BLI for aerospace application starts with the work on wake ingestion by Smith [5]. It should be noted that the concept of boundary layer ingestion already existed in the analysis of marine technology [5]. The method by Smith [5] gives a basic theoretical outline in which the wake parameters are related to the power benefit of a wake ingesting propulsor. Next, it can be found that the most important theoretical background that can be used for analyzing tightly integrated propulsion systems is the power balance method by Drela [1] which clarifies certain important unanswered issues that existed in the literature before it. Drela [1] creates a framework involving mechanical energy analysis which can be applied to analyze tightly integrated configurations. The extension of Drela's work to include thermal management for tightly integrated configurations was presented by Arntz et al. [2] using an exergy based formulation.

Literature, in general, describes different phenomena which can affect BLI/WI configurations. These include the increase in airframe drag due to the coupling effect of tightly integrated propulsors [7], flow distortion and the presence of shock waves [8]. Out of these, flow distortion is more in the spotlight in the literature as it is an important challenge [3] that needs to be addressed before BLI is possibly implemented in aircraft. A clear understanding of the mechanism of the flow modification due to the presence of the propulsor becomes necessary. Like for example, a mechanism for airframe drag rise is suggested by Lv. and Rao [7]. The power balance method (PBM) does shed some light on the power flow and viscous dissipation involved in such configuration.

The experimental methods covered in previous work serve as a proof of concept for the possible power benefit of BLI/WI configurations. These methods have been evolving and the use of PBM can also be found.

PIV based analysis is a recent development [9]. Though the use of the power balance method involving the calculation of specific integrals could result in different uncertainties and the error propagation which should be more carefully addressed. The development of D8 double bubble aircraft also showed some promising power saving results during the experimental investigations [10]. Further, Carrier et al. [11] validate a CFD code using an experimental setup. Sabo and Drela [12] present an experimental power saving analysis involving a NACA0040 BOR. Just to give an example, the work by Sabo and Drela [12] and the work by Carrier et al. [11] present a power saving of close to 25 % for the subsonic (for null net force or cruise condition) conditions considered in the respective work. The power saving metric used in [12] and [11] are quite like the PSC_{actual} described in section 2.2.

The CFD analyses cover the important aero-propulsive effects involved in BLI/WI systems. They also discuss some methods to perform optimizations and sensitivity analysis on computationally intensive frameworks like RANS CFD [13]. One of the work presents a very high power saving, which is the analysis of three different configurations by Elmilgui et al. [14] (but ≈ 85% power saving for whatever configuration is still questionable). Bluementhal et al. [15] on the other hand present a reverse engineering strategy to optimize the fuselage geometry by changing the pressure fields and adapting the physical geometry accordingly. The modeling of the configurations in the literature range from axisymmetric fuselage models with steady flow [14] to 3D steady flow models [16] and unsteady flow model [15] including wings. Kenway and Kiris [16] address the flow distortion issues by optimizing the fuselage geometry in a 3D RANS simulation. Gray et al. [13] on the other hand address the aero-propulsive coupling using a sensitivity analysis of an actuator disk pressure ratio modeled to represent a fan at the end of a fuselage. Further, the parameterization of axisymmetric fuselage geometries could be done with the help of work from ESDU document 77028 [17] and the work by Pettruson [18] on ultra high bypass ratio aircraft engine design also provides some parameterization techniques for nacelles and axisymmetric fuselages (including BLI cases). Further, it can be observed that different organizations have come up with different concept aircraft for the study of such BLI configurations. Some of these concept aircraft are D8 double bubble (MIT and NASA), STARC-ABL (NASA), Propulsive fuselage concept or PFC (Bahaus Luftfahrt).

1.2. MOTIVATION AND RESEARCH DEFINITION

It can be seen from figure 1.1 that BLI is a potential technology to reduce fuel consumption in transport flights. Thus, the investigation of the novel technology for specific details becomes necessary. Also, in the literature, certain contemporary theoretical methods used to analyze such configurations are mentioned. The most important are the work by Drela [1] on power balance analysis, and the work by Arntz et al. [2] on exergy analysis. The application of these methods to CFD frameworks, of course, may be specific to the type of solver under consideration. For example, Arntz and Atinault present an application of the exergy analysis method (EAM) to a blended wing body configuration using a CFD framework in [19]. Carrier et al. [11] also present a work in which an attempt is made to validate a CFD based analysis using experimental investigations. Drela, on the other hand, pioneered the use of mechanical energy based numerical analysis. For example, the power balance method (PBM) can be argued to be inherently introduced into the 2D-boundary layer equations in the Euler-IBLT CFD solver method described in [20]. This method is further extended for application to axisymmetric bodies in the MTFLOW [21] application. These theoretical methods must be carefully adapted for different solvers and their differences may be pointed out to ease the future research.

The next important aspect to consider is the application of BLI to the different surfaces of the aircraft. The aerodynamic surface to be used depends on the aircraft configuration. Tube-wing aircraft have become a recent research subject. Examples of these include the NASA STARC-ABL and the propulsive fuselage concept by Bahaus Luftfahrt. It is, of course, understandable that lesser modifications to the existing aircraft could result in an economical and quick implementation of the novel concept of BLI to transport aircraft. Thus, tube-wing aircraft configurations constitute an ideal setup. Also since fuselage is the longest aerodynamic body (in the streamwise direction) resulting in the highest loss of power in the wake flow, it naturally becomes the most important aerodynamic body which can be considered for BLI application. Isikveren et al. [23] discuss the work performed within the Distributed Propulsion and Ultra-high By-Pass Rotor Study at Aircraft Level project (called DisPURSAL) funded by the European Commission. The propulsive fuselage concept (PFC) is one of the designs considered in this work. It was found using an extensive conceptual analysis that the aircraft configuration using smaller (compared to the present transport aircraft) freestream ingesting under-wing engines supported by a BLI engine installed in the aft of the fuselage is one of the best possible setups (in terms of different criteria whose details can be found in [22]). The present thesis would anyways consider a BLI engine operating independently in the aft of the fuselage for simplicity.

Since the fuselage of the aircraft is identified to be the most important aerodynamic body for BLI in a tube-wing aircraft configuration, its design may need to be extensively studied. Although some previous work like that of Elmilgui et al. [14], Bluementhal et al. [15], Kenway and Kiris [16], Gray et al. [13] etc. have addressed this to some extent, a more detailed analysis focusing on the use of the contemporary theoretical methods through a CFD framework would be very useful. Thus, the following research objective could be stated:

The main objective of the research is to investigate the aerodynamic effect of the design of a fuselage with boundary layer ingesting propulsor in the aft on power consumption by performing a numerical study using computational fluid dynamics (CFD) with power balance and exergy analysis methods to perform a design space exploration and a design optimization.

The fulfillment of this main objective requires the fulfillment of the following goals with sub-goals:

- Develop a clear understanding of the application of the power balance and exergy analysis methods through a CFD framework.
    - Power balance and exergy analysis of chosen cases.
    - Error propagation analysis.
- Design space exploration and optimization using low-fidelity solver (using power balance method).
    - Unconstrained analysis of axisymmetric isolated body and BLI configuration using Euler-IBLT solver for different fuselage designs and flight conditions.
    - Constrained optimization of axisymmetric fuselage geometry using Euler-IBLT solver for BLI application.
- Verification and filling the gaps using a higher fidelity method (power balance and exergy analysis).
    - Verification of important results from the Euler-IBLT solver using RANS solver.
    - Comparison of results from power balance and exergy methods.

1.3. THESIS OUTLINE

The present thesis involves the numerical study of BLI applied to aircraft tube fuselage. The analysis of the novel concept is done using the contemporary theoretical methods applied to CFD.

The present thesis is divided into six chapters. Starting with the research definition in the present chapter, the theoretical concepts (PBM and EAM) are introduced in chapter 2. These include the theories required to study BLI and the important ones necessary to understand the CFD flow solvers.

Further, chapter 3 consists of the application of PBM and EAM to different CFD cases. A clear understanding of the behavior of the theoretical methods in different CFD setups is developed. This includes the identification of the possible errors. In the same section, the results from the low (Euler-IBLT) and high (RANS) fidelity solvers are compared for important cases. Finally, the baseline Fuselage design (and flight conditions) to be used in chapter 4 for design space exploration study is defined. It should be noted that BLI studies involve both isolated body (no propulsor or uninstalled configuration) and installed configuration (the BLI configuration) studies.

Next, chapter 4 consists of the design space exploration to study the effect of fuselage design (and flight conditions) on BLI. This is done by selecting various geometric parameters for the fuselage (like after body shape and slenderness) and studying their effect for BLI. Flight conditions (like flight speed and altitude) are also considered. The isolated body and BLI configuration simulations are performed using the Euler-IBLT solver (where PBM is used for obtaining performance metrics). The Euler-IBLT results are supplemented with RANS (with both PBM and EAM) simulation results (for verifying some cases for each parameter depending on the necessity). Finally, in chapter 5, the fuselage geometry is optimized with BLI considerations. The main observations, conclusions, and recommendations for future work are presented in chapter 6.

2

THEORETICAL BACKGROUND

2.1. THE BLI POWER BENEFIT

The power benefit of BLI can be understood to be due to two reasons. One, the wake flow is energized back closer to the freestream value which prevents the loss in wake flow of a body. Second, since the propulsor jet becomes the energized flow from the body wake, the jet speed is lower (and closer to freestream) reducing the power loss (in the jet). In an ideal case, the BLI propulsor must completely restore the body wake flow to the freestream value. This means that the body wake and propulsor jet loss will be null. This is represented in figure 2.1.

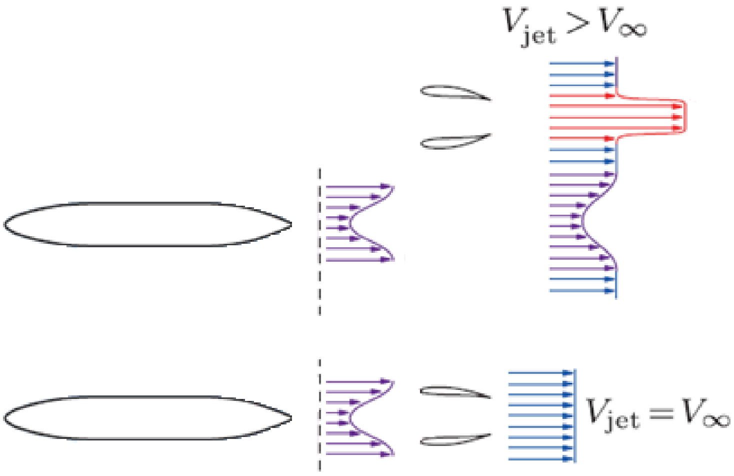

Figure 2.1: Ideal BLI effect. Adapted from [6].

2.2. PERFORMANCE METRIC

The concepts of BLI and WI as mentioned earlier have been researched for the application in marine propulsion [5]. These concepts have been mentioned in the literature to have power saving benefits [9, 10, 12] when compared with conventional configurations in which propulsors ingest the freestream flow. Thus, a metric to quantify this benefit becomes important.

The tightly integrated configurations involving BLI/WI result in certain confusion when the classic performance metric of Froude's efficiency is used. The quantification of power benefit has been controversial in the literature. Froude's propulsive efficiency value can be observed to exceed unity [7]. Froude's efficiency can be given as:

$$\eta_{propulsive} = \frac{TV_\infty}{P_{propulsor}} , \tag{2.1}$$

where T is thrust. The formula can be directly represented in terms of inflow and exit velocities for a simplified propulsor (mechanical) model such as the one given in figure 2.2.

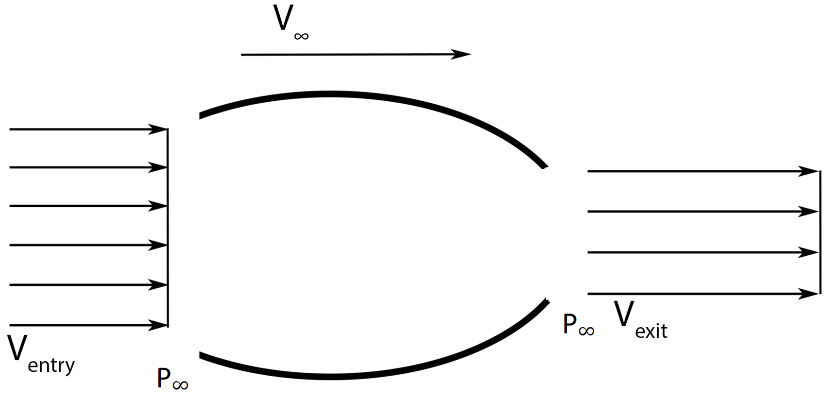

Figure 2.2: Simplified propulsor model.

For the propulsor in figure 2.2, it is assumed that the static pressure at the propulsor exit and inlet are equal to the freestream value. It is further assumed that no additional mass flow (like fuel) is injected into the propulsor. Also, as can be noticed from figure 2.2, the entry and exit velocities respectively are assumed to be uniform. Then the Power added by the propulsor to the flow would be the change in flow kinetic energy given by:

$$P_{propulsor} = \frac{1}{2}\dot{m}(V_{exit}^2 - V_{entry}^2) . \tag{2.2}$$

Thrust can be expressed as:

$$T = \dot{m}(V_{exit} - V_{entry}) . \tag{2.3}$$

Propulsive efficiency can then be obtained as the ratio of the ideal propulsive power (TV_∞) to the actual power supplied by the propulsor:

$$\eta_{propulsive} = \frac{TV_\infty}{P_{propulsor}} = \frac{\dot{m}(V_{exit} - V_{entry})V_\infty}{\frac{1}{2}\dot{m}(V_{exit}^2 - V_{entry}^2)} = \frac{2V_\infty}{V_{exit} + V_{entry}} . \tag{2.4}$$

In case $V_{entry} < V_\infty$ (note that WI and BLI actually have lower non-uniform inflow velocities than freestream velocity) and $V_{exit} \approx V_\infty$ (complete wake filling) it leads to the confusion of incorrect efficiency value of greater than unity. It should be noted that for WI and BLI the lower non-uniform inflow velocities should be integrated over an entry area. Also, if the inflow velocity is very small ($V_{entry} << V_\infty$), then the Froude's efficiency value becomes almost two ($\eta \approx 2$). But note that the above formula is consistent for a freestream ingesting propulsor (as $V_{exit} > (V_{entry} = V_\infty)$). This paradox requires a careful analysis of power.

Smith [5] introduced a metric called the power saving coefficient for wake ingestion (actually applicable to WI and BLI) in cruise flight which is commonly used in the later literature and is defined as [5]:

$$PSC_{actual} = \frac{P_{non-BLI} - P_{BLI}}{P_{non-BLI}} , \tag{2.5}$$

where the non-BLI power can be explicitly expressed in terms of the propulsive efficiency as [5]:

$$P_{non-BLI} = \frac{DV_\infty}{P_{propulsive}} . \tag{2.6}$$

Next for an imaginary ideal propulsor in freestream (with no jet dissipation), PSC can be completely represented in terms of the drag power as:

$$PSC_{strict} = \frac{DV_\infty - P_{BLI}}{DV_\infty}\,, \tag{2.7}$$

which of course would be lower than the actual power saving coefficient (PSC_{actual}). This value is used in most part of the current thesis due to the simplicity in calculations that it requires and the term PSC in the subsequent parts represents the PSC_{strict} definition. It should be noted that this definition is quite useful to compare different fuselage configurations as will be seen but is still unfair for comparison of a specific propulsor design. Propulsor design would need to be treated as a separate topic and is out of the scope of the present thesis.

For the case of BLI/WI, a propulsor is defined as ideal if it completely fills the wake of a body without causing any changes to the upstream flow field. Such a definition can also be found in [1]. In such a case an ideal power saving coefficient is defined as:

$$PSC_{ideal} = \frac{DV_\infty - P_{BLI-ideal}}{DV_\infty}\,, \tag{2.8}$$

where the $P_{BLI-ideal}$ could be obtained as the power in the flow entering a propulsor. This just requires the calculation of the power in flow at any location from an isolated body simulation as the ideal propulsor is assumed to have no effect on the upstream flow. Also, the power in the flow can be reduced to exergy flow (as only that is actually extractable in accordance with the second law of thermodynamics [23]) if thermal energy flow is also considered.

For an isolated body simulation, a PSC_{ideal} could be defined based on power balance method as:

$$PSC_{ideal} = \left(\frac{DV_\infty - \Phi}{DV_\infty}\right)_{TE} = \left(\frac{\dot{E} - P_V}{DV_\infty}\right)_{TE}\,, \tag{2.9}$$

which may not be very appropriate if thermal energy is significant in the flow. For such a case, an exergy based definition could be given as:

$$PSC_{ideal} = \left(\frac{DV_\infty - \dot{A}}{DV_\infty}\right)_{TE} = \left(\frac{\dot{\varepsilon}}{DV_\infty}\right)_{TE}\,, \tag{2.10}$$

which is the most appropriate for transonic flights. The definitions of $\dot{E} - P_V$ and Φ can be found in section 2.3. The definitions of $\dot{\varepsilon}$ and $\dot{A}$ can be found in section 2.4. The subscript TE is to highlight the fact that the maximum power or exergy flow is at the trailing edge of the isolated body and the calculated metirc should be representative of the energy flow (or exergy flow) at this point which would be wasted in the wake if not used. The dissipation (Φ) and anergy ($\dot{A}$) on the other hand can be viewed as the inevitably lost power till the body trailing edge under consideration. It is convenient to call this dissipation and anergy as the surface values (surface dissipation or surface anergy) as it occurs in the flow over the surface of the body.

The various definitions would be required to understand and appreciate the power benefit possible through the concept of BLI.

2.3. THE POWER BALANCE METHOD

The power balance method was introduced by Drela [1] which allowed an elegant analysis of the tightly integrated configurations. It should be noted that the propulsive power (2.2) as defined in section 2.2 when applied to BLI/WI configurations would not just consist of the power supplied by the propulsor but would also include the power present in the WI or BLI flows. This can be mathematically shown when the power balance method is used to analyze such configurations. The power balance method as introduced by Drela [1] is a general control volume analysis which can be used to quantify various power sources and sinks of a general configuration. The method as in [1] is presented next.

The CV presented in figure 2.3 is adapted from [1]. The important difference as compared to [1] is the fact that the variable u represents the complete x-component of velocity and not just the excess or defect in x-velocity when compared to the freestream. The control volume consists of an inner boundary (BS) covering

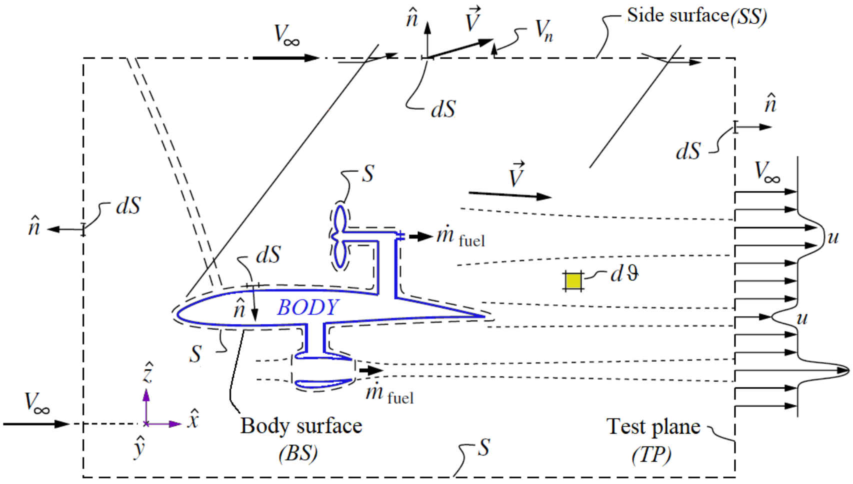

Figure 2.3: Control volume for power balance analysis and exergy analysis. Adapted from [1].

the body and the propulsors and an outer boundary covering the Test plane (TP) and side surface (SS). To avoid confusion regarding the possible location of the downstream plane, the aft plane will be called a test plane throughout this thesis. The TP is chosen to be normal to V_∞ while the side surface is chosen to be parallel to V_∞. Such a test plane which is far from the body would be a Trefftz plane (TFP). The plane upstream of the body is assumed to be at freestream conditions. Drela [1] also mentions that the choice of the distance of side boundaries can simplify the analysis if chosen appropriately depending on the problem. It is further assumed that the TP is sufficiently far away from the body so that the shock waves leave the CV completely from the side boundaries.

The mechanical energy equation is obtained using the Navier-Stokes momentum equation in divergence form by taking the dot product with the velocity variable (V). The volume integral of the equation over the control volume and simplification gives the complete list of power sources and sinks. The details of the exact derivation can be found in [1]. The following equation represents the power balance:

$$P_S + P_V + P_K = \dot{E} + \Phi - F_x V_\infty \,, \tag{2.11}$$

here the P terms represent the sources of power which include the effects like the presence of a propulsor (with or without blading). The terms on the right represent the power outflow through the TP ($\dot{E}$) and the power lost in the control volume due to dissipation into heat (Φ). The P_S term can represent the shaft power from different components. It can be understood to represent the power from the propulsors whose moving parts are covered by BS like the propeller in figure 2.3 [1]. It can be expressed as [1]:

$$P_S = \iint_{BS} [-(p - p_\infty)\hat{n} + \bar{\bar{\tau}}.\hat{n}].\vec{V}\, dS \,, \tag{2.12}$$

where the velocity vector $\vec{V}$ can be split into its components as:

$$\vec{V} = u\hat{i} + v\hat{j} + w\hat{k} \,. \tag{2.13}$$

Thus, the P_S term could be especially useful in the case in which the modeling of the actual propulsor components like the blades of fan, compressor or turbine is necessary. In simplified propulsor modeling like actuator disc model, this term would not be a contributor.

Next, the P_V term is the pressure-volume power term which refers to any power added into the CV by expansion against the atmospheric pressure. This is significant in the cases in which the pressure causing expansion is quite different from the atmospheric value like a combustor [1]. But it also plays a role in determining the power balance when compressibility cannot be neglected (especially when TP is very close to the aerodynamic body in a high speed flow). This term indeed becomes important when analyzing transonic flight as will be seen later. It is expressed as:

$$P_V = \iiint_{CV} (p - p_\infty)\nabla.\vec{V} d\vartheta\,. \tag{2.14}$$

The P_K term in the power balance equation 2.11 covers the flow of power across the BS surface covering the cases like the bottom propulsor as in figure 2.3 [1]. The pressure work and the kinetic energy flows across BS representing P_K is given by [1]:

$$P_K = \iint_{BS} -[(p - p_\infty) + \frac{1}{2}\rho(V^2 - V_\infty^2)]\vec{V}.\hat{n} dS\,. \tag{2.15}$$

Next, moving on to the terms on the right hand side of the power balance equation 2.11, the $\dot{E}$ term can be split into several contributions as follows:

$$\dot{E} = W\dot{h} + \dot{E}_a + \dot{E}_v + \dot{E}_p + \dot{E}_w\,, \tag{2.16}$$

here the $W\dot{h}$ term represents the power required to climb or gained due to descent. Next the $\dot{E}_a$ term is given by:

$$\dot{E}_a = \iint_{TP} \frac{1}{2}\rho(u - V_\infty)^2 u dS \tag{2.17}$$

This term is called the streamwise kinetic energy deposition rate [1] and represents the axial kinetic energy crossing the TP. A similar term can be used to represent the kinetic energy flow due to the normal velocity components which is given by:

$$\dot{E}_v = \iint_{TP} \frac{1}{2}\rho(v^2 + w^2) u dS \tag{2.18}$$

One important aspect to mention is the fact that the static pressure very close to an aerodynamic body is different from the freestream static pressure. Smith [5] considers the wake ingestion cases for which the static pressure has recovered to the freestream value. A term to represent the transport of power across the TP due to the pressure defect is the $\dot{E}_p$ given by:

$$\dot{E}_p = \iint_{TP} (p - p_\infty)(u - V_\infty) dS \tag{2.19}$$

In level flights, the sum of the three terms $\dot{E}_a$, $\dot{E}_v$ and $\dot{E}_p$ at the body trailing edge represent the wake power flow in case of incompressible flows. For compressible flows, the P_V term also plays a role (as $\nabla.V$ is not zero everywhere like in the incompressible case) as will be shown later. Also, one important aspect to note is that the power in the wake of a body cannot be separately taken in terms of only some of the terms composing $\dot{E}$ like $\dot{E}_a$. Meaning a propulsor operating behind a body cannot just use the power available as $\dot{E}_a$ and gain a benefit. It is easy to understand this statement if the case of an inviscid flow over an airfoil is considered. According to [1], for such a case, $\dot{E}_a + \dot{E}_v + \dot{E}_p = 0$, in which the negative $\dot{E}_p$ term cancels the other two. Thus, if a propulsor behind an airfoil with such a flow were to just use $\dot{E}_a$ to produce an acceleration, it would end up being a perpetual motion machine.

Next, the Φ term represents the dissipation or conversion of mechanical energy into heat. The viscosity in real flows is the reason for such dissipation and this term is contributed to by boundary layers, body wakes, propulsor plumes, vortices, and shock waves. The following general definition can be given for viscous dissipation [1]:

$$\Phi = \iiint_{CV} (\bar{\bar{\tau}}.\nabla).\vec{V} d\vartheta \tag{2.20}$$

Finally, coming to the last term on the right hand side of 2.11, the $F_x V_\infty$ term. This just represents the net force power, which for example would be equal to the drag power (DV_∞) for an isolated body. For a cruising flight , the net force would be zero and the term can be removed from the power balance. The net force definition eliminates the requirement for thrust and drag separation which is ambiguous for tightly integrated configurations. The net force can be expressed in terms of flow field variables at the test plane and the side surface as:

$$F_x = \iint\limits_{TP} -[(p-p_\infty)+\rho(u-V_\infty)u].dS + \iint\limits_{SS} -\rho(u-V_\infty)v.dS \tag{2.21}$$

As already mentioned, the power balance method clarifies certain important questions regarding BLI/WI and also resolves the over-unity paradox. This will be shown next. Considering a propulsor working in freestream and a wake ingesting propulsor, power calculations are performed. Figure 2.4 shows the two cases.

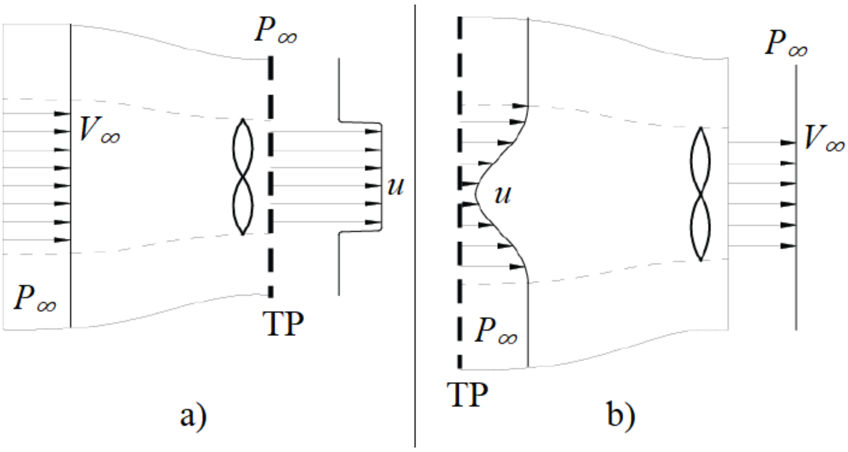

Figure 2.4: **a)** Freestream propulsor case. **b)** Ideal wake filling propulsor case. Figure Adapted from [7].

For the propulsor in figure 2.4-a), the propulsive efficiency is given as the ratio of the thrust power to the actual power supplied by the propulsor. This can be expressed as [7]:

$$\eta_{propulsive} = \frac{TV_\infty}{P_{propulsor}} = \frac{\iint\limits_{TP} \rho u(u-V_\infty)V_\infty.dS}{\iint\limits_{TP} \frac{1}{2}\rho u(u^2-V_\infty^2).dS} = \frac{\iint\limits_{TP} \rho u(u-V_\infty)V_\infty.dS}{\iint\limits_{TP} \frac{1}{2}\rho u(u-V_\infty)V_\infty.dS + \iint\limits_{TP} \frac{1}{2}\rho u(u-V_\infty)^2.dS}, \tag{2.22}$$

$$\eta_{propulsive} = \frac{TV_\infty}{P_{propulsor}} = \frac{TV_\infty}{TV_\infty + \dot{E}_a} \leq 1\,. \tag{2.23}$$

Clearly, for the propulsor operating in freestream, the propulsive efficiency is lesser than unity. The $\dot{E}_a$ term is the same as the term defined in the power balance by Drela [1] (see equation 2.17) which must be positive for thrust generation. Next, for the ideal wake filling propulsor (figure 2.4-b), the propulsive efficiency would be given by [7]:

$$\eta_{propulsive} = \frac{TV_\infty}{P_{propulsor}} = \frac{\iint\limits_{TP} \rho u(V_\infty-u)V_\infty.dS}{\iint\limits_{TP} \frac{1}{2}\rho u(V_\infty^2-u^2).dS} = \frac{\iint\limits_{TP} \frac{1}{2}\rho u(V_\infty-u)^2.dS + \iint\limits_{TP} \frac{1}{2}\rho u(V_\infty^2-u^2).dS}{\iint\limits_{TP} \frac{1}{2}\rho u(V_\infty^2-u^2).dS}, \tag{2.24}$$

$$\eta_{propulsive} = \frac{TV_\infty}{P_{propulsor}} = \frac{P_{propulsor} + \dot{E}_a}{P_{propulsor}} \geq 1\,. \tag{2.25}$$

It now becomes clear that the power in the body wake is also utilized by the wake filling propulsor for power generation. The above analysis leads to the direct conclusion that the hypothetical ideal wake filling propulsor is better in performance than a freestream ingesting propulsor. This fact makes BLI/WI an attractive possibility for fuel consumption cut down in flights.

2.4. EXERGY ANALYSIS

The theoretical limitation of a power balance analysis as described in section 2.3 is the fact that temperature field becomes obscured and there is a possibility of over predicting the usable power due to boundary layer ingestion. This will become clear once the calculations are performed on different configurations in the subsequent chapters. Arntz et al. [2] introduced an exergy based analysis for such aircraft application which can be viewed as an extension of Drela's PBM with the inclusion of thermal effects. Certain important terms from the work of Arntz et al. [2] will be used in the present thesis to supplement the arguments made using Drela's PBM.

The CV for the analysis can be considered the same as that used for PBM in figure 2.3. Energy can be split into usable and useless parts based on the second law of thermodynamics [23] according to which a heat engine cannot operate at 100% efficiency and the maximum theoretical efficiency is that of the Carnot engine [23]. Thus, with the assumption that any power available in the wake as thermal energy is extractable with the efficiency of a Carnot engine, the power balance method can be extended. This leads to the following equation as given by Arntz et al. [2]:

$$\dot{\varepsilon}_p = \dot{\varepsilon}_m + \dot{\varepsilon}_{th} + \dot{A} - F_x V_\infty \,, \tag{2.26}$$

where the anergy $\dot{A}$ can be further split into different contributions:

$$\dot{A} = \dot{A}_\Phi + \dot{A}_{thm} \,. \tag{2.27}$$

It should be noted that the heat transfer from the surface of the fuselage is not considered (adiabatic assumption). Meaning that the fuselage is assumed to be an insulator and the corresponding term is not included in equation 2.26. Probably the fuselage surface could be modeled as a heat source or sink depending on the application in the future. The terms in equation 2.26 are explained next.

Starting with the terms on the right hand side of equation 2.26, the term $\dot{\varepsilon}_m$ exactly represents the $\dot{E}$ term introduced in section 2.3. This can be easily understood since mechanical energy is the same as mechanical exergy.

Next, the term $\dot{\varepsilon}_{th}$ represents the thermal exergy outflow from the CV. This term forms a part of the total thermal energy $\dot{E}_{th}$ outflow from CV. Once the thermal energy outflow is known, this term can be given based on the Carnot engine efficiency value operating in the given temperature field. Thermal energy outflow is given by [2]:

$$\dot{E}_{th} = \iint_{TP} \rho(e - e_\infty) u \, dS + \iint_{TP} p_\infty u \, dS \,, \tag{2.28}$$

where e is the internal energy and it is considered that the side surface is far away from the body so that all outflow is through the TP. The exergy can be calculated directly from the thermal energy by subtracting the anergy generation rate $\dot{A}$ from the thermal energy outflow. This is given by [2]:

$$\dot{\varepsilon}_{th} = \dot{E}_{th} - \iint_{TP} T_\infty \rho(s - s_\infty) u \, dS \,, \tag{2.29}$$

where s is the entropy (with dimensions and not to be confused with the normalized entropy as defined in sub-section 2.5.2). Further, as already clear, the anergy generation rate in the CV can be easily obtained using the local entropy field at the TP as [2]:

$$\dot{A} = \iint_{TP} T_\infty \rho(s - s_\infty) u \, dS \,. \tag{2.30}$$

Unlike viscous dissipation (Φ) as introduced in section 2.3, the anergy generation rate $\dot{A}$ is much simpler to calculate if the entropy field is available. Also, anergy is a much more reliable term from the perspective of studying the energy extractable in configurations such as fuselage with BLI. The split up of the anergy generation rate can be obtained as the sum of the anergy rate due to viscous dissipation ($\dot{A}_\phi$) and thermal mixing ($\dot{A}_{thm}$). The viscous dissipation related anergy term can include boundary layers , wakes, swirl, propulsor plumes, and even shocks (a separate $\dot{A}_w$ (as in [2]) for shocks may not be necessary if the Φ definition as given in section 2.3 is used). The anergy rate splitting is made possible by the application of Eddy viscosity model in mean entropy production of Moore and Moore [24] as mentioned in [2]. The viscous dissipation anergy rate can be given as [2]:

$$\dot{A}_\Phi = \iiint\limits_{CV} \frac{T_\infty}{T}(\bar{\bar{\tau}}.\nabla).\vec{V}\,d\vartheta\,, \tag{2.31}$$

which further leads to the definition of viscous dissipation exergy ($\dot{\varepsilon}_\Phi$) which can be viewed as a power source that is made available due to the heat from the viscous dissipation [2]. It can be given as [2]:

$$\dot{\varepsilon}_\Phi = \iiint\limits_{CV} \left(1-\frac{T_\infty}{T}\right)(\bar{\bar{\tau}}.\nabla).\vec{V}\,d\vartheta\,, \tag{2.32}$$

which when summed with $\dot{A}_\Phi$ obviously gives the viscous dissipation (Φ) as defined in section 2.3. Further, the thermal mixing anergy related to the finite thermal conductivity of fluid is given by [2]:

$$\dot{A}_{thm} = \iiint\limits_{CV} \frac{T_\infty}{T^2}k(\nabla T)^2\,d\vartheta\,. \tag{2.33}$$

Finally, the exergy supplied by the propulsor ($\dot{\varepsilon}_p$) can be given by [2]:

$$\dot{\varepsilon}_p = -\iint\limits_{B} \rho(h_0 - h_{0,\infty})u\,dS + \iint\limits_{B} T_\infty\rho(s-s_\infty)u\,dS\,. \tag{2.34}$$

This exergy analysis as will be observed later is important for transonic flight analysis involving tightly integrated configurations.

Further, an important relation connecting the power balance method and the exergy analysis for isolated fuselage is the following [2]:

$$\dot{A} - \Phi = \dot{A}_{thm} - \dot{\varepsilon}_\Phi\,. \tag{2.35}$$

2.5. FLOW SOLVERS

The main motive of this section is to give a brief explanation about the flow solvers used and the relevant theoretical background, especially for the low fidelity solver MTFLOW which is used for most of the studies in the thesis.

2.5.1. RANS SOLVER

Ansys Fluent (version 18.1) [25] is the solver chosen for comparison of important results from the low fidelity solver. It is specified here that the Euler-IBLT solver uses an axisymmetric formulation and the same simplification is used for the respective RANS simulations. The RANS equations are solved using a finite volume discretization scheme in Fluent for the flight fuselage simulations. Individual boundary conditions and meshes used in different simulations are mentioned in the respective sections. The RANS equations are obtained by Reynolds averaging (which is an ensemble averaging procedure and is equivalent to time averaging for statistically steady flows) [26, 27]) the Navier-Stokes equations [26, 27]. Since Fluent is used to attain some confidence regarding the results from the low fidelity solver, the required power balance terms are studied systematically starting from application to simple incompressible-laminar flows to compressible-turbulent flows. It should be noted that the flows over aircraft fuselages that will be considered are typically in the transonic regime and the flow needs to be described using a compressible and turbulent flow model. The flight simulations in Fluent are performed using the ideal gas law for capturing the fluid compressibility and k-ω-SST turbulence model for modeling turbulence. Sutherland's law (three-coefficients method) is used to model the fluid viscosity for compressible flows. The flow field variables can be split into a mean and fluctuating component as follows:

$$f = \overline{f} + f'\,, \tag{2.36}$$

where $\overline{f}$ is the mean value and f' is the fluctuating component. The continuity equation can be given as (not showing the overbar on mean quantities except on Reynolds stress) [25]:

$$\frac{\partial\rho}{\partial t} + \frac{\partial(\rho u_i)}{\partial x_i} = 0\,. \tag{2.37}$$

Similarly, the momentum equation can be expressed as [25]:

$$\frac{\partial(\rho u_i)}{\partial t} + \frac{\partial(\rho u_j u_i)}{\partial x_j} = -\frac{\partial p}{\partial x_i} + \frac{\partial \sigma_{ij}}{\partial x_j} + \frac{\partial(-\rho\overline{u_i' u_j'})}{\partial x_j}\,, \tag{2.38}$$

where $-\rho\overline{u_i' u_j'}$ is the Reynolds stress term which needs to be modeled for closure. Eddy viscosity hypothesis is used in turbulence models like k-ω-SST and Spalart-Allmaras for the modeling. The viscous stress term σ_{ij} is approximated by [25, 27]:

$$\sigma_{ij} \approx 2\mu\left(S_{ij} - \frac{1}{3}S_{kk}\delta_{ij}\right). \tag{2.39}$$

Further, the Reynolds stress term can be approximated by Eddy viscosity model as [25, 26]:

$$-\rho\overline{u_i' u_j'} = 2\mu_t\left(S_{ij} - \frac{1}{3}S_{kk}\delta_{ij}\right) - \frac{2}{3}\rho k\delta_{ij}\,, \tag{2.40}$$

where S_{ij} is the strain rate tensor, δ_{ij} is the Kronecker delta function ($\delta_{ij} = 1$ if $i = j$ else $\delta_{ij} = 0$ if $i \neq j$), μ_t is the turbulent or Eddy viscosity, and k is the kinetic energy of the fluctuating flow field given by $((\tilde{u}')^2 + (\tilde{v}')^2 + (\tilde{w}')^2)/2$.

Further, the solution of compressible flows requires the energy equation as well. The energy equation further introduces the temperature variable and an additional equation becomes necessary for closure which for example can be the ideal gas equation. The energy equation and the introduction of the turbulent thermal conductivity (κ_t) can be found in [27] and is not repeated here.

2.5.2. EULER-IBLT SOLVER

The main motive of the present section is to provide a brief explanation of important concepts relevant to the combined Euler and integral boundary layer theory solver (MTFLOW) which is used by Drela [20] for rapid solving of flow field equations. As already mentioned, MTFLOW is a compressible flow solver for axisymmetric geometries [21]. MTFLOW assumes the real flow to be divided into a viscous and an inviscid part and the two flows are handled using different equations. The inviscid flow is described using the Euler equations which allows for rotational flow capture at and near shocks unlike the potential flow equations [20]. A finite volume discretization is applied to the conservation form of the equations which again prevents numerical issues at and near shocks [21]. The inviscid flow equations are described next.

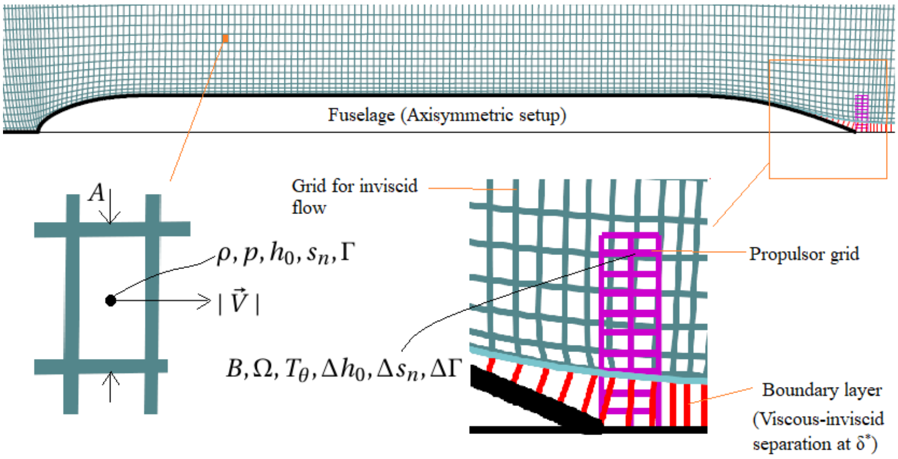

Figure 2.5: MTFLOW flow domain example.

MTFLOW applies mass conservation to each streamtube. This can be captured using the following equation [21]:

$$\dot{m} = \rho\,|\,\vec{V}\,|\,A(2\pi r - BT_\theta)\,, \tag{2.41}$$

where A is the cell width in the direction as shown in figure 2.5 and $|\vec{V}|$ is the meridional speed of the fluid. The mass flow is explicitly fixed in each streamtube instead of having a differential continuity equation [21].

According to Drela [21], either a momentum conserving or an entropy conserving equation can be used. Each have their pros and cons. The entropy conservation equation, for example, prevents geometry related numerical issue of spurious losses or gains. This especially can be significant near leading edge in which there is a sudden incorrect increase or drop in entropy. On the other hand, the entropy conservation equation is found to have trouble close to shocks [21]. The streamwise or the normal momentum conservation equation can be given as [21]:

$$dp + \rho\,|\vec{V}|\,d(|\vec{V}|) + \rho V_\theta dV_\theta + pd(\Delta s_n) - \rho\Omega\Gamma = 0\,. \tag{2.42}$$

The streamwise or the normal entropy conservation equation can be given as [21]:

$$-pds_n + pd(\Delta s_n) + \rho d(\Delta h_0) = 0\,. \tag{2.43}$$

The differentials are taken in the required directions and the entropy s_n in the above equations is defined in dimensionless form and expressed as [21]:

$$s_n = ln\left(\frac{\left(\frac{h}{h_\infty}\right)^{\frac{\gamma}{\gamma-1}}}{\frac{p}{p_\infty}}\right), \tag{2.44}$$

where the subscript ∞ can represent the freestream value that is specified at the inlet of the domain. It should also be noted that changes in total enthalpy or entropy given by Δh_0 and Δs_n respectively must be specified by the user to model different aspects when required. Further, the momentum balance in the transverse direction is described using:

$$d\Gamma - d(\Delta\Gamma) = 0\,, \tag{2.45}$$

where the swirl change $\Delta\Gamma$ again is user specifiable and, for example, can be used to model a mechanical propulsor. Finally, the energy equation is given by [21]:

$$dh_0 - d(\Delta h_0) - \Omega d\Gamma = 0\,, \tag{2.46}$$

where Ω is the propulsor rotor angular speed. As can be easily understood, to model an actuator disk with negligible swirl, it is possible to choose a low value of swirl change $\Delta\Gamma$ distribution (low enough to make the swirl velocity negligible) and a corresponding value of Ω to add the required amount of power to the flow.

Another important aspect to note is the fact that there is no flow field in the region with the modeled boundary layer (till δ^*) shown in figure 2.5. This means that till δ^* (displacement thickness), there is no flow field (velocity, pressure, entropy etc.) output but rather only certain boundary layer related integral quantities which are calculated at the streamwise locations. Before moving on to the viscous equations it is important to mention that a propulsor grid cannot entirely lie in the displacement area of the boundary layer. This is because the propulsor can only act on the inviscid flow field which indirectly affects the boundary layer field as will be understood once the viscous equations are described. It should also be noted that the propulsor must further satisfy the condition that its size must be greater than the actual boundary layer thickness (δ) for correct capturing of physical flow as is elaborated in A.2.

Next, moving on to the viscous equations, Drela uses a mechanical energy formulation to describe the boundary layer. The starting point is, of course, the Prandtl's boundary layer equations. The continuity is given for 2-D flow by [20]:

$$\frac{\partial(\rho u)}{\partial x_n} + \frac{\partial(\rho v)}{\partial y_n} = 0\,, \tag{2.47}$$

where the n subscript is to represent the fact that the coordinates have been taken normal to the body (local coordinates) on which the boundary layer exists. Next, the momentum equation is given for 2-D flow by [20]:

$$\rho u\frac{\partial u}{\partial x_n} + \rho v\frac{\partial u}{\partial y_n} = \rho_e u_e\frac{\partial u_e}{\partial x_n} + \frac{\partial \tau}{\partial y_n}\,, \tag{2.48}$$

where the subscript e represents the boundary layer edge quantity and τ can be given by:

$$\tau = \mu_l \frac{\partial u}{\partial y_n} - \rho \overline{u'v'}\,, \tag{2.49}$$

where it should be noted that the Reynold's stress term ($-\rho\overline{u'v'}$) represents the extra shear stress due to turbulence. Further, the mechanical energy equation can be obtained by multiplying the momentum equation with u. It should be clearly understood that the single equation for momentum mentioned above accurately captures both the streamwise and the normal momentum equations by the introduction of the boundary layer edge quantities. The pressure across (in the normal direction) the boundary layer is assumed constant and is equal to the edge value of p_e. The energy equation based on total enthalpy is not used in MTFLOW for the boundary layer flow [21]. This occurs as a result of the assumption that the flow is adiabatic and the Prandtl number is close to unity [20]. This, of course, limits the use of MTFLOW to dissipation analysis and exergy analysis cannot be performed. The temperature field in the fluid can be studied only in the RANS solver. Since a dissipation based analysis has been in use in the literature before and after the work of Arntz et al. [2] and its successful application to the D8 transport aircraft [10, 28] encourages its use anyways. It should also be noted that unless the temperature differences are very significant, dissipation based analysis is very close to an anergy based analysis. Also, the propulsor which is actually able to use both the mechanical and thermal energy in the flow is yet to be considered in the literature for BLI based configurations.

The momentum and mechanical energy equations are integrated across the boundary layer obtaining the Von Kármán boundary layer momentum integral and Drela's boundary layer kinetic energy (mechanical energy) integral equations. These can be written in the conservation form as [1, 20]:

Momentum:

$$\frac{d(\rho_e u_e^2 \theta)}{dx_n} = \underset{\text{Friction term}}{\boxed{\rho_e u_e^2 \frac{C_f}{2}}} - \underset{\text{Pressure term}}{\boxed{\rho_e u_e \delta^* \frac{du_e}{dx_n}}}\,, \tag{2.50}$$

Mechanical energy:

$$\frac{d(\frac{1}{2}\rho_e u_e^3 \theta^*)}{dx_n} = \underset{\text{Dissipation term}}{\boxed{\rho_e u_e^3 C_\Phi}} - \underset{\substack{\text{Term related to}\\ \text{pressure gradient and}\\ \text{compressibility}}}{\boxed{\rho_e u_e^2 \delta^{**} \frac{du_e}{dx_n}}}\,, \tag{2.51}$$

where $\rho_e u_e^2 \theta$ and $\frac{1}{2}\rho_e u_e^3 \theta^*$ are momentum defect and kinetic energy defect respectively. The boundary layer integral terms are explained in A.1. These equations can be written in the axisymmetric form (as required by MTFLOW) as:

Momentum:

$$\frac{d(\rho_e u_e^2 \theta b)}{dx_n} = \rho_e u_e^2 b \frac{C_f}{2} - \rho_e u_e \delta^* b \frac{du_e}{dx_n}\,, \tag{2.52}$$

Mechanical energy:

$$\frac{d(\frac{1}{2}\rho_e u_e^3 \theta b)}{dx_n} = \rho_e u_e^3 b C_\Phi - \rho_e u_e^2 \delta^{**} b \frac{du_e}{dx_n}\,, \tag{2.53}$$

where b (given as $b = 2\pi r + \pi\delta^* \hat{n}.\hat{r} - BT_\theta$ [21]) is the circumference of the immediate streamtube starting at the displacement thickness. The logarithmic form of these equations is available in [21]. These are:

Momentum:

$$\frac{d\theta}{\theta} = \frac{C_f}{2}\frac{ds}{\theta} - (H+2)\frac{du_e}{u_e} - \frac{d\rho_e}{\rho} - \frac{db}{b}\,, \tag{2.54}$$

Mechanical energy:

$$\frac{dH^*}{H^*} = \left(\frac{2C_\Phi}{H^*} - \frac{C_f}{2}\right)\frac{ds}{\theta} + \left(H - 1 - \frac{2H^{**}}{H^*}\right)\frac{du_e}{u_e}\,. \tag{2.55}$$

These equations written in this form help to declare the unknowns which need to be calculated to achieve closure. For example if the displacement and momentum thickness (δ^* and θ) are considered independent variables, then the momentum and mechanical energy equations would still have C_f, C_Φ, H^* and H^{**} as unknowns [20] (it should be noted that edge quantities like u_e are available from the inviscid solution). Thus, the unknowns would have to be related to the known quantities. It is found that these declared unknowns are dependent on the kinetic shape parameter (H_k, edge Mach (M_e) and momentum thickness Reynolds number (Re_θ) [20]. Further, certain boundary layer profiles are assumed to find the unknowns. For laminar flow, Falkner-Skan family profiles are used (as seen from MTFLOW source code) and for turbulent flow, the closure is achieved based on the empirical relations given by Swafford [29] (the reference to such a closure in MTFLOW is mentioned in [30]). Though it is not mentioned in [21] regarding such closures, it is highly likely that the MTFLOW code is based on [20]. Further, a shear lag equation is used to account for the non-equilibrium turbulence [21]. The shear lag equation can be found in [21] and the details of it can be understood from [20]. Finally, the laminar to turbulent transition is predicted based on the e^N method (which is an extension of the e^9 method by Ingen [31]). It should be noted that e^N method is based on linear stability theory and is only useful when the transition initiation is dominated by Tollmien-Schlichting waves [32]. The boundary layer equations and the Euler equations are solved simultaneously using Newton's method in MTFLOW [21].

The above described Euler-IBLT formulation results in a very efficient solver in terms of computational time although some accuracy may be lost. Also, the mesh generation process in MTFLOW can be easily automated using a few parameters. This ultimately results in a solver that is readily suitable for design space exploration and optimization studies. Finally, it is again mentioned that it is only possible to perform a dissipation analysis using MTFLOW and the exergy information is unavailable and requires the use of the RANS solver.

3

BOUNDARY LAYER INGESTION STUDIES USING CFD

Analysis of boundary layer ingestion in aircraft configurations using CFD requires a careful analysis of the behavior of the methods such as power balance and exergy analysis in a CFD framework. Various simple cases are used to study different terms introduced in sections 2.3 and 2.4. A comparison with analytical values are made where possible. It should be noted that the dependence of the numerical errors on the details like the definition of the control volume and the mesh size need to be investigated. This section presents various comparisons which help to gain an idea about such errors and also shows the effect of different propulsor modeling. Further, specific results from both RANS and Euler-IBLT solvers are presented for understanding the pros and cons of each solver.

As described in section 2.3, the power balance method is the simple application of energy conservation principle to a flow and the exergy information can further be obtained by the application of the second law of thermodynamics for the exergy analysis. The various terms described can be calculated for different flow fields. The flow field required, on the other hand, can be obtained by various methods as per requirement. For example, the flow field information could be obtained from an experimental result using PIV as done by Lv and Rao [9] or from a CFD simulation of the flow. Also, if the power supply to a propulsor is known, the power saving achieved due to BLI or WI can be directly obtained without the complete flow field information as done in a few works in the literature [10–12]. It should be noted that the calculation of the power balance integrals themselves depend on numerical integration techniques as only discrete flow field data are available from methods like CFD. Thus, the accuracy of the numerical technique used for interpolation of the flow field and to perform the integration also plays a role in the possible errors in the power balance or exergy analysis. The main task of the current section is to clearly identify the possible errors from various sources so that they can be avoided in the actual study. Also, it should be noted that the results from CFD themselves do not represent a flow more realistically than the model used to mimic the physics. For example, an inviscid flow field would not capture the effect of viscosity and a laminar flow model would not capture turbulence. The model to be used depends on the requirement. For example, the flow over a fuselage is compressible, viscous, three-dimensional, and turbulent for the most part due to the high Reynolds and Mach numbers involved. It would be systematic to quantify and analyze the required terms for various flow models starting from a simple case and slowly moving on to complicated cases, noting in each case the various error sources and the methods to rectify or circumvent them. Moreover, the complete balance of various power terms would be checked in the present section for simple cases of flow over a flat plate and the easily and reliably computable quantities would be identified which could be used for further studies without issues. Exergy analysis will also be presented for the case of transonic flow over a baseline fuselage geometry which will supplement power balance analysis to give a deeper insight into the possible benefit in the BLI configurations.

As already mentioned, the CFD calculations for the present thesis are done using two different methods. The first consists of low fidelity calculations using a coupled Euler and IBLT solver called MTFLOW by Drela [21] and the second uses RANS based CFD calculations performed using the commercial software package - Ansys Fluent [25]. It should be noted that MTFlow is a solver for flows through/over axisymmetric bodies only. An axisymmetric model is incapable of capturing the effect of circumferential flow distortion but is still is capable of providing information about the power consumption which can lead to a preliminary fuselage design. RANS CFD is computationally expensive when compared to Euler-IBLT CFD but allows complete flow field capturing, unlike Euler-IBLT CFD which provides the boundary layer integral quantities as described previously. The following studies are performed in the present section:

- A study to show the power benefit of BLI/WI for the flow (laminar and turbulent) over a flat plate.
- A comparison of Euler-IBLT CFD (using MTFLOW) results with RANS CFD (using Ansys Fluent) for NACA0040 BOR from the experimental work of Sabo and Drela [12] (incompressible flow case) and axisymmetric aircraft fuselage constructed using shapes from ESDU 77028 document [17] (compressible flow case).

The above-defined studies would provide a clear opportunity to understand the power balance and exergy analysis methods and the associated issues that can occur in different cases. This would allow building a clear foundation for the design space studies.

It should be noted that the power balance method as introduced by Drela [1] is derived from the mechanical energy conservation equation which is obtained directly from the momentum equation [1].This indeed represents the complete energy conservation without explicitly quantifying the thermal distribution. Clearly, the method applies for any case in which thermal effects are also present like compressible flows and the presence of heat sources (only that certain important thermal effects cannot be explicitly quantified). As all the cases that would be considered in the present work would not involve the blading details of the propulsors, the P_S term can be dropped from the power balance equation (2.11) and the following is obtained:

$$P_V + P_K = \dot{E} + \Phi \tag{3.1}$$

Also expanding the $\dot{E}$ term without the potential energy change rate term $(W\dot{h})$ the following can be written:

$$P_K = \dot{E}_a + \dot{E}_v + \dot{E}_p + \dot{E}_w - P_V + \Phi \tag{3.2}$$

The descriptions of various terms are given in section 2.3. The terms in the above equation have been carefully clubbed to represent the power balance in a simple manner as shown in figure 3.1.

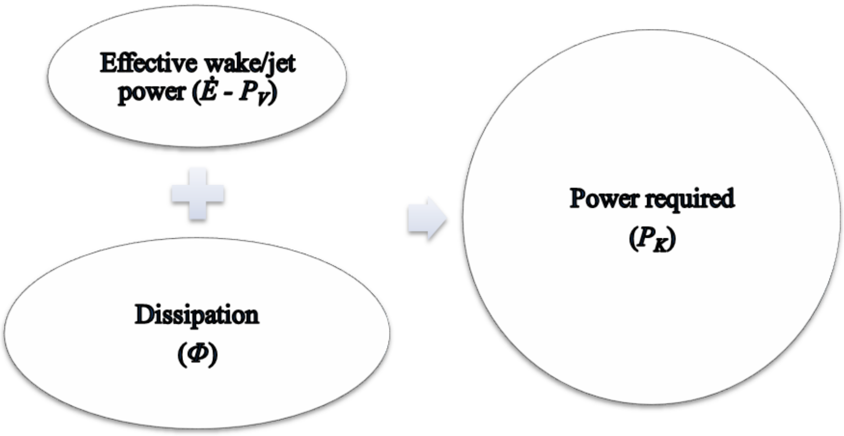

Figure 3.1: Power balance equation for cruise condition.

The P_V term can represent the effect of a heat source and P_V also importantly contributes explicitly to any effect due to compressibility that changes the effective wake/jet flow power. It should be noted that for incompressible flow, $P_V = 0$ as the velocity divergence $(\nabla.V)$ is zero.

The first task involves deciding the method to couple Power balance with CFD. One obvious method is to extract the flow field or the required data and to post process them after using a field interpolation (or any required interpolation) method. MATLAB provides powerful tools for most of the post-processing calculations.

3.1. LAMINAR FLOW OVER FLAT PLATE CASES

3.1.1. ISOLATED BODY SIMULATION

Analyzing the flow over isolated bodies in terms of power balance quantities is an important step towards understanding the possible power benefit. This is because an imaginary propulsor which can completely utilize the boundary layer/wake power for thrust production without affecting the upstream flow field would in fact only need to overcome the dissipation due to different phenomena like boundary layer losses, vortices, and shock waves. It is again reminded that each power term which adds up to the effective wake power are equally important and cannot be looked at separately to achieve a power benefit as explained earlier in section 2.3.

For the comparison of the results from laminar flat plate simulations, power balance quantities calculated based on Blasius solution would be used. These values can be found in [1] and will also be repeated here. Flow over a flat plate is considered for the following situation:

- The Plate has unit length and width.
- A length based Reynolds number (Re) of 100,000 is considered.
- ISA sea level conditions are assumed.

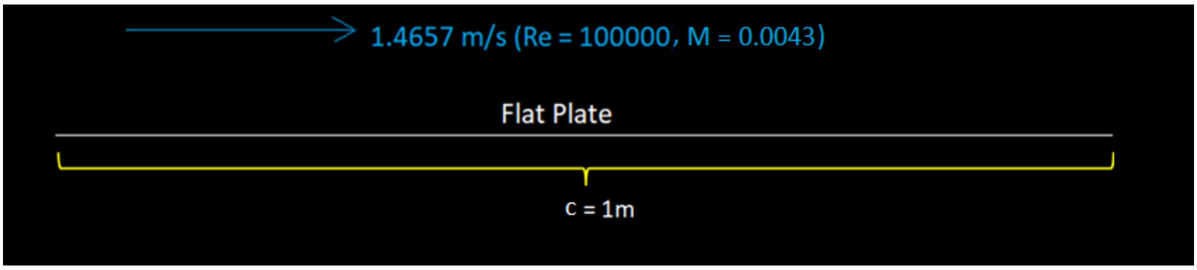

Figure 3.2: Isolated flat plate for laminar flow analysis. Example values given in SI units.

The Blasius solution gives different expressions for different boundary layer integral quantities including drag and dissipation coefficients [1, 33] which are repeated in table 3.1.

Quantity	Formula
Normalized boundary layer thickness $\left(\frac{\delta}{x}\right)$	$\frac{4.91}{\sqrt{Re_x}}$
Normalized displacement thickness $\left(\frac{\delta^*}{x}\right)$	$\frac{1.72}{\sqrt{Re_x}}$
Normalized momentum thickness $\left(\frac{\theta}{x}\right)$	$\frac{0.664}{\sqrt{Re_x}}$
Normalized kinetic energy thickness $\left(\frac{\theta^*}{x}\right)$	$\frac{1.044}{\sqrt{Re_x}}$
Local shear stress coefficient (C_f)	$\frac{0.664}{\sqrt{Re_x}}$
Local dissipation coefficient (C_Φ)	$\frac{0.261}{\sqrt{Re_x}}$

Table 3.1: Boundary layer quantities based on Blasius boundary layer solution for laminar flow over flat plate [1, 33].

It should be noted that for a flat plate, the boundary layer edge velocity (u_e) is taken equal to the freestream value (V_∞). Also, the viscous dissipation can be directly related to the kinetic energy thickness as follows:

$$\frac{1}{2}\rho_\infty V_\infty^3 \theta^*(x) = \int_0^x \rho_\infty V_\infty^3 C_\Phi \, dx \,. \tag{3.3}$$

This, of course, means complete removal of the pressure gradient term from equation 2.51 as described in subsection 2.5.2 and physically it implies a zero pressure gradient. As the pressure gradient is zero, the effective wake power can be directly written using the momentum and kinetic energy thickness values from table 3.1 as:

$$\dot{E} = \dot{E}_a = D(x)V_\infty - \Phi(x) = \frac{1}{2}\rho_\infty V_\infty^3(2\theta(x) - \theta^*(x)) = 0.142\rho_\infty V_\infty^3 x Re_x^{-\frac{1}{2}} . \tag{3.4}$$

It should be noted that the following equation for drag ($D(x)$) at a chordwise location x which is valid for a flat plate without a pressure gradient has been used in the above relation:

$$D(x) = \rho_\infty V_\infty^2 \theta(x) . \tag{3.5}$$

This further gives the drag power in terms of chordwise Reynolds number as:

$$D(x)V_\infty = 0.664\rho_\infty V_\infty^3 x Re_x^{-\frac{1}{2}} . \tag{3.6}$$

This gives a ratio of 21.39% for effective wake power with respect to drag power $\left(\frac{\dot{E}}{DV_\infty}\right)$ as mentioned in [1]. This means that an ideal-wake filling propulsor would have a 21.39% power saving when compared to a freestream operating propulsor. This theoretical limit can be compared to CFD results in different ways using the power balance terms described by Drela in [1]. The first method is to calculate the different power balance terms for isolated body after which a wake filling attempt by adding a propulsor in the aft of the plate can be done.

The CFD simulation is performed in Ansys Fluent using the laminar viscous model. An important step towards achieving correct simulation results is the creation of a sufficiently resolved mesh. The following criteria become important:

- Mesh fineness in the streamwise and normal directions.
- The spacing of mesh grid lines close to the body for boundary layer capturing.

The first criteria can be handled using a mesh convergence study. The second criteria on the other hand for a laminar flow can be determined based on the boundary layer thickness (δ) which can be approximated to be $3 \times \delta^*$ [34] as mentioned in table 3.1. The classical transformed y (normal to plate) coordinate which is used to obtain Blasius'equation from the boundary layer equations [34] is defined by:

$$\eta = y\sqrt{\frac{V_\infty}{\nu x}} . \tag{3.7}$$

Fluent guidelines [25] suggest that the y coordinate (normal to plate) of first grid points (just calling it y_{fgp}) must have a transformed coordinate η_{fgp} of less than or equal to one. That is:

$$\eta_{fgp} = y_{fgp}\sqrt{\frac{V_\infty}{\nu x}} \leq 1 . \tag{3.8}$$

The fgp subscript just refers to the first grid point. It should be noted that this guideline relates more to the accuracy of finite difference based velocity gradient calculation ($\frac{\partial u}{\partial y}]_{wall}$) required to obtain the shear stress. For the presently considered flow, a maximum first grid point spacing (y_{fgp}) of $0.0032c$ ($3.2mm$) is obtained. Thus, any spacing close to and below this value should give the best results. Next, the mesh convergence process will be discussed.

The seeding on the plate indeed would control the accuracy of the integral of the velocity gradient required to obtain plate drag. Thus, the seeding on the plate is used to analyze the fineness required in the streamwise direction. For the normal direction, the spacing of the first layer of cells next to the plate is maintained and the number of horizontal grid lines is controlled up to a distance of $0.05c$ (which is $3.2\times\delta$ according to Blasius solution) in the normal (y) direction. In total, results from eight meshes are analyzed. It should be noted that the size of the flow domain and the position of the plate in the domain are maintained. One of the eight meshes showing the flow domain and the used boundary conditions is given in figure 3.3. The mesh convergence details are shown in table 3.2:

The difference in the drag value measured for different meshes with respect to the Blasius solution can be attributed to numerical error. It should be noted that the Reynolds number of 100,000 considered here produces a boundary layer thickness (δ) equal to 1.56% of the plate length (c). Also, it is a well-known fact

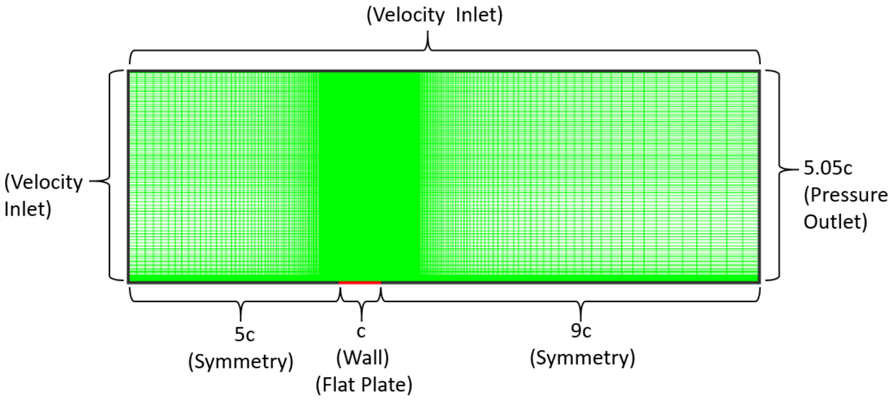

Figure 3.3: Isolated flat plate mesh 3 (details in table 3.2)- flow domain and boundary conditions.

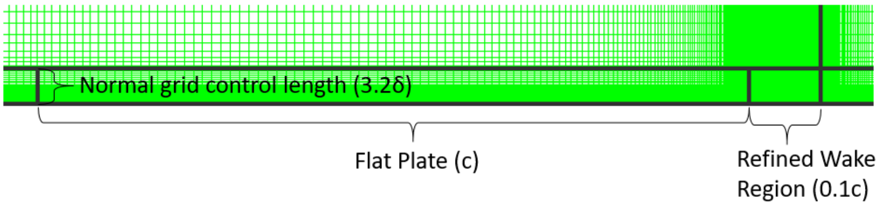

Figure 3.4: Magnified view near plate for mesh 8 (details in table 3.2) showing the immediate wake refinement and the normal grid refinement control length.

Name	Grid detail	Cell count	Plate drag coefficient (C_D)	Drag difference (w.r.t. Blasius solution)
Mesh 1	s=50 (uniform), n=50	40379	0.00838	0.0029%
Mesh 2	s=100 (uniform), n=50	53193	0.00842	-0.3949%
Mesh 3	s=150 (uniform), n=50	61090	0.00843	-0.5621%
Mesh 4	s=300 (uniform), n=50 and overall refinement	204352	0.00847	-1.0670%
Mesh 5	s=150 (uniform), n=25	50840	0.00841	-0.3218%
Mesh 6	s=150 (uniform), n=75	71340	0.00844	-0.6923%
Mesh 7	s=150 (uniform), n=100	81590	0.00844	-0.7051%
Mesh 8	s=150 (non-uniform), n=50 and immediate wake refinement	111005	0.00843	-0.5487%

Table 3.2: Laminar flow over isolated flat plate- mesh convergence details. 's' is the number of streamwise grid points on plate and 'n' is the number of grid points in normal direction till 0.05c from plate. $F_x = D$, $Re = 100{,}000$, and $M = 0.00430$.

that Prandtl's boundary layer equations involve the thin boundary layer assumption $\left(\frac{\delta}{c} << 1\right)$. Also, the actual Navier-Stokes equations are solved for Laminar flow in Fluent instead of the Prandtl's boundary layer equations. The thin boundary layer assumption however should apply for the present case and the obtained drag value does not change much for different mesh sizes and has a very low difference when compared to Blasius solution value (as can be seen from table 3.2), assuring that the selected Reynolds number is acceptable for the comparison. For the mesh convergence study, the difference between the drag values in the different meshes is the important criteria rather than the difference from Blasius solution drag result. The maximum difference in plate drag obtained in different meshes is just 1.08% (which is between the extreme values from mesh 1 and mesh 4). It should be noted that mesh 4 is highly refined compared to the others and still gives a very close plate drag value. This means that the considered meshes can already be considered acceptable and one of the meshes can be selected for further processing. Mesh 8 gives a comfortable choice as the immediate region behind the plate (up to a distance of 10% of plate length from the plate TE) is refined so that a propulsor volume could be modeled later if necessary. Thus, it will be employed for further studies. The profile from this specific mesh is compared to the profile from the Blasius solution in figure 3.5.

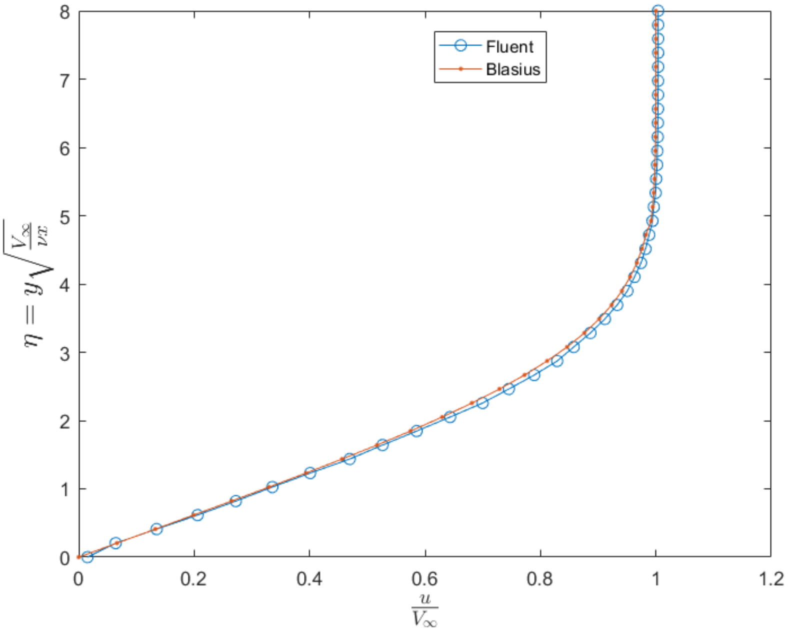

Figure 3.5: Comparison of boundary layer profiles at $X_{TP} = c$ for mesh 8 (details in table 3.2). $F_x = D$, $Re = 100,000$, and $M = 0.00430$.

Next, the power balance results would be presented. Since the flow conditions considered effectively result in an incompressible flow, the power balance for the flow over the isolated flat plate reduces to:

$$\dot{E} + \Phi = DV_\infty \tag{3.9}$$

$$\dot{E}_a + \dot{E}_v + \dot{E}_p + \Phi = DV_\infty \tag{3.10}$$

Next step, of course, is to define an appropriate control volume for the calculation of the power balance integrals. The power balance integrals, on the other hand, can be calculated either by performing Riemann sums obtained from discrete flow field values (cell values) or the discrete field values (cell or node values) could be used to generate an interpolated function which could be used further for numerical integration. Creation of an interpolated function was chosen for easier control over the exact location of the control volume boundaries. This is achieved using the scatteredinterpolant function in Matlab [35]. The scatteredinterpolant function contains different spatial interpolation schemes like linear, nearest-neighbor and natural-neighbor [35]. The linear scheme is used in all case in the present thesis unless stated otherwise. Numerical integration implemented in the used matlab functions consists of global adaptive quadrature method [35]. The CV shape chosen for analysis is given in figure 3.6. $X_{LP} = 4c$ and $Y_{TP} = 0.2c$ are the specific dimensions used for computing the power balance results. Power balance result is presented in figure 3.7.

The calculated $\dot{E}$ term at the plate TE is found to be 22.95% of the drag power. This is comparable to the value obtained from the Blasius solution based theoretical value of 21.39%. The minor difference is attributed to numerical error.

It is also important to calculate the power balance terms for different meshes to observe the sensitivity of different power balance integrals to the mesh geometry. Thus, the power balance integrals as formulated

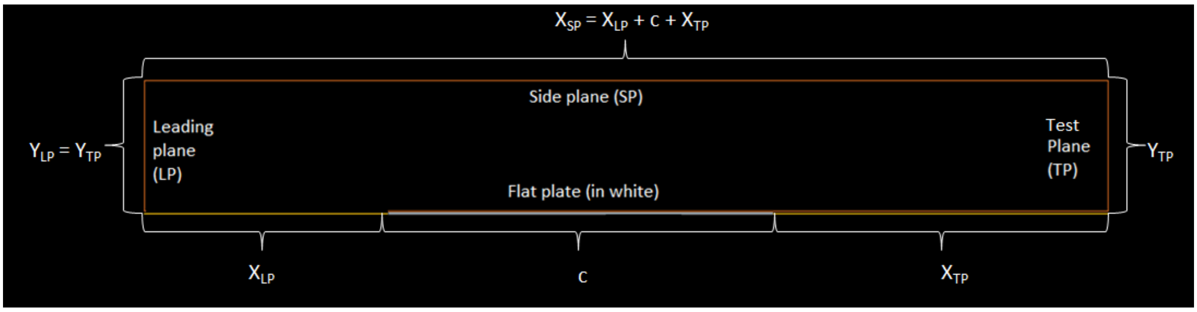

Figure 3.6: Partial CV (orange) in the computational domain for flow over flat plate. The complete CV is obtained by mirroring this partial CV about the yellow line.

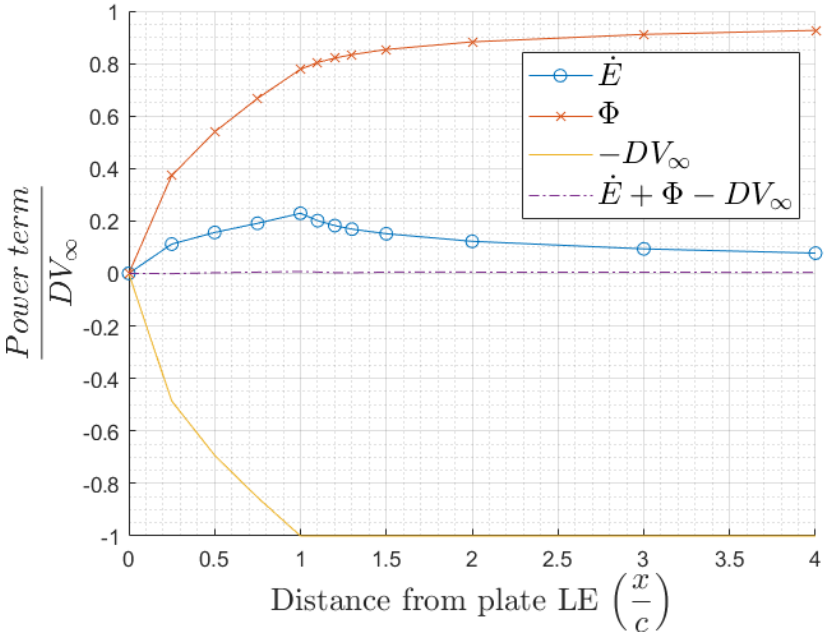

Figure 3.7: Power balance results for laminar flow over isolated flat plate using mesh 8 (details in table 3.2). $F_x = D$, $Re = 100{,}000$, and $M = 0.00430$.

in section 2.3 will now be reformulated (simplified) for the present case. All the required terms are found in equation 3.10. The CV considered is effectively two-dimensional and unit span can be assumed to calculate the power balance integrals. Assuming the plate leading edge to be the origin of the coordinate system with x along the plate and y normal to the plate, the integrals are listed next:

$$\dot{E}_a = 2\int_0^{Y_{TP}} \frac{1}{2}\rho(u - V_\infty)^2 u.dy \tag{3.11}$$

$$\dot{E}_v = 2\int_0^{Y_{TP}} \frac{1}{2}\rho v^2 u.dy \tag{3.12}$$

$$\dot{E}_p = 2\int_0^{Y_{TP}} (p - p_\infty)(u - V_\infty).dy \tag{3.13}$$

$$\Phi = 2\int_0^{Y_{TP}} \int_{-X_{LP}}^{X_{TP}} \mu\left(\frac{\partial u}{\partial y}\right)^2 .dx.dy \tag{3.14}$$

The factor of 2 in the above integrals is due to the fact that the CV in figure 3.6 only covers the upper half and needs to be mirrored with respect to the flat plate to obtain the lower half as well. The power balance values for different meshes are listed in table 3.3. As can be observed easily, the Φ value is very sensitive to the mesh

Mesh	$\frac{\dot{E}}{\rho_\infty V_\infty^3}$	$\frac{\Phi}{\rho_\infty V_\infty^3}$	$\frac{DV_\infty}{\rho_\infty V_\infty^3}$	$100 \times \frac{\dot{E}+\Phi-DV_\infty}{DV_\infty}$
Mesh 1	0.000957	0.003241	0.004200	-0.0365
Mesh 2	0.000962	0.003318	0.004200	1.6141
Mesh 3	0.000962	0.003033	0.004226	-5.3901
Mesh 4	0.000964	0.003396	0.004226	3.0706
Mesh 5	0.000967	0.003448	0.004200	4.8053
Mesh 6	0.000962	0.003344	0.004226	1.7581
Mesh 7	0.000962	0.003318	0.004226	1.5757
Mesh 8	0.000967	0.003267	0.004226	0.7597

Table 3.3: Laminar flow over a flat plate - Power balance results for different meshes with test plane at plate TE. $F_x = D$, $Re = 100,000$, and $M = 0.00430$.

(which is actually due to numerical error). Some minor changes in the mesh results is bad power balance results (and no real pattern can be identified). Although the results obtained above are after application of interpolation to the flow field, direct Riemann summing of discrete flow field results from Fluent are also similar. Thus, the viscous dissipation integral is not very reliable unless the power balance is correctly verified for the particular mesh. But identification of such meshes for complex bodies for many simulations would require a lot of labor. Also, it must now be clear why mesh 8 is chosen for the validation study (due to a low error in power balance). It should also be noted that the derivative $\frac{\partial u}{\partial y}$ has a sudden peaking behavior close to the body which can also result in bad interpolation in some cases as was observed for certain curved bodies which are covered in the upcoming sections. $\dot{E}$, on the other hand, is quite insensitive to the mesh. Thus, if Drag value (and hence the drag power) is correctly predicted, dissipation can also be directly obtained (for incompressible flow) from the power balance relation:

$$\Phi = DV_\infty - \dot{E}\,. \tag{3.15}$$

For a compressible flow, the P_V term as described in section 2.3 becomes significant and the following relation holds:

$$\Phi = DV_\infty - \dot{E} + P_V\,. \tag{3.16}$$

For the presently considered laminar flow over a flat plate case, it is also interesting to study the dependence of power balance terms on the size of the defined control volume. It is a known fact that in the absence of numerical errors, the control volume size should not produce any difference in the results. But, on the other hand, there could be some numerical error at each considered point in flow field output of CFD solutions and this could build up in different ways when an integration (or just Riemann sums for that matter) is performed. For the Fluent CFD results for laminar flow over flat plate case, this study is performed. It is rather simple to write the error formulas for each of the involved integral and analyze the resulting expression for any clues. Also, the values of the power balance integrals for different control volume sizes could be plotted to analyze how each term changes with the size. Thus, the control volume size dependence of the power balance terms is studied by analyzing the uncertainty propagation by using the standard deviation formula [36] and also by plotting the variation of the power balance terms with size of the TP. For a function $f(x, y, ...)$, if the uncertainty in the independent variables are δx, δy,..., then the error in $f(x, y, ...)$ is given by:

$$\delta f = \sqrt{\delta x^2 \left(\frac{\partial f}{\partial x}\right)^2 + \delta y^2 \left(\frac{\partial f}{\partial y}\right)^2 + ...} \tag{3.17}$$

This formula can be applied to the power balance integrals by the application of Leibniz integral rule. Since the limits of the integrals considered are independent of any flow field variable, the partial derivatives of the power balance integrals with respect to the flow field variables just reduces to the integrals of the respective partial derivatives of the integrands. The respective expressions for the different terms are next listed.

$$\dot{E}_a = \iint\limits_{TP} \frac{1}{2}\rho(u - V_\infty)^2 u.dS \tag{3.18}$$

$$\delta\dot{E}_a = \delta u \iint\limits_{TP} \frac{1}{2}\rho \underset{\approx 0 \text{ in freestream}}{\boxed{(3u^2 - 4uV_\infty + V_\infty^2)}} .dS \tag{3.19}$$

$$\dot{E}_v = \iint\limits_{TP} \frac{1}{2}\rho v^2 u.dy \tag{3.20}$$

$$\delta\dot{E}_v = \sqrt{\delta u^2 \left(\iint\limits_{TP} \frac{1}{2}\rho \underset{\substack{\approx 0 \text{ in} \\ \text{freestream}}}{\boxed{v^2}} .dS \right)^2 + \delta v^2 \left(\iint\limits_{TP} \rho u \underset{\substack{\approx 0 \text{ in} \\ \text{freestream}}}{\boxed{v}} .dS \right)^2} \tag{3.21}$$

$$\dot{E}_p = \iint\limits_{TP} (p - p_\infty)(u - V_\infty).dS \tag{3.22}$$

$$\delta\dot{E}_p = \sqrt{\delta p^2 \left(\iint\limits_{TP} \frac{1}{2}\rho \underset{\approx 0 \text{ in freestream}}{\boxed{(u - V_\infty)}} .dS \right)^2 + \delta u^2 \left(\iint\limits_{TP} \underset{\approx 0 \text{ in freestream}}{\boxed{(p - p_\infty)}} .dS \right)^2} \tag{3.23}$$

$$\Phi = \iiint\limits_{CV} \mu \left(\frac{\partial u}{\partial y} \right)^2 .d\vartheta \tag{3.24}$$

$$\delta\Phi = \delta \left(\frac{\partial u}{\partial y} \right) \iiint\limits_{CV} 2\mu \underset{\approx 0 \text{ in freestream}}{\boxed{\left(\frac{\partial u}{\partial y} \right)}} .d\vartheta \tag{3.25}$$

Also the net x-force integral is mentioned for a control volume with the side plane (SP) parallel to the global x direction along which the net x-force is assumed to act:

$$F_x = \iint\limits_{TP} -[(p - p_\infty) + \rho(u - V_\infty)u].dS + \iint\limits_{SP} -\rho(u - V_\infty)v.dS \tag{3.26}$$

$$\delta F_x = \left(\delta p^2 \left(\iint\limits_{TP} \underset{\substack{\neq 0 \text{ in} \\ \text{freestream}}}{\boxed{.dS}} \right)^2 + \delta u^2 \left(\iint\limits_{TP} \rho \underset{\approx V_\infty \text{ in freestream}}{\boxed{(2u - V_\infty)}} .dS + \iint\limits_{SP} \rho \underset{\substack{\approx 0 \text{ in} \\ \text{freestream}}}{\boxed{v}} .dS \right)^2 + \delta v^2 \left(\iint\limits_{SP} \rho \underset{\approx 0 \text{ in freestream}}{\boxed{(u - V_\infty)}} .dS \right)^2 \right)^{\frac{1}{2}} \tag{3.27}$$

It is very clear from the above equations that the terms in green which become very small (≈ 0) in freestream help reduce the error accumulation during integration. On the other hand, the red terms do not have this property and the respective terms are prone to error accumulation for increasing control volume sizes. Fortunately, the power terms are on the safe side and one may choose a big enough control volume as per requirement. It should be noted that viscous dissipation (Φ) term which was observed to be sensitive to the mesh geometry is also on the safe side in terms of control volume size selection. But the x-force integral is sensitive to the control volume size as some of the terms in its error equation are not zero in freestream (and thus no term to control the numerical error buildup). Plots of the power terms versus the test plane size (Y_{TP}) are given in figure 3.8 for the laminar flow over flat plate considered. It should be noted that $X_{TP} = 1.5 \times c$ has been used to obtain the result. This is done just for the sake of inclusion of some wake field also in the calculation.

As predicted by the uncertainty propagation formula the power terms are not very sensitive to the control volume TP size. But, on the other hand, it should be noted that the control volume must be defined in a way that the individual contributions to the wake power like $\dot{E}_a$, $\dot{E}_v$ and $\dot{E}_p$ stabilize (do not change with TP size). This is because otherwise, some power outflow would happen through the side plane and the simplification (side plane quantities are assumed to be zero) assumed in section 2.3 will not be valid.

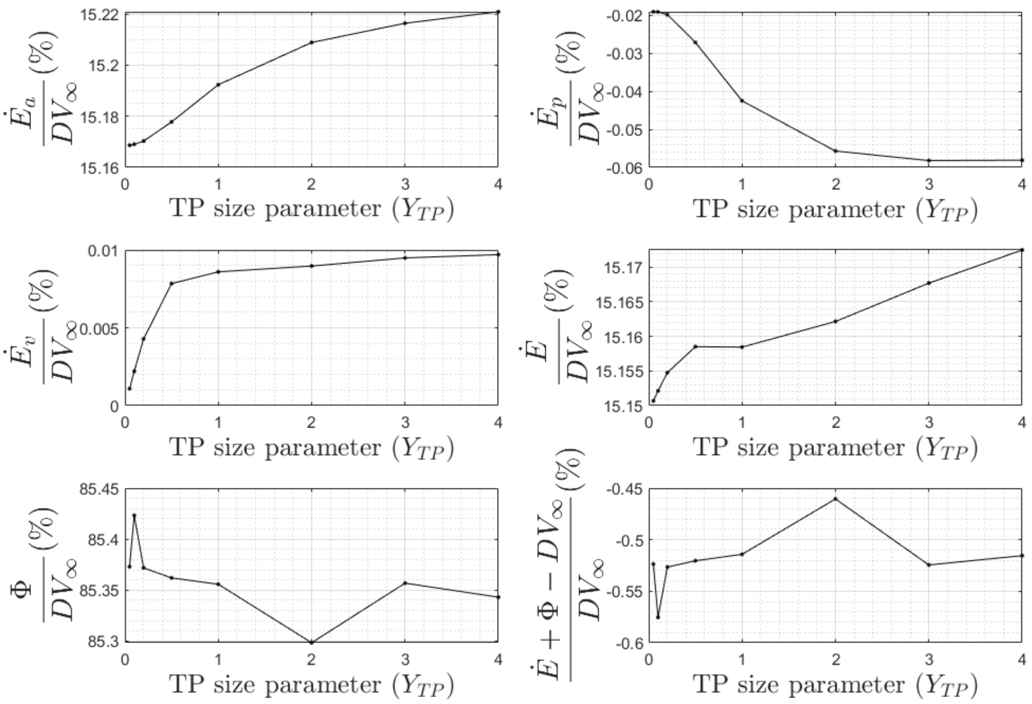

Figure 3.8: Laminar flow over isolated flat plate - Variation of power terms with test plane size parameter (Y_{TP} in figure 3.6) for $X_{TP} = 0.5c$; $F_x = D$, $Re = 100{,}000$, and $M = 0.00430$.

Next, the prediction about the error accumulation in the net x-force formula could also be verified. This is done by comparing the net x-force (which must be equal to the plate drag) with the drag value calculated by applying Newton's shear stress formula (as in figure 3.9). It can be observed that the net x-force term indeed is highly sensitive to the CV definition and could easily result in incorrect results if not used cautiously (actually it will not be used at any point in the thesis due to this except for some qualitative verification).

3.1.2. Approximate boundary layer/wake filler

The next interesting task would involve the study of how well the available wake power could be used to achieve a power saving. As already stated in section 1.1, real BLI/WI propulsors have the tendency to increase the drag when compared to the drag on the isolated body. Also, the propulsors have their own losses related to heat addition, frictional losses between moving parts, fluid viscous losses etc. Of course, propulsors can be modeled in a way to avoid some of these losses. Like for example, a pressure jump model over a small volume would only have viscous loss. Viscous loss could also be removed by imposing zero viscosity in specific regions (which is not very realistic but still good for the present study). On the other hand, controlling the effect of the propulsor on the surrounding flow field (which causes an increase in body drag) can be challenging.

The freestream conditions are kept the same as in the laminar flow over the isolated plate case and mesh 8 is used (mesh details in table 3.2) and a propulsor model is tried. The first attempt to create a propulsor model to fill the wake flow will be described in this sub-section. As the title suggests an approximate wake filler is created in this attempt. The 'approximate' word is just to suggest that the jet of the propulsor still contributes to a minor power loss (it is actually negligible). The net x-force is also negligible (zero) meaning there is no net acceleration or deceleration. The model consists of adding momentum sources to a propulsor volume. A propulsor modeled as a volume is more realistic than a disk-like model which would have a sudden pressure jump. Also, the drag increase effect is sensitive to the propulsor model (sub-section on perfect wake fillers (3.1.3) has some more useful results). Thus, a propulsor volume with momentum sources is chosen as a model for this study. The flat plate with the propulsor at the aft is shown in figure 3.10.

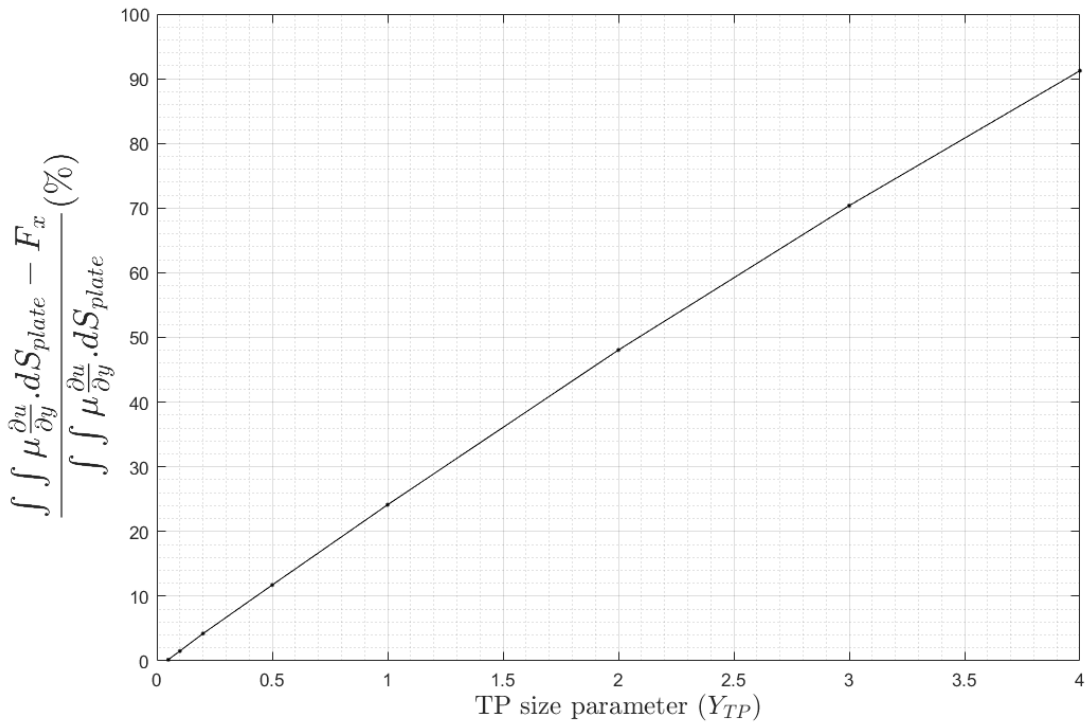

Figure 3.9: Laminar flow over isolated flat plate - Variation of net x-force term with test plane size parameter (Y_{TP} in figure 3.6) for $X_{TP} = 0.5c$; $F_x = D$, $Re = 100,000$, and $M = 0.00430$.

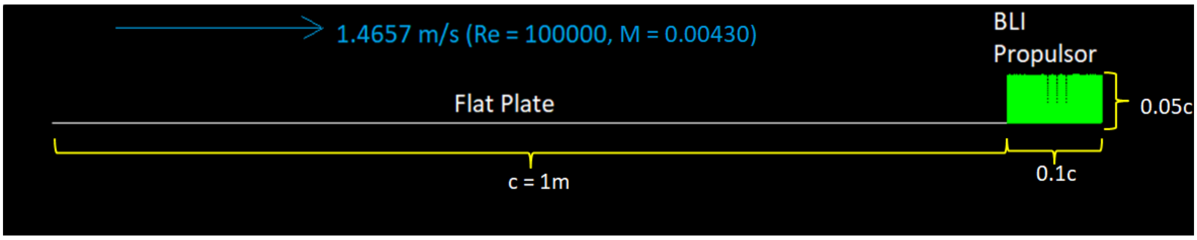

Figure 3.10: Flat plate with the propulsor at the aft. Some example values are mentioned in SI units.

For the fluid flow analysis, of course, laminar flow is considered and an x-momentum source is added in each horizontal layer of the propulsor volume mesh as shown in figure 3.11. The momentum source values can be calculated (for a zero viscous loss propulsor) using incompressible flow Bernoulli's theorem (with mechanical energy addition). For a propulsor as in figure 3.11, if each horizontal layer of cell has a cross-sectional area of S_l and is responsible for a force (only in x direction) delivery of F_l, and if the flow field pressure and x-velocity values in the cells of the first vertical layer (the entry cells in the propulsor horizontal layers) is P_{l1} and u_{l1} respectively, then for achieving a freestream total pressure at the end of the propulsor, the following equation must be valid for any horizontal layer (neglecting the vertical velocity component):

$$P_{l1} + \frac{1}{2}\rho u_{l1}^2 + \frac{F_l}{S_l} = P_\infty + \frac{1}{2}\rho V_\infty^2 \tag{3.28}$$

Momentum source values in Fluent are applied per unit cell volume and the x-momentum source (M_l) required in each cell layer can be calculated as:

$$\frac{F_l}{S_l} = \frac{M_l}{S_l} \times \sum_{cells\,in\,layer} Volume_{cell}\,, \tag{3.29}$$

$$M_l \times \Delta X = P_\infty - P_{l1} + \frac{1}{2}\rho(V_\infty^2 - u_{l1}^2)\,, \tag{3.30}$$

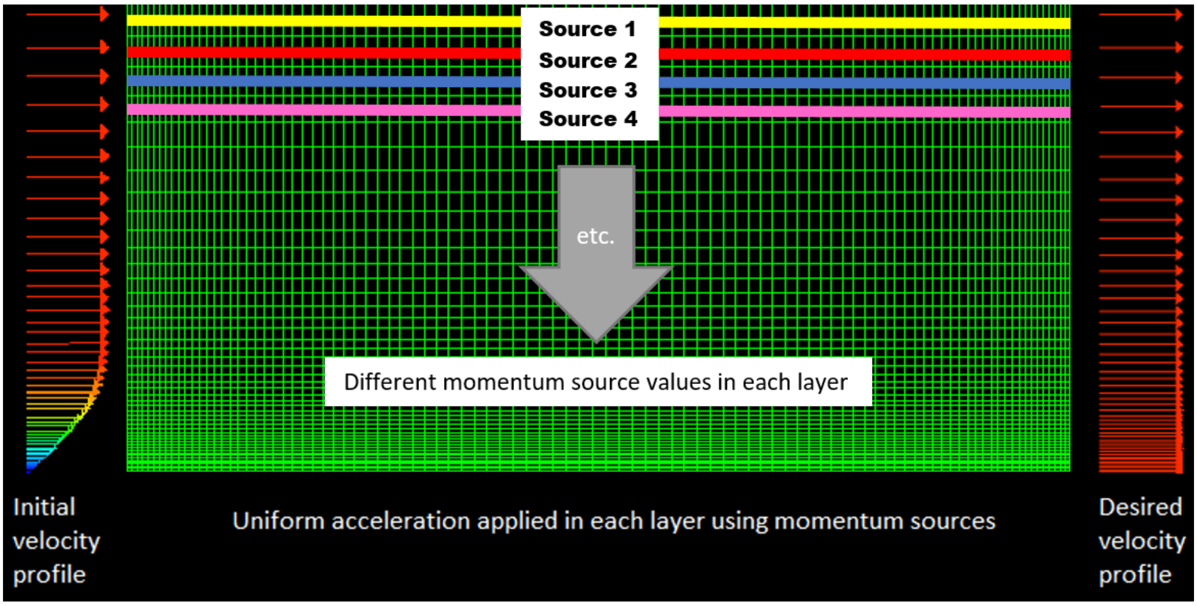

Figure 3.11: x-momentum source addition for approximate wake filler. The initial velocity profile shown is the profile from the end of isolated flat plate. It should be noted that real flow cannot produce such profiles for finite propulsor length due to flow continuity.

$$M_l = \frac{P_\infty - P_{l1} + \frac{1}{2}\rho(V_\infty^2 - u_{l1}^2)}{\Delta X}\,, \tag{3.31}$$

where ΔX is the distance through which the fluid is to be accelerated (or the total pressure change is to occur). The same value of ΔX will be used for all horizontal cell layers for simplicity. One obvious choice for ΔX is the propulsor length but this leads to another problem. The issue with setting ΔX equal to the propulsor length is the fact that the x-momentum source addition becomes independent of plate drag. Thus, the situation is as if there exists some specific propulsor length for which probably the propulsor thrust results in zero net x-force by equaling with plate drag and at the same time fills the wake. Thus, the approximate wake filler is designed to add just enough x-momentum source to make the thrust equal to the plate drag. Ideally speaking, if this process is done by an infinitely long propulsor without any loss, the pressure changes caused by the added x-momentum sources on upstream flow field would be negligible and the propulsor would have the sole effect of wake filling. This statement would also lead to the conclusion that sudden pressure jumps would have a higher drag increasing effect (at least in the case of flat plate). It should also be noted that the continuity equation requires that any acceleration in the x direction to happen along with a streamtube contraction which would change the y-velocity component as well. Thus, longer the propulsor (ideally infinitely long), lesser the change in y-component. But the present study considers a finite propulsor with a dimension as mentioned in figure 3.10 which as will be seen is good enough. Also, the viscous loss within the propulsor is removed by making the viscosity inside the propulsor zero as shown in figure 3.12. Thus, the ΔX value is updated using a Fluent UDF which is called every iteration. The drag obtained from Fluent is used to calculate the ΔX value required to achieve a zero net x-force (calculated as the difference between the plate drag and the force due to added momentum source) as shown in the chart in figure C.1.

The simulation result shows that the total pressure target is achieved very closely leading to a very low power (just 0.7% of the propulsor power) lost in propulsor jet. Such a low percentage is actually inseparable from the errors of the calculation and the approximate design is not really different from a perfect wake filler. But it is also clearly noted that the total pressure is almost (but not fully though it may have a negligible effect) recovered in figure 3.13. The velocity profile achieved is also shown in figure 3.14. The recovery is actually good to be considered as a fully recovered case which is highly evident from the wake energy deposition rate ($\dot{E}$) at the end of the propulsor. It should be notes that the velocity profile shown in figure 3.14 gives an indication that the axial kinetic energy deposition rate ($\dot{E_a}$) may still not be zero (though it is actually negligible). This is true and it is actually equal to 1.54% of the propulsor power (P_K) at the end of the propulsor. However, the pressure defect also causes ($\dot{E_p}$) to become negative at the end of propulsor and this ultimately reduces the $\dot{E}$ to an even lower value (0.7% of the propulsor power). This also shows that the selected propulsor length works well for wake filling at zero net x-force. As a final note, it is also mentioned that a ΔX of $0.14c$ is ob-

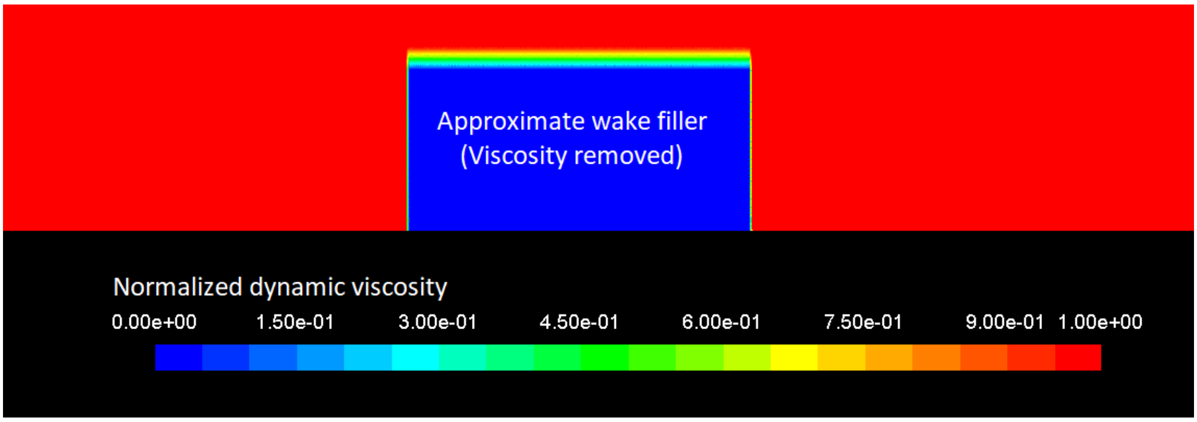

Figure 3.12: Vicosity removal in the propulsor (approximate wake filler). $F_x = 0$, $Re = 100,000$, and $M = 0.00430$.

tained as compared to the propulsor length of $0.1c$. One should note that one cannot just use this ΔX value to obtain a new complete wake filling propulsor. This is because the individual cell source values (which depend on propulsor length) affect the upstream flow field and ΔX value becomes dependent on propulsor length. Thus, the propulsor length may be made dynamic to iteratively obtain a ΔX value which satisfies all conditions. But this effort is unnecessary as the obtained propulsor is already good in terms of wake filling.

The complete power balance is shown in figure 3.16. The power balance after the propulsor is given by:

$$P_K = \dot{E} + \Phi - F_x V_\infty \tag{3.32}$$

The net force (F_x) is zero as set by the UDF. It should be noted that the sum of $\dot{E}$ and Φ for an isolated body (flat plate in this case) must exactly equal the drag power (DV_∞). But a maximum error close to 2% of propulsor power is observed between the drag power and the sum of $\dot{E}$ and Φ for the AWF. The maximum error in power balance after the propulsor is as low as 0.9% of propulsor power (which is just attributed to numerical error). It should be noted that the propulsor effect is felt on the upstream flow (which increases the drag). The drag power definition in this case in terms of freestream velocity is ambiguous. Thus, exact equality of drag power with the sum of $\dot{E}$ and Φ may not be true. On the other hand, this could also be due to a numerical error in the highly sensitive Φ integral. But no change is made to the mesh geometry when compared with the isolated case (where the Φ results are good in terms of power balance). More investigation is required regarding this (which may be complex due to the propulsor coupling). But this effect still causes no hindrance in proceeding with the main aim of the research. As a final note, it is also mentioned that the integral of P_K is also sensitive to the size of the boundary like the F_x integral. Thus, one may prefer using the momentum source values directly to obtain the power ($P_{k_{cell}} = F_{cell} \times u_{cell}$) by Riemann sums which is also not really free from the error buildup (but only one variable (u) would contribute to the error). But much difference is not found using this method for the present case as the size of the propulsor anyways seems small for any significant error buildup. Also, since the power balance works correctly, the obtained power value is acceptable.

Further, the power balance results are calculated using the CV defined in figure 3.15 (it should be noted that it has to be mirrored about the flat plate to get the full CV). The boundary around the propulsor is defined to exactly fit the propulsor geometry. A Y_{TP} of $3c$ is used for the power balance calculations. It can be observed from the power balance result plots that the total drag power before the propulsor is higher than the total power required to propel the configuration. Of course, this is due to the use up of the wake power by the propulsor. A power saving coefficient of 19.06% is achieved. The following observations are made:

- The approximate wake filler performs very well in terms of wake filling leaving a very low propulsor jet power loss of 0.7% which is actually comparable to numerical error.
- A power saving coefficient of 19.06% is obtained.
- Drag increase compared to the isolated laminar flow flat plate configuration is 3.26%.
- The surface dissipation increase compared to the isolated flat plate is 2.44%. This can be noted in figure 3.16 in which the isolated flat plate (laminar flow) results are also presented alongside.

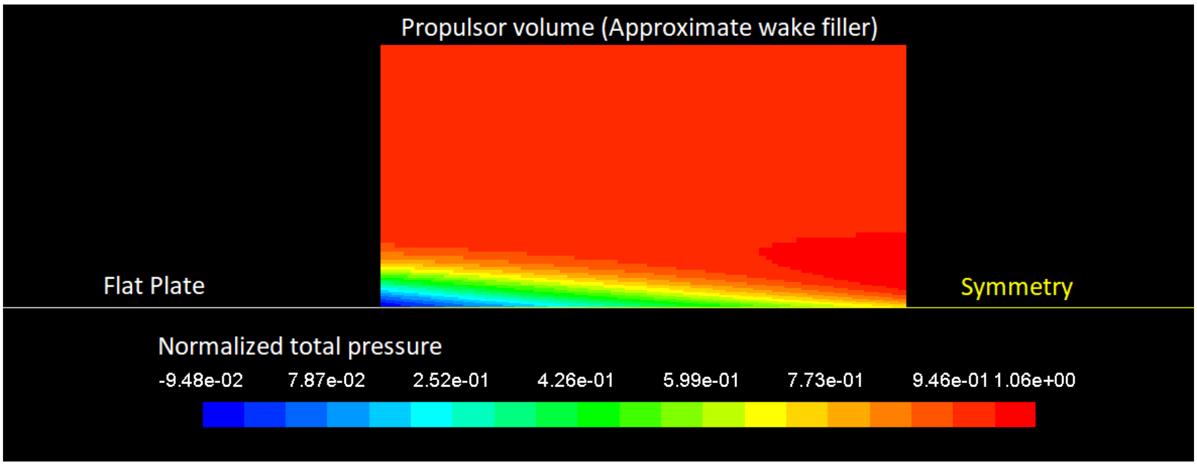

Figure 3.13: Total pressure contour in approximate wake filler. The total pressure is almost completely recovered to freestream value. $F_x = 0$, $Re = 100,000$, and $M = 0.00430$.

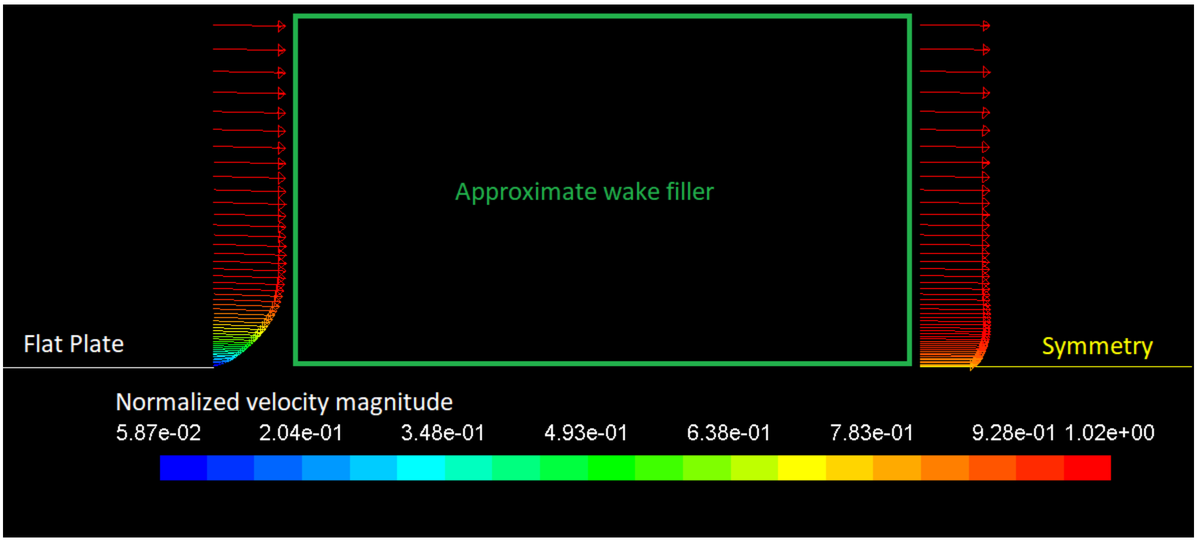

Figure 3.14: Velocity profile achieved using approximate wake filler. $F_x = 0$, $Re = 100,000$, and $M = 0.00430$.

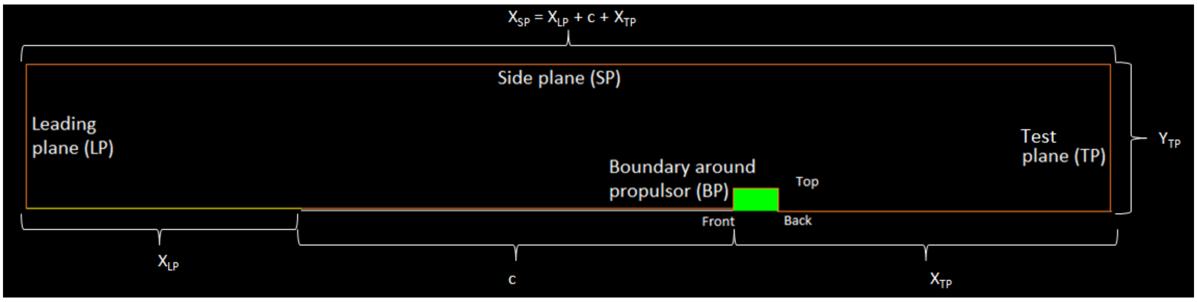

Figure 3.15: Control volume for flat plate with approximate wake filler.

3.1.3. PERFECT BOUNDARY LAYER/WAKE FILLERS

The previous study using the approximate wake filler clearly gives some insight into the usefulness of boundary layer ingestion. This subsection is moreover just another approach to fill the boundary layer/wake. The name perfect wake filler should not be confused with the performance of the propulsor. The main approach used is to just set a volume condition for velocity to restore the freestream flow field values wherever necessary. This approach makes it easy to run the simulations without further implementation difficulties.

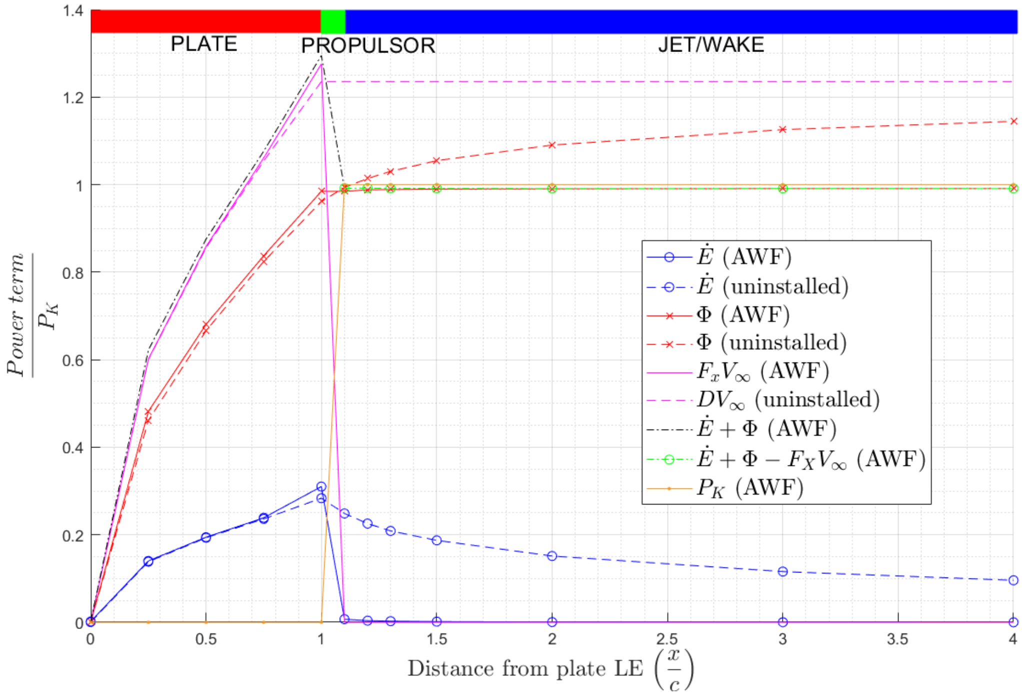

Figure 3.16: Power balance results for laminar flow over plate with approximate wake filler. $F_x = 0$, $Re = 100{,}000$, and $M = 0.00430$.

Again the freestream conditions are kept the same as in the laminar flow over the isolated plate case and mesh 8 is used (mesh details in table 3.2) with just creation of new fluid zone names (which does not change the mesh in anyways). This subsection would deal with two cases of perfect wake filling:

- Filling after some distance (= $0.1c$ from plate TE) 3.17.
- Filling immediately at the end of plate 3.18.

The filling is achieved by fixing the x-velocity to freestream value and the y-velocity to zero. This volume condition method is found to be very useful in studying the power saving when complete wake filling is done at different x-locations after the plate TE. This method clearly has a propulsor coupling effect like the previous case and the plate drag is increased compared to the isolated plate case. An important fact to note is that since the velocity values over a region is fixed to freestream value and since the outlet static pressure of the domain is set to freestream static pressure, the whole volume of velocity fixed region takes on the same value of static pressure. The incompressible nature of the flow is also a required condition for such a static pressure field. This is obvious because if the static pressure was not the same in the whole volume (with the fixed velocity), then the same value of velocity cannot exist in the downstream direction. Also, this is one reason why it is important to fix the whole volume after any required x-location (till the pressure outlet surface) instead of a small region after the required location. The validity of the boundary condition can easily be verified by comparing the mass flow through the domain with the mass flow through the same domain without fixing the velocity field anywhere (the mass flows are found to be equal as expected). As a final note, one can easily observe the major disadvantage of this method, which is the fact that a propulsor volume cannot be demarcated (and propulsor viscous loss cannot be removed). This leaves the complete analysis to just using the value of $\dot{E}$ and Φ to obtain the value of P_K based on power balance. Also, there is no doubt regarding the net x-force value which is of course zero. The reason is simple momentum conservation. It is easy to imagine that any selected control volume with TP in the wake filled volume and side plane in a pressure recovered region would result in zero net x-force by using the F_x equation as given in section 2.3. Also, these are the only two cases in which the F_x equation actually works without the significant numerical error buildup with control volume size (no real chance for error build up as the field values are literally fixed). The required power to achieve the filling is calculated as follows:

$$P_K = \dot{E} + \Phi \tag{3.33}$$

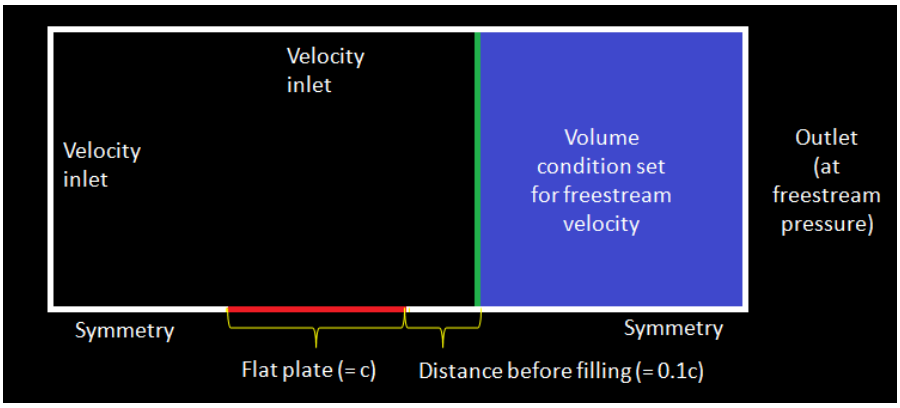

Figure 3.17: Perfect wake filler case 1 model.

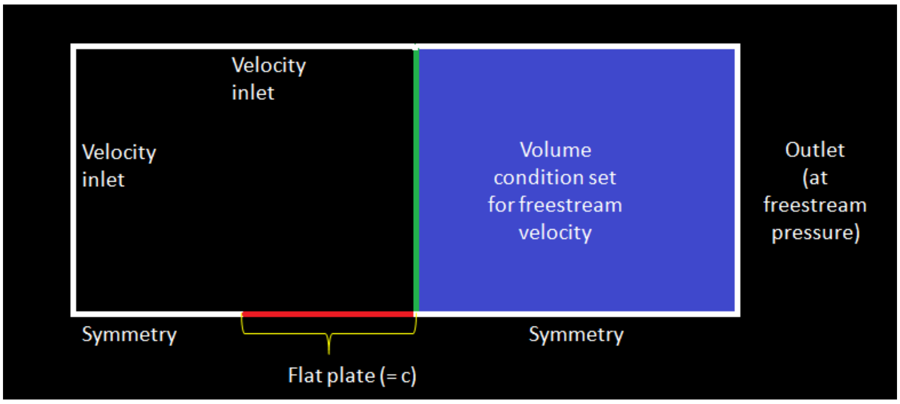

Figure 3.18: Perfect wake filler case 2 model.

Case Parameter	Isolated plate (Blasius)	Isolated plate (CFD)	Approximate wake filler (CFD)	Perfect wake filler - case 1 (CFD)	Perfect wake filler - case 2 (CFD)
C_D	0.008385	0.008428	0.008703	0.008687	0.009878
PSC (%)	-	-	19.06	17.62	13.26
$\dot{E}$ at configuration end (% w.r.t. DV_∞ or P_{prop})	21.39	22.95	0.7	0	0
Drag increase $\left(\frac{D_{iso}-D_{prop}}{D_{iso}}\%\right)$	-	-	3.26	3.07	17.12
Surface dissipation increase $\left(\frac{\Phi_{iso}-\Phi_{prop}}{D_{iso}V_\infty}\%\right)$	-	-	1.90	2.26	8.93
Net x-force (F_x)	Plate Drag	Plate Drag	0	0	0
Viscous loss in propulsor	-	-	0	Present	Present

Table 3.4: Comparison of different cases with laminar flow over flat plate. Note that the percent $\dot{E}$ value is taken with respect to the propulsor power P_K in wake filling cases and with respect to drag power (DV_∞) otherwise. $Re = 100,000$, and $M = 0.00430$.

The power saving results and comparison of the different propulsor models are all presented in table 3.4. It can be observed that the approximate wake filler has the best performance when compared with the perfect fillers. It is clear that the case 2 of perfect wake fillers has a much higher effect on the plate boundary layer flow causing the highest increase in drag (actually it is more appropriate to compare the surface dissipation as will be seen in subsequent chapters) leading to the worst performance. Also, it can be noted that the drag increase in case 1 of the perfect wake filler is lesser than that of the approximate wake filler but still case 1 perfect wake filler has a lower PSC value. This is because of the fact that the viscous loss in the approximate filler was removed but the same could not be done for case 1 perfect wake filler. Another interesting flow field to observe is total pressure recovery in the perfect wake fillers as shown in figures 3.19 and 3.19. Complete total pressure recovery is observed in both cases. Before finishing off, it is good to see that the sum of the surface dissipation increase and the PSC for the propulsors (Approximate wake filler and Perfect wake filler - case 2) are very close to the PSC_{ideal}. For Perfect wake filler - case 1, a minor under-prediction is expected (and observed) as the dissipation from plate TE till the filling plane would also need to be included to get to the PSC_{ideal} value.

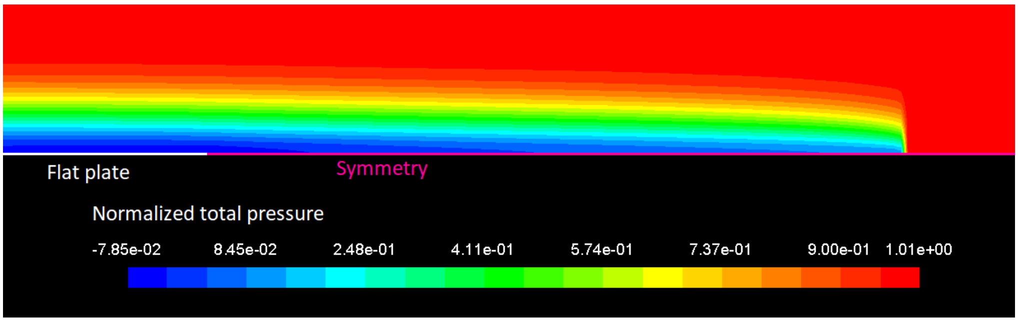

Figure 3.19: Perfect wake filler case 1 total pressure contour. $F_x = 0$, $Re = 100,000$, and $M = 0.00430$.

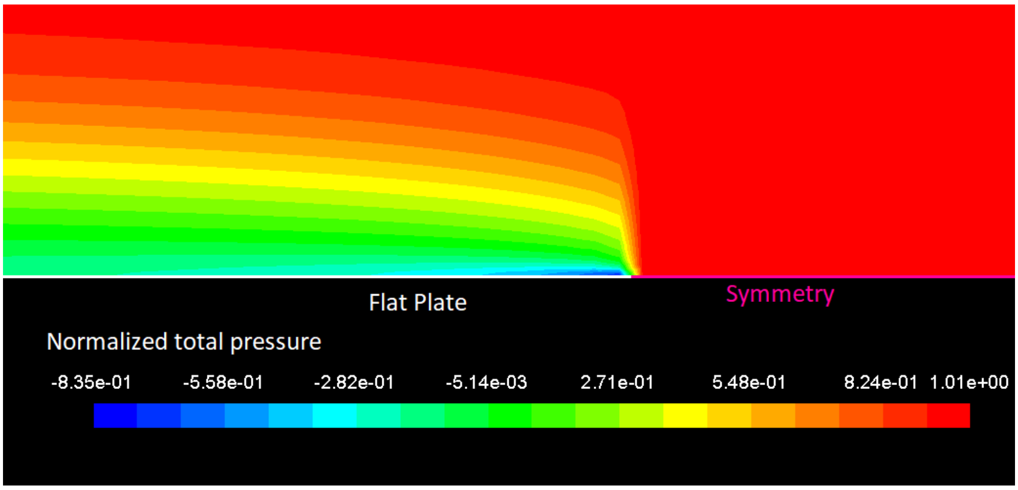

Figure 3.20: Perfect wake filler case 2 total pressure contour. $F_x = 0$, $Re = 100,000$, and $M = 0.00430$.

3.2. TURBULENT FLOW OVER FLAT PLATE CASES (RANS)

The study involving laminar flow over a flat plate gave a deep insight into the calculation of power balance quantities for the specific flow model. Also, the benefit of wake ingestion was made clear using the simple propulsor models. This section would deal with turbulent flow over a flat plate. Since most of the flow over real aircraft tends to be turbulent, it becomes important to perform a simple comparison of most commonly used turbulence models. A laminar model would also be compared alongside to mark the difference between laminar and turbulent cases. The flow conditions considered for the study are (see figure 3.21):

- The Plate is $2c$ long and has unit span.
- A plate length based Reynolds number (Re) of 10^7 is considered.
- ISA sea level conditions are assumed.

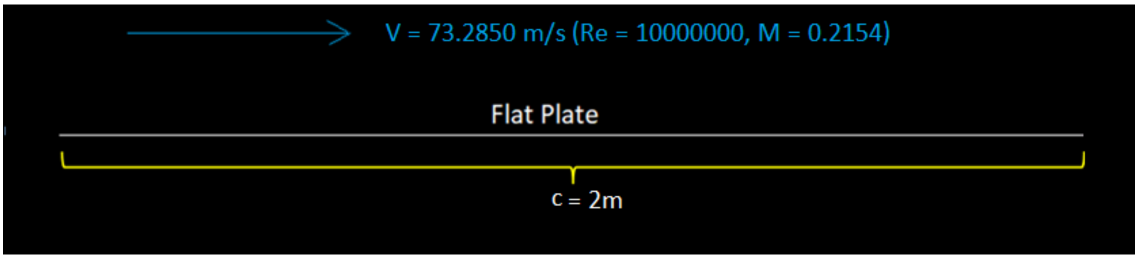

Figure 3.21: Flat plate with conditions for turbulent flow. Some example values are also provided in SI units.

It should be noted that to achieve a turbulent flow and at the same time keep the Mach number below 0.3 (for maintaining incompressible flow), the plate length has to be increased (from c to 2c where c is unit chord). Two turbulence models are compared, namely k-Ω-SST (Menter) and Spalart-Allmaras turbulence models. These were observed frequently in the literature [14, 15, 37]. The main aim is to compare the drag and the effective wake power. The only difference in the power balance integrals when compared to the laminar case is for the viscous dissipation and the shear stress. The inclusion of Reynolds stress becomes important in the calculation. The wall shear force and dissipation formulas are modified as follows (for Newtonian fluids):

$$F_{wall} = \iint_{wall} \left(\mu_l \left(\frac{\partial u}{\partial y}\right) - \rho \overline{u'v'}\right) .dA\,, \tag{3.34}$$

$$\Phi = \iiint_{CV} \left(\mu_l \left(\frac{\partial u}{\partial y}\right)^2 - \rho \overline{u'v'} \left(\frac{\partial u}{\partial y}\right)\right) .dV\,. \tag{3.35}$$

Since the considered turbulence models are eddy viscosity models, the Reynolds stress term can be further simplified using Boussinesq's assumption (for incompressible flow) [26]:

$$-\rho \overline{u'v'} = \mu_t \left(\frac{\partial u}{\partial y} + \frac{\partial v}{\partial x}\right)\,, \tag{3.36}$$

where the gradient $\frac{\partial u}{\partial y}$ is the dominant term and the wall shear force and viscous dissipation can be expressed as:

$$F_{wall} = \iint_{wall} (\mu_l + \mu_t) \left(\frac{\partial u}{\partial y}\right) .dA\,, \tag{3.37}$$

$$\Phi = \iiint_{CV} (\mu_l + \mu_t) \left(\frac{\partial u}{\partial y}\right)^2 .dV\,, \tag{3.38}$$

where μ_l is the laminar dynamic viscosity and μ_t is the Eddy viscosity and the x and y coordinates are taken tangential and normal to the body under consideration at any point (local coordinate system (same as the global coordinate system for the flat plate)). Unlike μ_l, μ_t is not a fluid property and depends on the flow [26]. One should also note that viscous dissipation obviously is always positive. It can be easily understood that the sensitivity of the viscous loss terms to the mesh or the control volume would be similar to the laminar case with the additional effect of the Eddy viscosity term. Also, a good reference for the solution to turbulent flow over flat plate is the one-seventh law. Like the laminar case, the values of the various boundary layer quantities derived using one-seventh law are listed in table 3.5. Similar to the laminar case, the effective wake power and drag power can be given as:

$$\dot{E} = \dot{E}_a = D(x)V_\infty - \Phi(x) = \frac{1}{2}\rho_\infty V_\infty^3 (2\theta(x) - \theta^*(x)) = 0.002\rho_\infty V_\infty^3 x Re_x^{-\frac{1}{7}}\,. \tag{3.39}$$

$$D(x)V_\infty = 0.016\rho_\infty V_\infty^3 x Re_x^{-\frac{1}{7}}\,. \tag{3.40}$$

The ratio $\left(\frac{\dot{E}}{DV_\infty}\right)$ obtained in this case is 12.50% as compared to the 21.39% for the laminar case (obtained using Blasius solution). Clearly, more of the power is spent in viscous dissipation in turbulent boundary layers. $\dot{E}$, on one hand, is the available mechanical power and is completely extractable at least theoretically. Φ, on

Quantity	Formula
Normalized boundary layer thickness $\left(\frac{\delta}{x}\right)$	$\frac{0.16}{(Re_x)^{1/7}}$
Normalized displacement thickness $\left(\frac{\delta^*}{x}\right)$	$\frac{0.02}{(Re_x)^{1/7}}$
Normalized momentum thickness $\left(\frac{\theta}{x}\right)$	$\frac{0.016}{(Re_x)^{1/7}}$
Normalized kinetic energy thickness $\left(\frac{\theta^*}{x}\right)$	$\frac{0.028}{(Re_x)^{1/7}}$
Local shear stress coefficient (C_f)	$\frac{0.027}{(Re_x)^{1/7}}$
Local dissipation coefficient (C_Φ)	$\frac{0.0120}{(Re_x)^{1/7}}$

Table 3.5: Boundary layer quantities based on one-seventh for turbulent flow over flat plate [33]. It should be noted that the value of dissipation coefficient and kinetic energy thickness values were derived and have not been taken from the reference.

the other hand, results in the conversion of mechanical energy to thermal energy and complete re-extraction of this is impossible according to the second law of thermodynamics (maximum extractable being when a theoretical Carnot heat engine is used [23]). The present section will only deal with mechanical energy re-extraction. Theoretical aspects of thermal management with regard to boundary layer/wake ingestion are given in [2]. The same control volume geometry used for power balance analysis in the laminar case is used for all turbulent cases (only the dimensions are a bit different (importantly the plate is $2c$ long)). It should be noted that a different mesh is used to satisfy the $y^+ < 1$ condition for turbulent flows (for k-ω-SST and SA models). The power balance results of the different cases are presented in figure 3.22. The minor errors observed in power balance results are numerical errors mostly contributed by Φ due to its high sensitivity to mesh and solver numerics (as mentioned earlier). It was also noted that the value of $\dot{E}$ converged faster than Φ (meaning the simulation had to be run for more iterations for less error in Φ). As a final note, the dimensions of the control volume used for obtaining the power balance results are $X_{LP} = 4c$ and $Y_{SP} = 2c$ (but results are not really sensitive to these as proved earlier). Further, the comparison of important results from different models is presented in table 3.6.

Quantity / Case	C_D	$\left(\frac{\dot{E}}{DV_\infty}\right)_{TE}$ (%)	$\left(\frac{\Phi}{DV_\infty}\right)_{TE}$ (%)
Turbulent (One-Seventh law)	0.0064	12.50	87.50
Turbulent ($k-\omega-SST$)	0.005787	10.33	89.46
Turbulent (Spalart-Allmaras)	0.005989	10.07	90.59
Laminar	0.0008313	21.79	77.45

Table 3.6: Comparison of power balance results for different flow models for flow over flat plate. $F_x = D$, $Re = 10{,}000{,}000$, and $M = 0.2154$.

It is clearly observed from the power balance results that the turbulent flow over flat plate results in a much higher drag and percentage wise the wake power is lower than in the laminar case. As such the results from both the investigated turbulence models are very close to each other but they result in a higher drag coefficient value than that predicted by the One-Seventh law. A turbulence viscosity ratio of 10 is used in both cases for the simulation and a freestream turbulence intensity of 1% is used in case of k-ω-SST model. The resulting modeling difference can be suggested as a reason for the difference in results when compared to one-seventh law. In any case, the value of the wake power $\dot{E}$ is close to the result from the one-seventh law percentage wise.

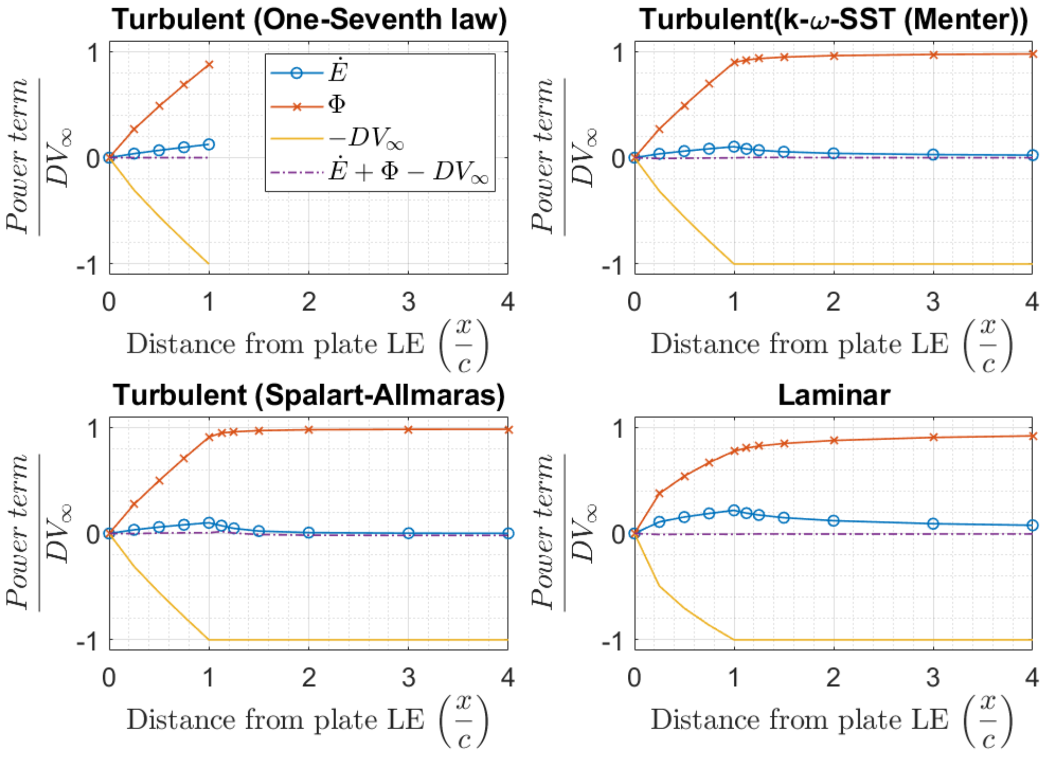

Figure 3.22: Power balance plots of different models of flow over a flat plate. $F_x = D$, $Re = 10{,}000{,}000$, and $M = 0.2154$.

3.3. NACA0040 BODY OF REVOLUTION CASE (RANS AND EULER-IBLT)

An interesting case to study power balance can be found in the work by Sabo and Drela [12]. This case contains an extreme geometry which can be used to study the accuracy of the Euler-IBLT solver when compared to the RANS solver.

3.3.1. DISSIPATION ANALYSIS OF ISOLATED BODY (RANS)

Isolated body analysis as already shown through the example of flat plate simulations can give a good indication of the possible BLI/WI benefit. Also, it becomes important to compare the RANS and Euler-IBLT codes before the actual studies. An analysis of the solution accuracy between different solvers requires clarity in predicting the laminar to turbulent transition location. For example, a fully turbulent RANS simulation may not be the most appropriate when comparing with a solver like MTFLOW. Although MTFLOW uses an e^N transition prediction method, it is possible to set a forced transition location. Also, Sabo and Drela [12] perform certain analyses by adding a trip at 15% chord length of the body. This location seems a good starting point for comparison. The intention although is not to compare with the experimental work of Sabo and Drela [12] as their work also contains a strut attached to the NACA0040 BOR whose drag was not corrected for [12].

Fluent simulation is performed by dividing the domain into a laminar and a turbulent region with the dividing line connecting the NACA0040 BOR at 15% chord. The k-ω-SST (Menter) turbulence model is used for the turbulent region. Freestream turbulence parameters are calculated by considering the flow to be internal flow in wind tunnel (using data from [12]) and following standard guidelines given in [25] for such internal flows. The flow and geometry details are given in figure 3.23. It should be noted that the domain size selected is nearly 20 times the body length in the front, aft, and normal directions.

The power balance terms are obtained and plotted (figure 3.24) for various locations in the wake starting from the trailing edge of the body. It should be noted that the viscous dissipation is not calculated directly from the flow field as done for the cases of flat plate. It is instead directly obtained from the power balance

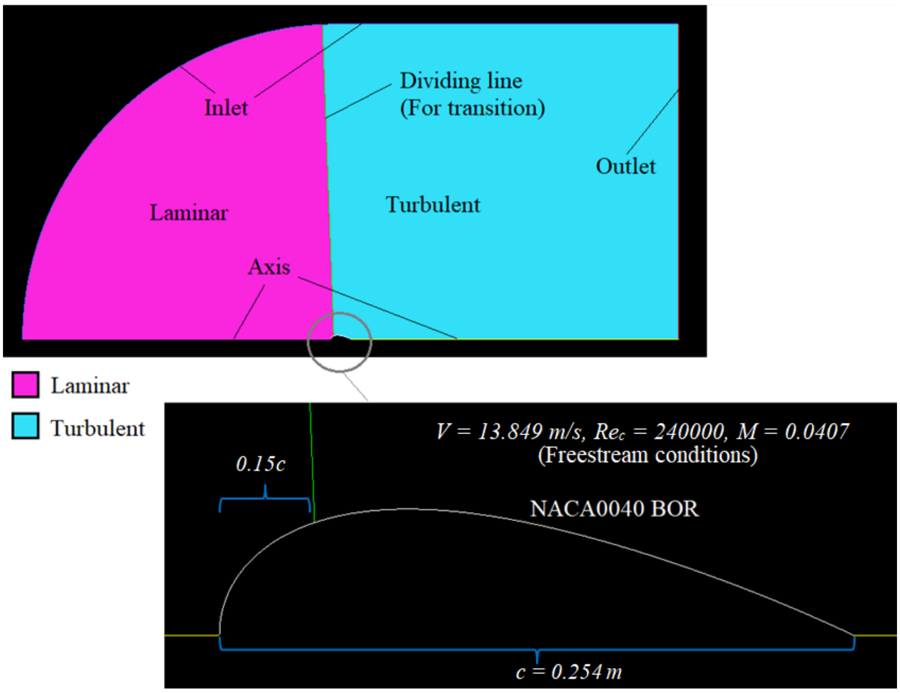

Figure 3.23: Flow domain and geometry details for NACA0040 body of revolution simulation (RANS).

relation (equation 2.11). Also, the composition of the mechanical power flow out of CV ($\dot{E}$) is shown in figure 3.25.

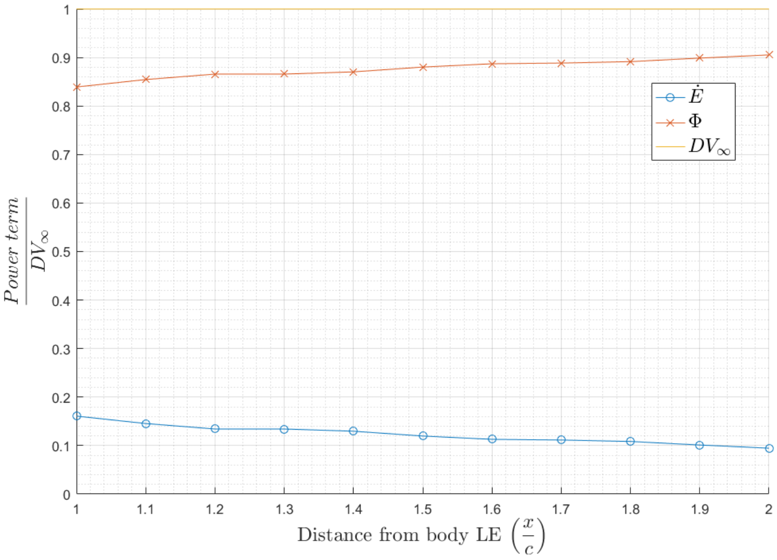

Figure 3.24: Power balance results for NACA0040 body of revolution simulation (RANS). $F_x = D$, $Re = 240{,}000$, and $M = 0.0407$.

As can be understood, for incompressible flows, $\dot{E}$ is a good indicator of the maximum extractable power in a BLI configuration, the highest possible benefit being at the body trailing edge. It should be observed that the P_V term as introduced in section 2.3 has negligible contribution due to incompressibility. Important values for comparison of the flow solvers are tabulated later in table 3.7.

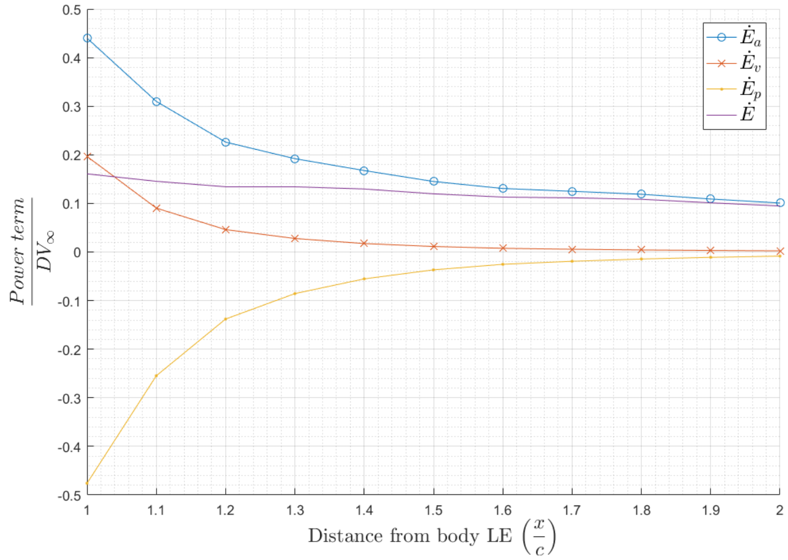

Figure 3.25: $\dot{E}$ composition from the flow field of NACA0040 body of revolution simulation (RANS). $F_x = D$, $Re = 240,000$, and $M = 0.0407$.

3.3.2. DISSIPATION ANALYSIS OF ISOLATED BODY (EULER-IBLT)

Next, the body is analyzed using the Euler-IBLT solver with similar settings. The laminar to turbulent transition is achieved using a forced transition setting in which the transition location is fixed at $0.15c$. Since this is an Euler-IBLT solver, the dissipation is calculated directly by integrating the dissipation term in equation 2.51 along the boundary layer and wake as necessary. It should be clearly observed that unlike the flat plate, the momentum defect area ($\rho_e u_e^2 \theta b$) at the body TE does not represent the drag (due to non-freestream pressure at the location). Thus, power balance relation has to be applied to obtain the effective wake power from the viscous dissipation (Φ). MTFLOW itself uses the widely applied Squire-Young formula [38] to obtain the viscous body drag [21] which is a far-field approach to drag prediction. Since swirl is not modeled in the study, no additional drag needs to be accounted for. Thus, the viscous dissipation is obtained as:

$$\Phi(x) = \int_0^{x_n} \rho_\infty u_e^3 C_\Phi b \, dx_n \,, \tag{3.41}$$

where x_n denotes the local body coordinate (parallel to the body). Also, it should be noted that MTFLOW (at least in the present version) uses inlet velocity and density (just V_∞ and ρ_∞) based normalization for the local dissipation coefficient C_Φ instead of boundary layer edge quantities (u_e and ρ_e) as observed in the source code. This is anyways convenient as the angle of the boundary layer profile with respect to global coordinates does not confuse the integration. Also, the density in the present case is anyways constant due to incompressibility. Although the kinetic energy defect term has been used commonly in literature for loss calculation [6, 28, 39], it would be more appropriate to use the viscous dissipation for both incompressible and compressible flows as it matches the definition of Φ as given in section 2.3 and as described in [1]. For incompressible flow, the kinetic energy defect very closely matches the dissipation as observed from figure 3.26. It should be noted that for the axisymmetric case, the $\frac{1}{2}\rho_e u_e^3 b \theta^*$ can be called the kinetic energy defect area as in [21] (which is analogous to kinetic energy defect for a 2D case).

The comparison of different quantities of interest from RANS and Euler-IBLT solvers are provided in table 3.7.

It can be observed that the error in drag is moderate for the geometry. The possibility of breakdown of the assumption of constant pressure across the boundary layer is high for the chosen geometry. Thus, MTFLOW may be less applicable to such cases. But as can be observed, the dissipation value on a percentage basis has a lower difference. The results from the present case highlight the extent of validity of the assumptions used in MTFLOW solver.

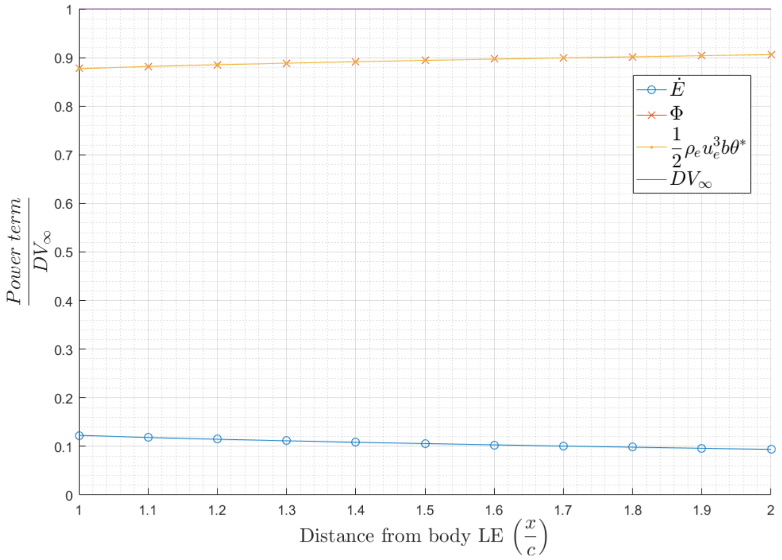

Figure 3.26: Dissipation analysis for NACA0040 body of revolution (Euler-IBLT). $F_x = D$, $Re = 240{,}000$, and $M = 0.0407$.

Solver Quantity	RANS	Euler-IBLT	Difference
Drag coefficient	0.05433	0.05823	-7.19 %
$\left(\frac{\dot{E}}{DV_\infty}\right)_{TE}$ (%)	16.08	12.27	3.81
$\left(\frac{\Phi}{DV_\infty}\right)_{TE}$ (%)	83.92	87.72	-3.81

Table 3.7: Comparison of results from RANS and Euler-IBLT solvers for NACA0040 BOR. $F_x = D$, $Re = 240{,}000$, and $M = 0.0407$.

3.4. FUSELAGE GEOMETRY CASE (RANS AND EULER-IBLT)

This section contains the comparison of the RANS and Euler-IBLT solvers for a transonic flow case with a fuselage geometry. The section also covers the exergy analysis of the fuselage geometry using the solution data from the RANS solver. Also, the fuselage geometry that would be defined in this section would also form the baseline case for the design space analysis in the subsequent chapter.

The possible configurations for boundary layer ingestion is indeed a question which needs to be analyzed carefully. Different choice of novel aircraft concepts like the D8 Double bubble aircraft by MIT, STARC-ABL by NASA, or the propulsive fuselage concept by Bauhaus Luftfahrt are possible. Isikveren et.al. [22] provide a detailed explanation regarding the selection process involved in filtering out the novel propulsive fuselage concept. A conceptual system level analysis including various aspects are covered. Thus, the resulting fuselage dimensions and the flight conditions from the work will be adapted as per necessity in the present study.

The fuselage geometry is considered to be axisymmetric which is a simplification necessary to perform the design space study using MTFLOW. On the other hand, this simplification does prevent one from capturing important details like circumferential flow distortion but it is accepted for the present study as it is still a good model to study the power consumption. Also, the propulsor design is out of scope and special simplifications will be applied as earlier to model the propulsor. The fuselage geometry details and the flight condition details can be found in table 3.8. The axisymmetric fuselage geometry is given in figure 3.27.

3.4.1. MESH AND SOLVER SETTINGS

Before moving on to fixing a transition location and beginning a comparison study of the solvers it is necessary to analyze the mesh and solver settings necessary for appropriate solution.

Parameter	Value
Fuselage diameter	6.205 m (always)
Fuselage length	69 m
Fuselage slenderness $\left(\frac{L_{fuselage}}{D_{fuselage}}\right)$	11.12
Fuselage afterbody slenderness $\left(\frac{L_{afterbody}}{D_{fuselage}}\right)$	2.5
Fuselage forebody slenderness $\left(\frac{L_{forebody}}{D_{fuselage}}\right)$	1.67
Fuselage forebody geometry	ESDU I (paramsh = 0.9)
Fuselage afterbody geometry	ESDU II (paramsh = 0.5)
Flight Mach	0.8
Reynolds number (length-based)	408,471,672
Flight altitude	FL350
Flight ambient temperature	ISA+10 (= 228.738 K)
Flight ambient pressure	23831.84 Pa
Propulsor length (if present)	1 m (always)
Propulsor Diameter (if present)	6.205 m (= $D_{fuselage}$)

Table 3.8: Baseline fuselage geometry and flight conditions. The quantities mentioned as 'always' are not changed throughout the thesis.

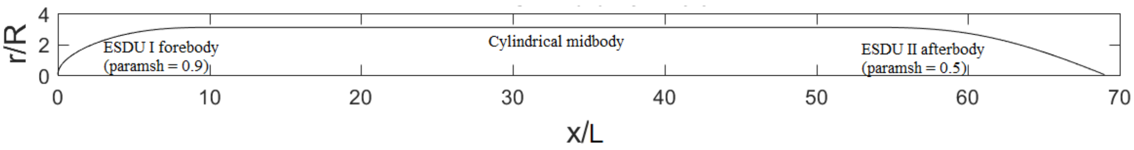

Figure 3.27: Baseline fuselage geometry for design space exploration.

RANS solver settings

RANS solver is always used in axisymmetric mode as the intention is to verify the accuracy and validity of the solutions from the Euler-IBLT solver (which has only axisymmetric modeling). The k-ω-SST (Menter) [40] turbulence model is used in the simulations. The usual boundary conditions used for isolated body simulations are given in figure 3.28. The freestream turbulence intensity is fixed at 0.1 as recommended by Spalart and Rumsey [41] and a viscosity ratio of 2 is used (set in the farfield boundary condition). Green-Gauss cell based method is used in the solver method setting. Further, coupled algorithm is used along with pseudo-transient setting which allowed for a fast convergence. The viscous heating, compressibility effects, production Kato-Launder, production limiter options are switched on in the turbulence model panel. The wall $y+$ is always verified to be below 1. As a final note, molecular viscosity is calculated using the three-coefficient Sutherland law. All the residuals are ensured to reduce at least below a value of 10^{-6} for all simulations.

Next, moving on to the mesh. Three different meshes are used and results are obtained. These are shown in tables 3.9 and 3.10. The meshes are created by systematically increasing the number of grid points in the streamwise and normal directions (giving equal importance to special locations such as the points on the fuselage). It should be noted that the flow is considered to be fully turbulent for these cases and no laminar-turbulent splitting is applied for simplicity. The values of obtained drag coefficients for the three meshes are very close indicating that the number of cells is already sufficient. The values of the power balance and exergy analysis terms on a percentage basis show mild fluctuations between the three meshes. Important terms like the dissipation (Φ) and the anergy rate ($\dot{A}$) show closer values for the medium and the fine meshes. The medium mesh is accepted as the results are satisfactory and the computational power required is acceptable.

Quantity / Mesh	Cell count	C_D	$\dot{E}_a$	$\dot{E}_v$	$\dot{E}_p$	$\dot{E}$	P_V	$\dot{E}-P_V$	Φ
Coarse	191874	0.07288	55.47	17.37	-79.48	-6.63	-20.86	14.22	85.78
Medium	422154	0.07282	55.78	17.71	-80.81	-7.34	-20.12	12.79	87.21
Fine	608584	0.07278	55.28	17.35	-79.24	-6.61	-19.81	13.20	86.80

Table 3.9: Mesh considerations for baseline fuselage RANS (fully turbulent) simulations (Power balance terms). Power terms are given as a percentage of drag power and shaded columns contain quantities obtained from power balance. $F_x = D$, and $M = 0.8$.

Quantity / Mesh	Cell count	C_D	$\dot{A}$	$\dot{\varepsilon}$	$\dot{\varepsilon}_{th}$	$\dot{A}_{thm}$
Coarse	191874	0.07288	86.92	13.07	19.71	5.66
Medium	422154	0.07282	90.03	9.97	17.31	5.68
Fine	608584	0.07278	88.99	11.01	17.62	5.69

Table 3.10: Mesh consideration for baseline fuselage RANS (fully turbulent) simulations (Exergy analysis terms). Power terms are given as a percentage of drag power and shaded columns contain quantities obtained from exergy analysis. $F_x = D$, and $M = 0.8$.

Euler-IBLT solver settings

For the Euler-IBLT solver, the mesh is made as dense as possible as it is very cheap anyways. For example, the code by default allows a maximum of 45 streamlines which is used for the study. This limit can be easily tweaked in the source code but the results did not change much for more number of streamlines tried (= 70). Next, the number of streamwise grid points is kept at 300. Though this is not the limit, it seemed sufficient for the overall domain sizes involved. The grid setting was chosen to bunch at stagnation lines. All the mesh settings need to be fixed in the mtset application.

The CFD solver application mtsol is used with the blended entropy equation (at the leading edge to prevent spurious losses) and momentum equation (elsewhere) setting (Smom=4 in the solver). The mtflo application is called for adding propulsor grid if necessary. It is again mentioned that the Euler-IBLT solver runs only in axisymmetric mode. Also, all the simulations are steady state.

The solver is compiled and run in Windows 10 operating system using Windows subsystem for Linux (WSL). The plot display is achieved using Xming X server application. For the automated studies (like DSE and optimization), when the display was not necessary, the X virtual framebuffer (Xvfb) application is used which allows the solver to run without display output. The applications are directly called from Matlab. The solver is compiled and used in double precision which worked without any issues. Single precision seemed to have convergence issues when solving in viscous mode.

3.4.2. DISSIPATION AND ANERGY ANALYSIS OF ISOLATED BODY (RANS)

The analysis of the baseline fuselage geometry again requires a decision regarding the laminar to turbulent transition location. Since the Euler-IBLT solver will be free to allow a natural transition (based on the e^N method) during the design space studies, the natural transition location obtained in MTFLOW is directly used to set the transition location in the RANS simulations. Thus, the transition location is obtained from the Euler-IBLT simulation first. An N_{crit} value of 9 is used for all the simulations. For the baseline fuselage, the transition location is found to be at $0.0358L_{fuselage}$. As done in the case of NACA0040 BOR, the domain is divided into two portions one with laminar and the other with the turbulent flow with the separation line at the assumed transition location. This is shown in figure 3.28.

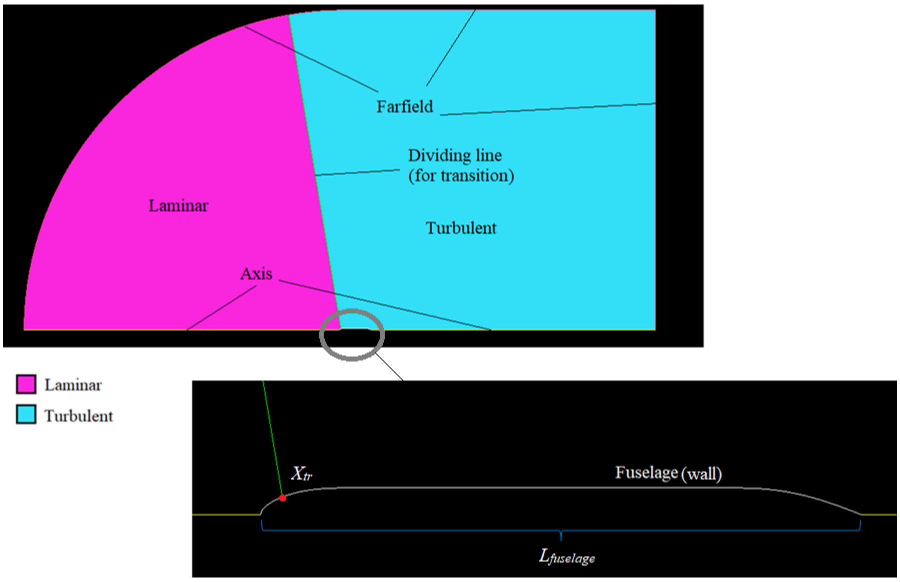

Figure 3.28: Flow domain and geometry details for fuselage simulation (RANS).

The plot showing different power balance and exergy analysis terms can be found in figure 3.29. The splitting of the mechanical energy outflow is given in figure 3.28. The values of Φ, $\dot{\varepsilon}$, and $\dot{\varepsilon}_{th}$ are not calculated from the flow field variables and are instead directly obtained from equations 2.11 or 2.26 as required. The reason for this is due to the ease of computing the terms and the reliability of the calculation. For example, Φ integral was found to be sensitive to minor meshing details in subsection 3.1.1. On the other hand, the expression to calculate $\dot{\varepsilon}_{th}$ (as given by equations 2.28 and2.29) behaves similar to the expression for net force F_x (given in equation 2.21). The error buildup associated with the F_x formula with the TP size has been discussed in subsection 3.1.1 (equation 3.27 gives some details). This makes the calculation of $\dot{\varepsilon}$ and $\dot{\varepsilon}_{th}$ unreliable as they are very sensitive to the CV definition. Fortunately, on the other hand, the anergy rate $\dot{A}$ as defined in equation 2.30 was actually observed to be well behaved and did not change much with TP size (in spite of some error build up being expected in this case based on previous arguments). In any case, the overall validity of the calculations is still verifiable. From figure 3.29, it can be noticed that the exergy rate $\dot{\varepsilon}$ closely matches the mechanical energy $\dot{E}$ rate once the thermal exergy $\dot{\varepsilon}_{th}$ rate tends to zero. This, of course, is a good verification of the results as the separate application of power balance and exergy analysis show consistency. It is also observed from the results that the anergy rate value is always higher than the dissipation. This means that the power balance method does not account for the thermal anergy rate $\dot{A}_{thm}$. The following equation gives some clarity:

$$\dot{E} - P_V = \dot{\varepsilon} + \dot{A}_{thm} - \dot{\varepsilon}_{\Phi} \,. \tag{3.42}$$

One argument can be given in which it can be proposed that if the curvatures of the fuselage body are not very high and an isentropic expansion or compression (meaning the process is reversible) can be assumed, then power balance method becomes more meaningful and represents only the mechanical power analysis. But due to the finite value of the thermal conductivity of the fluid, there is a deviation from this behavior. It should be noticed that the $\dot{E}$ terms is negative at the trailing edge as most of the energy is in the thermal form. $\dot{E}$ is not a good indicator of mechanical energy outflow when the thermal energy is finite. Ultimately the $\dot{E} - P_V$ value is a bit higher than the usable power at different locations. But it may still possible to use dissipation based analysis for qualitative studies for comparing fuselage geometries. However, it should be kept in mind that the obtained benefit from the power balance analysis may be higher than what is actually possible. Thus, the important power balance results from the Euler-IBLT solver can be supplemented with an exergy analysis.

3.4.3. Dissipation analysis of isolated body (Euler-IBLT)

Next, the baseline fuselage is analyzed using the Euler-IBLT flow solver. The transition is allowed to occur naturally based on the e^N method with $N_{crit} = 9$ and an X_{tr} of $0.0358 L_{fuselage}$ is obtained as mentioned earlier. An important aspect to note about this case is that the kinetic energy defect area $\frac{1}{2}\rho_e u_e^3 b\theta^*$ is higher than

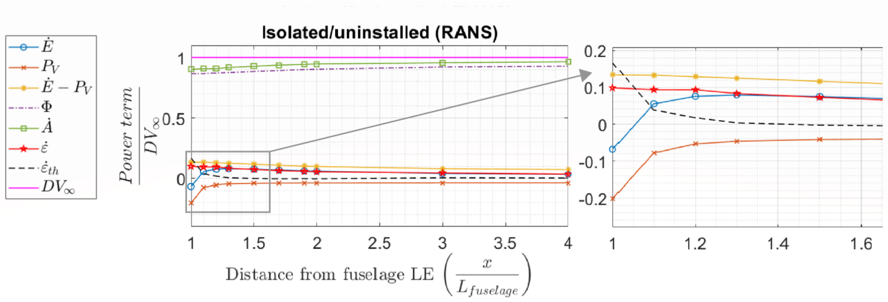

Figure 3.29: Power balance and exergy analysis for isolated baseline fuselage (RANS). $F_x = D$, and $M = 0.8$.

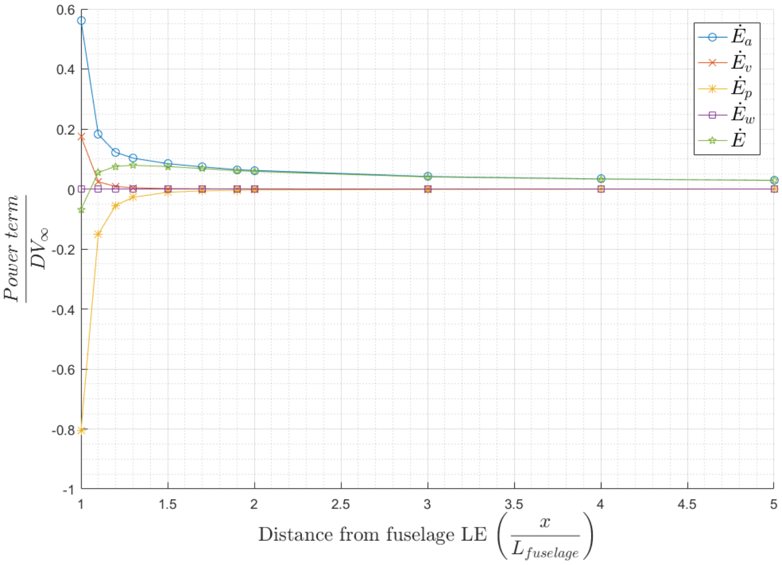

Figure 3.30: $\dot{E}$ composition from the flow field of baseline fuselage simulation (RANS). $F_x = D$, and $M = 0.8$.

the viscous dissipation at locations such as the fuselage TE. This is because the density flux thickness δ^{**} in the mechanical energy equation 2.51 is not negligible as in the incompressible case. This can be observed in figure 3.31.

It is now easy to observe the difference between energy defect area $\frac{1}{2}\rho_e u_e^3 b\theta^*$ and dissipation Φ. It is especially important to realize that the kinetic energy defect area initially reduces and then starts increasing. Thus, the viscous dissipation Φ obtained by integrating the dissipation term in equation 2.51 along the body (and wake when required) would be used as an indicator of the performance. Finally, the table containing the comparison of results from the RANS and Euler-IBLT are shown in table 3.11.

The RANS results in 3.11 are first verified against the drag prediction method described in the ESDU 78019 document [42]. The software provided with the ESDU 78019 [42] is used and the drag value is obtained for the selected fuselage geometry. Certain geometrical inputs required by the software with ESDU 78019 document [42] are calculated using the software from ESDU 77028 document [17]. It can be observed that the results from the RANS simulation are spot on with the results from the ESDU 78019 method.

As can be observed from the result, the body drag and isolated body surface dissipation seem a bit overpredicted by the Euler-IBLT solver. The surface anergy rate value from the RANS solver seems closer to the surface dissipation from the Euler-IBLT solver. But this can in no way be accepted as any special advantage as the Euler-IBLT solver is still limited for the theoretical point of view. Also, the difference in drag coefficient as expected is lesser when compared to the results from the NACA0040 BOR. Since the main goal is to study the difference in surface dissipation/anergy between different fuselage geometries, this difference is not expected

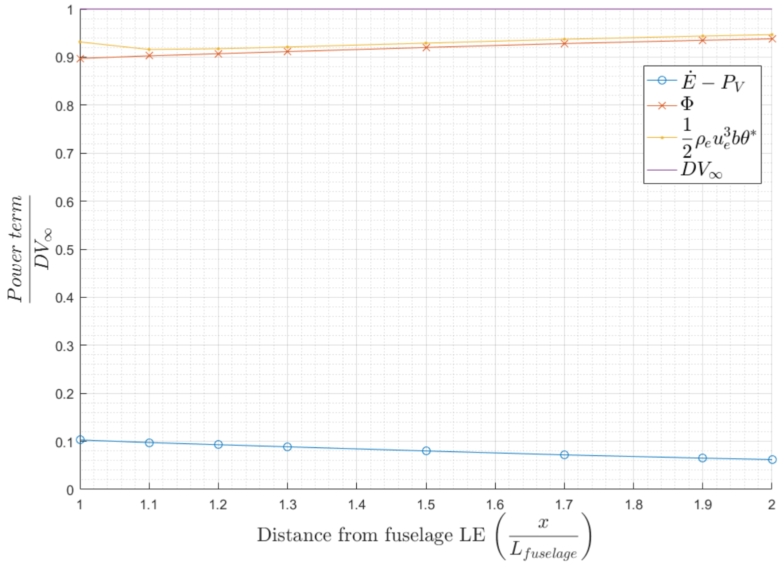

Figure 3.31: Dissipation analysis for baseline fuselage (Euler-IBLT). $F_x = D$, and $M = 0.8$.

Solver Quantity	ESDU 78019	RANS	Euler-IBLT	Difference (from RANS)
C_D	0.071715	0.071934	0.075096	0.31 % (ESDU 78019) -4.40 % (Euler-IBLT)
$\left(\frac{\dot{E}-P_V}{DV_\infty}\right)_{TE}$ (%)	-	13.36	10.30	3.06
$\left(\frac{\Phi}{DV_\infty}\right)_{TE}$ (%)	-	86.64	89.70	3.06
$\left(\frac{\dot{\varepsilon}}{DV_\infty}\right)_{TE}$ (%)	-	9.84	-	-
$\left(\frac{\dot{A}}{DV_\infty}\right)_{TE}$ (%)	-	90.16	-	-

Table 3.11: Comparison of results from RANS and Euler-IBLT solvers for baseline fuselage. $F_x = D$, and $M = 0.8$.

to cause much of a trouble. Thus, a dissipation analysis supported by anergy rate calculations for verifying important results should sufficiently result in a design space study.

4

DESIGN SPACE EXPLORATION STUDY

The studies from the previous chapters have led to a clear idea about the theoretical concepts of power balance and exergy analysis methods and their application to a CFD framework. Important details like the reliable terms (like terms which are free from error buildup) from the power balance and exergy analysis methods have been identified and their successful application to different configurations were verified. Also, the results from the RANS and Euler-IBLT solvers were compared to be able to maintain a critical perspective on the results from the solvers. Also, the drag result from the RANS solver was compared to the drag calculated using the ESDU 78019 document [42] software for the baseline fuselage case and the results had a negligible difference. The mesh and solver settings were also discussed. All these studies have lead to sufficient information gathering and confidence to proceed towards studying different fuselage geometries from the perspective of boundary layer ingestion.

Boundary layer ingestion is specifically chosen to be applied to the fuselage of aircraft since it is the longest part (in streamwise direction) resulting in a high amount of power being wasted in the wake flow (which should be clear from the power balance studies using flat plate). Also, due to its closely circular shape, it becomes easier to adapt aero-engines for boundary layer ingestion application when fuselage is used. The body of fuselage as such could be optimized for a minimum drag but due to the possibility of extracting some power in the wake, it becomes imperative to perform a dissipation or anergy based analysis at least from a theoretical perspective for now. Also, an important aspect to consider is the increase in drag that takes place due to the airframe and propulsor interaction. Isolated body studies followed by a study of propulsor interaction for different fuselage geometries and flight conditions would help understand the performance of different geometries when using BLI.

The exploration is considered for the following cases:

1. Isolated body:
    (a) Afterbody shape parameter ($paramsh$)
    (b) Afterbody slenderness $\left(\frac{L_{afterbody}}{D_{fuselage}}\right)$
    (c) Fuselage slenderness $\left(\frac{L_{fuselage}}{D_{fuselage}}\right)$
    (d) Flight speed (V_∞) (Variable M and Re)
    (e) Altitude (fixed M)
2. BLI configuration:
    (a) Afterbody shape parameter ($paramsh$)
    (b) Afterbody slenderness $\left(\frac{L_{afterbody}}{D_{fuselage}}\right)$
    (c) Fuselage slenderness $\left(\frac{L_{fuselage}}{D_{fuselage}}\right)$

(d) Flight speed (V_∞) (Variable M and Re)

(e) Altitude (fixed M)

(f) Propulsor radius ($R_{propulsor}$)

(g) Propulsor position

The exploration studies are first performed with the Euler-IBLT solver for several values of the specified parameters and further analyzed using RANS solver for specific values of each parameter depending on the requirement. Also, for all the analysis, all parameters are kept fixed (expect of course the parameter whose sensitivity is being studied) and same as the baseline case as defined in section 4.7. Also, the transition location obtained from the Euler-IBLT solver is used in RANS solver also to maintain consistency.

4.1. FUSELAGE AFTERBODY SHAPE

The afterbody of the fuselage is the airframe in the immediate vicinity of the considered BLI propulsor. Thus, the fuselage surface dissipation analysis (that is the viscous dissipation till fuselage TE which does not include wake viscous dissipation) for different afterbody shapes is an interesting study to perform.

As already described, the baseline fuselage geometry and flight condition are used and the results will be presented relative to this reference. Since dissipation information is possible to extract from the MTFLOW results, it is used as the performance parameter. Thus, it is easy to understand that lower the dissipation, better the geometry. Also the ideal power saving coefficient (PSC_{ideal}) as defined in section 2.2 (equation 2.8) would be presented as this value is interesting from the perspective of how beneficial a BLI configuration is in terms of power saving for a specific geometry or flight condition.

The parameterization of the fuselage geometry is done by dividing the fuselage geometry into forebody (based on ESDU I (or ESDU1) curve family as defined in the ESDU 77028 document [17]), a cylindrical midbody, and an afterbody (based on ESDU II (or ESDU2) curve family as defined in the ESDU 77028 document [17]). There are several shape families that have been defined in the ESDU 77028 document [17] for axisymmetric fuselage parameterization. These include shapes described by power law family, modified ellipsoid family, Myring cubic family, tangent ogive, and of course the ESDU I and ESDU II families. ESDU I is chosen for the aircraft forebody and ESDU II is chosen for the afterbody. The reason for this selection should be evident from the geometry obtainable by the shape families. The description by any one family mostly covers a wide range of shapes and roughly speaking the same shapes are to a large extant obtainable by the other families too leading to closely the same shapes by different families. The only exception is the power law family which mostly produced high drag and high dissipation shapes. Thus, any one family satisfactorily provided various shapes with only one control parameter. This unlike CST parameterization (provides better degree of freedom but requires more control parameters [43]) is very convenient for the design space study. The parameterization is clear from the figure 3.27 with the baseline fuselage geometry.

4.1.1. ANALYSIS USING EULER-IBLT SOLVER

The study is performed by fixing all parameters except the afterbody shape control parameter ($paramsh$). The transition prediction is still based on e^N method with $N = 9$. The dissipation analysis result for the isolated body cases are presented for the $paramsh$ values of $0, 0.2, 0.5, 1, 2, 4, 6, 8, 10, 20$, and 50 in figure 4.1.

It is possible to observe from figure 4.1 that the dissipation is lesser for higher values of $paramsh$ for the ESDU2 curve family. The corresponding afterbody shapes can also be observed in figure 4.1. The afterbody contributes to a higher surface dissipation when the curve is fully convex. The drag of the body also behaves similarly. This is because the power saving coefficient (ideal) as observed does not change much with afterbody shape (actually the change is so low that it is difficult to separate from numerical errors). This means that the ratio of the surface dissipation to the drag power is not changed much with the shape of the afterbody. This indeed may help in making the design of fuselages easier but there are still some questions to be answered.

An important complexity involved in the design of fuselages for BLI application is the fact that the propulsor modifies the flow field in its proximity changing certain important aerodynamic performance quantities.

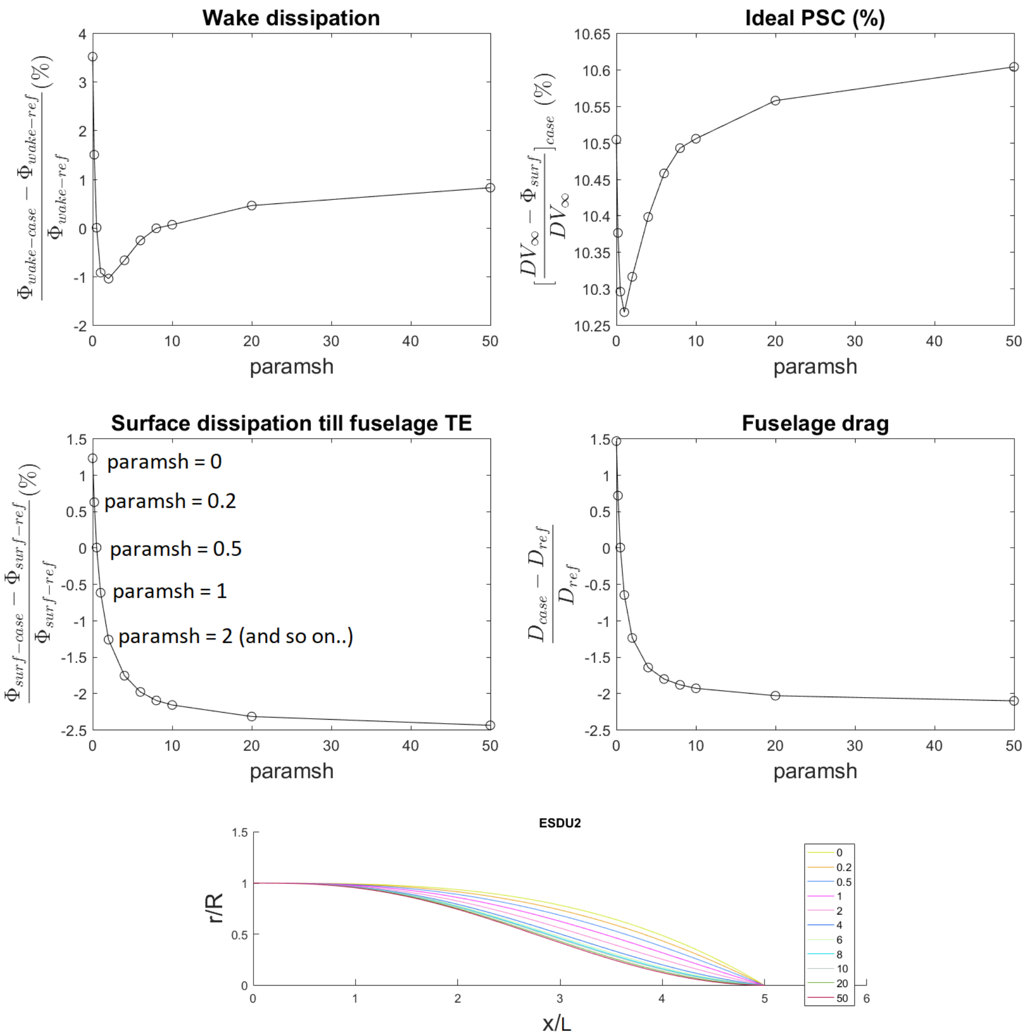

Figure 4.1: Design space exploration (Euler-IBLT) results for different afterbody shapes (isolated body). $F_x = D$, and $M = 0.8$.

As observed in the studies for flat plate with different wake filling propulsors in subsection 3.1.3, the drag value increases and the propulsor models show different power saving values depending on the interference (it should be noted that the perfect wake filler 2 has a higher interference than perfect wake filler 1 and approximate wake filler as the wake filling happens immediately behind plate). This clearly causes a higher surface dissipation in case of certain propulsors resulting in lower power saving coefficient values. The next question is if it would be possible to manipulate the shape of the body ahead of the propulsor to probably get a control over this interference? This question would be addressed with transonic flights in mind.

The interference caused by the presence of a propulsor was addressed in the literature by Hall et al. [6]. It is important to differentiate between the interference due to the propulsor body (like the nacelle) and the interference due to the static pressure jump created by the propulsor. The later is of interest as of now. The study by Hall et al. [6] shows that for different pressure ratios of the propulsor (placed behind the aerodynamic body), the change in surface dissipation is negligible. This study was performed by Hall et al. using MTFLOW. This is an interesting result which may have to be verified for different fuselage configurations and flight conditions.

To start with, the analysis as done for the isolated fuselage configuration using the Euler-IBLT solver (MTFLOW) is now repeated with a propulsor model and the power savings of the propulsor is found for the different afterbody shapes. But before proceeding further with the results, the propulsor modeling in the Euler-

IBLT solver needs discussion. Figure 2.5 as shown in subsection 2.5.2 clearly shows a possible propulsor grid at the aft of the fuselage. The propulsor size shown is rather large as it is as big as the fuselage in diameter. But the Euler-IBLT solver clearly seems to be limited with respect to the allowed propulsor size for BLI configurations. It is not possible to model a propulsor with a radius lesser than the displacement thickness (δ^*) as there will be no propulsion due to the absence of any flow field. But it does not end there. Propulsors smaller than the actual boundary layer thickness (δ) were found to give physically incorrect results (as can be noticed from figures 4.7). This is because the flow through such a propulsor model is not the same as flow through a similar model in a complete flow field as described and explained in A.2. Thus, to have a propulsor model with real flow physics, it needs to be at least as large as the boundary layer thickness. Thus, a propulsor with a radius equal to the fuselage radius is initially used (based on total pressure contour from RANS analysis in figure 4.5). The length of the propulsor is fixed to be $0.0145 \times L_{fuselage-Base}$ (which is $1.00m$) for all simulation cases as it gives a smooth convergence in the Euler-IBLT solver.

Next, proceeding to the power saving results for different afterbody shapes, the relevant plots are shown in figure 4.2. It is observed that the PSC_{strict} does not vary much for different afterbody shapes similar to the insensitivity of the PSC_{ideal} for the isolated body case. The variation of the propulsor power consumed has a variation similar to the variation of the isolated body surface dissipation. This again hints at the fact that the isolated body dissipation analysis can be used to study BLI configurations (at least for the comparison of different geometries) as suggested by Hall et al. [6].

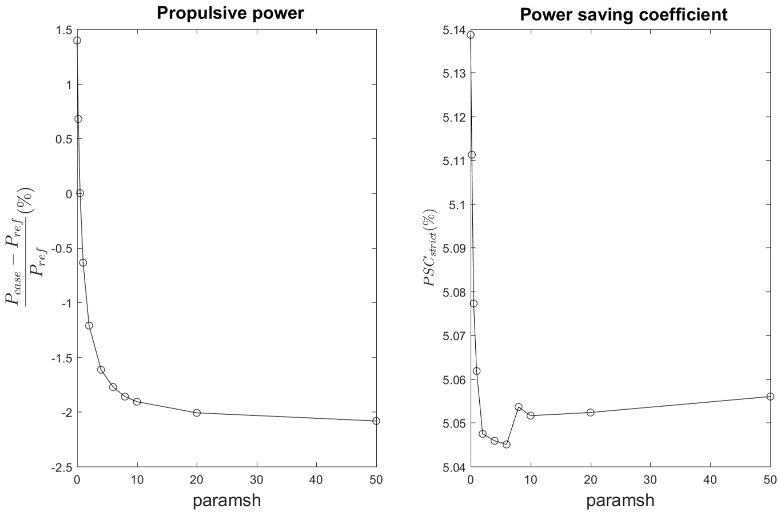

Figure 4.2: Design space exploration (Euler-IBLT) results for different afterbody shapes (BLI configuration). $F_x = 0$, and $M = 0.8$.

The change in surface dissipation (which is negligible as can be observed) by adding the propulsor is shown in figure 4.3. The change in shape factor at the fuselage TE is shown in figure 4.4. The relation between the shape factor and the dissipation coefficient as given in the work by Hall et al. [6] is included in the appendix section A.3. It should be noted that the change in the dissipation coefficient is of the same nature as the shape factor for turbulent flow at high shape factors (which is the case near the fuselage TE). Thus, on one hand the propulsor tries to decrease the surface dissipation by decreasing the shape factor but at the same time the pressure gradient created by it causes an increase in the boundary layer edge velocity which should increase the surface dissipation as explained in A.3. This causes the dissipation to remain unchanged when a propulsor is added which causes a minor change in shape factor of the nearby flow. But it should be noted that the friction coefficient behaves differently (edge velocity increases or decreases along with friction coefficient). The increase in drag (at least friction drag) is explained. Also, as observed in case of the flat plate, the addition of propulsor causes an increase in $\dot{E}$ at the plate TE as compared to the isolated case. There is clearly a rearrangement of the usable power due to the addition of propulsor. Thus, the increase in fuselage drag (the integrated pressure and viscous forces) can be attributed to this. This qualitative explanation is rather just to give simple theoretical support to the result.

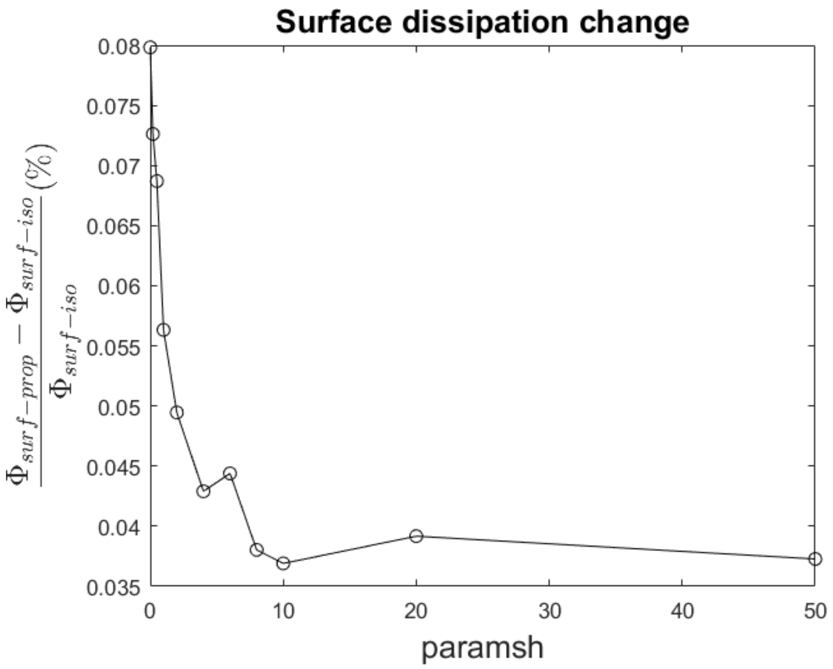

Figure 4.3: Surface dissipation change due to propulsor for different fuselage afterbody shapes (Euler-IBLT). $M = 0.8$.

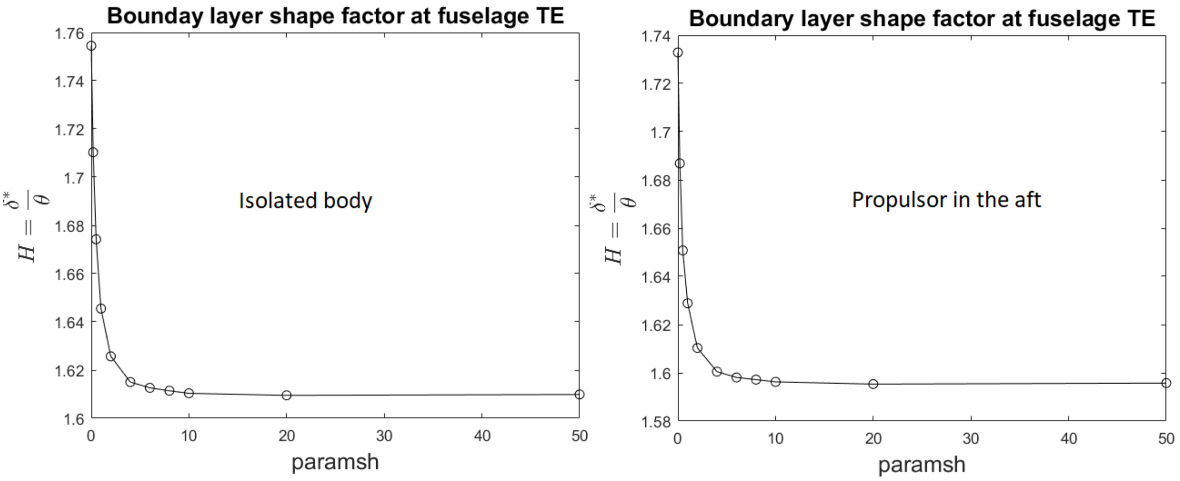

Figure 4.4: Change in shape factor at the fuselage TE due to propulsor for different fuselage afterbody shapes (Euler-IBLT). $M = 0.8$.

But the analysis does not end here as the results presented by Hall et al. [6] using MTFLOW still requires clarification regarding the propulsor size used. Also, it would be interesting to study the surface anergy rate instead of the dissipation to more accurately capture the physical aspects of the flow.

4.1.2. ANALYSIS USING RANS SOLVER

Due to the requirement of high computational time for RANS analysis, only certain important cases from the design exploration study will be analyzed using the RANS solver. In the present case, the result for the RANS analysis for the isolated baseline fuselage is already known and it will be interesting to study the same result for the least dissipation fuselage obtained in the Euler-IBLT analysis (which is for an afterbody *paramsh* of 50). Another important verification would be to study the effect of adding a propulsor in the RANS framework.

First, the isolated body analysis results for the baseline fuselage and for the obtained low dissipation fuse-

Quantity	$paramsh = 0.5$	$paramsh = 50$	Difference
C_D	0.071934	0.070223	-2.38 %
$C_{\Phi S}$	0.031160	0.030520	-2.05 %
$C_{\dot{A}S}$	0.032427	0.031569	-2.64 %
$\left(\frac{\dot{E}-P_V}{DV_\infty}\right)_{TE}$ (%)	13.36	13.08	-0.3
$\left(\frac{\Phi}{DV_\infty}\right)_{TE}$ (%)	86.64	86.92	0.3
$\left(\frac{\dot{\varepsilon}}{DV_\infty}\right)_{TE}$ (%)	9.84	10.09	0.3
$\left(\frac{\dot{A}}{DV_\infty}\right)_{TE}$ (%)	90.16	89.91	-0.3

Table 4.1: Isolated body results for two afterbody shapes (RANS). $F_x = D$, and $M = 0.8$.

lage are presented in table 4.1. It can be observed from the results that the surface anergy rate difference in RANS result is close to the dissipation difference as obtained in the Euler-IBLT solver (clearer if observed from bar charts in section 4.8). Also, the maximum extractable power (the exergy at fuselage TE which is indicative of exergy based PSC_{ideal}) as a percentage of drag power does not change much for the two fuselage geometries. Of course, this behavior is comparable to the ideal power saving coefficient behavior as obtained using the Euler-IBLT solver. But it is only fair to compare the dissipation based values to the Euler-IBLT solver anyways. The values of dissipation Φ also does not vary much between the two fuselage geometries (which again hints at close dissipation based PSC_{ideal} values).

Next, the addition of propulsor is required to study actual BLI configurations. Also to justify the propulsor size used in the Euler-IBLT study the total pressure contours are analyzed from the RANS solution. Since the validity of the results is dependent on the size of the propulsor with respect to the local boundary layer thickness (in Euler-IBLT solver), a contour of total pressure can help decide a safe propulsor size at least for the preliminary study. These total pressure contours are shown for the two afterbody shapes in figure 4.5. As can be observed since the total pressure almost recovers to the freestream value before the fuselage radius, the radius of the fuselage could be a safe choice for the propulsor radius.

Next, having decided upon the initial propulsor sizing for the study, it becomes imperative to define a propulsor modeling in the RANS solver. Unlike the previously analyzed cases of incompressible flow over a flat plate, the flow physics has changed to compressible and this directly impacts the propulsor model. The addition of momentum sources as done previously in the case of approximate wake filler (in subsection 3.1.2) cannot result in power addition. This is because the momentum source only enters the momentum equation of the solver [25]. A separate source needs to be defined for energy. Adding only momentum source just uses up the internal energy of the flow resulting in no net addition of power. As such a body force model (like adding a momentum source) to represent a propulsor is described in works like [44, 45]. Especially in the work by Stokkermans [45], an actuator disc model is considered for a compressible flow application in which momentum and energy sources are simultaneously defined to simulate a propeller and experimental evidence is presented and compared with RANS CFD simulations (using Spalart-Allmaras turbulence modeling). This type of modeling is found to be useful due to its cheap computational cost as compared to modeling a complete three-dimensional propeller. Also, the intention of the present thesis is not to give advice for designing a propulsor for the novel configuration.

The momentum and energy sources are added to produce a uniform pressure jump (not a complete wake filling attempt as done in case of flat plate). The energy sources required to produce a given momentum addition is calculated on the basis local velocity field as done in [45]. That is if a momentum source is added to a cell to produce an axial thrust force of F_c, then the power required is calculated as $F_c.u_c$, where u_c is the fluid velocity in the cell. This, of course, means that the cell must be sufficiently small in the axial direction. The fuselage is shown with a propulsor in the figure 4.6. The integrated pressure and viscous force over the fuselage body is equated to the force due to the added momentum sources ($D_{fuselage} = T_{propulsor}$). The user-defined function for the same can be found in appendix C.2. It is easy to observe that the model is cor-

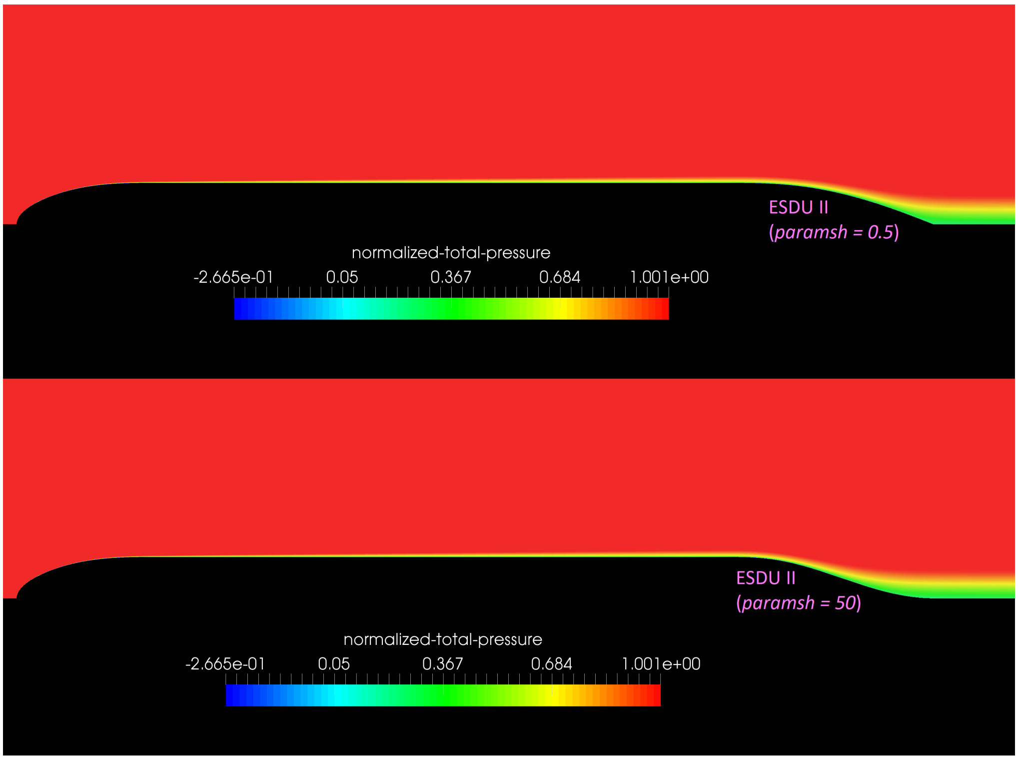

Figure 4.5: Normalized total pressure (p_0/p_{0_∞}) contour for two different afterbody shapes. This gives an indication of the boundary layer thickness. $F_x = D$, $M = 0.8$.

rect by calculating the net force (F_x) at some test plane after the propulsor (defined in section 2.3). It should be noted that F_x is not a reliable integral (as described in subsection 3.1.1) and the size of the test plane must be carefully cut off once the total pressure recovery is achieved. Even after all the precautions, only the order of magnitude of the net force (F_x) obtained through the integration is important and can be used for a superficial verification. Finally, another important detail to note is that no wall of any kind is added to the edge of the propulsor to prevent mass flow from the top. The main reason for this is that adding any such body (with or without friction) will cause an interference with the fuselage which can hinder the study of the actual BLI effect.

With these details, it is possible to proceed with the results of the two afterbody shapes with propulsors. Since in RANS it is possible to model a propulsor size of choice, two different propulsor sizes are chosen. One with diameter equal to the fuselage diameter ($1 \times D_{fuselage}$ called r100) and the other with diameter half of the fuselage diameter ($0.5 \times D_{fuselage}$ called r50). It should be noted that to maintain the cruise condition, a smaller propulsor would have to produce a higher pressure jump (and hence utilizing more power from the boundary layer in this case). The surface anergy rate of the fuselage is again of interest to understand the interaction effect of propulsor for different afterbody geometries. The table 4.2 gives different quantities of interest for the two afterbody shapes with propulsors of two different diameters. As can be observed the fuselage drag coefficient (C_D) obtained as the integrated pressure and viscous forces is quite misleading for power considerations. The propulsor power values from a qualitative sense still follow the isolated body dissipation (or drag for that matter) behavior, that is the afterbody with $paramsh = 0.5$ requires more power than the $paramsh = 50$ body for cruise flight. Also, the surface anergy rate ($C_{\dot{A}S}$) is not changed much to be separable from numerical errors when different propulsors are added. Thus, all the present evidence assert the fact that the isolated body analysis quite elegantly captures the qualitative power requirements of different fuselage geometries.

Finally, it is also mentioned that the Euler-IBLT solver seems to over predict the value of the power saving coefficient ($\approx 5.1\%$) as compared to the RANS solver (which give PSC_{strict} of $\approx 2.5\%$). This can be observed in the figure 4.2 and the table 4.2. This can be an effect of the difference in the flow models between the Euler-

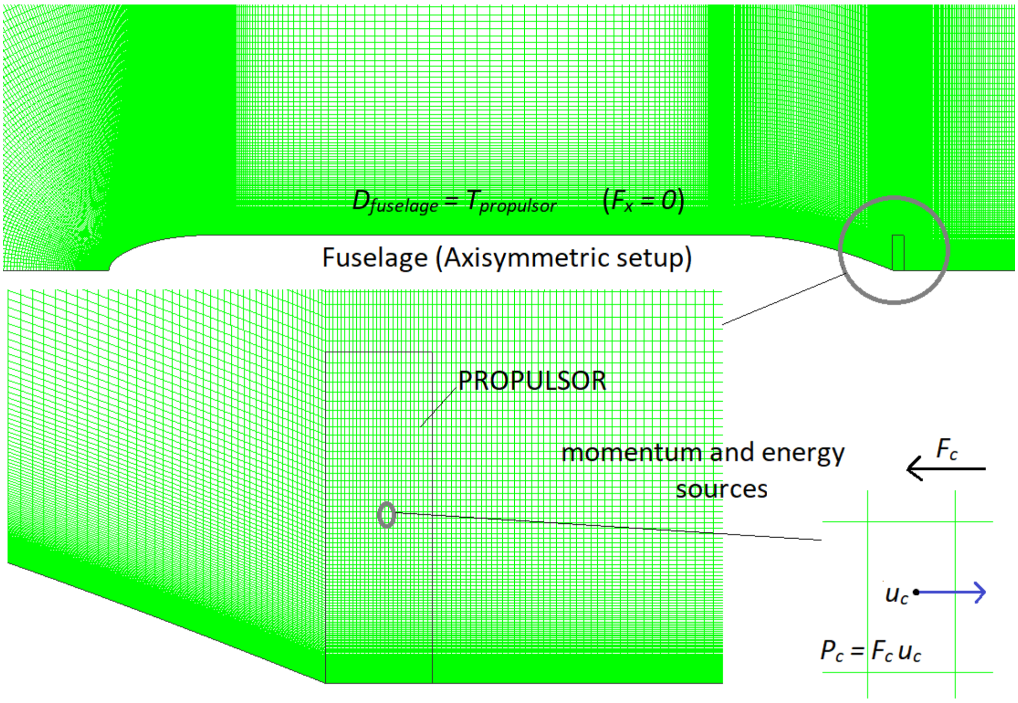

Figure 4.6: Example flow domain with propulsor model in RANS solver.

IBLT and the RANS solvers. But this is anyways less of a concern as the relative power consumption (whose match is good between the solvers) is a more important performance metric when comparing different fuselage designs.

Quantity	$paramsh = 0.5$	$paramsh = 50$	Difference
$\frac{D_{propulsor}}{D_{fuselage}} = 1$			
C_D	0.079498	0.073697	-7.30 %
C_P	0.035034	0.034232	-2.29 %
$C_{\dot{A}S}$	0.032404	0.031614	-2.44 %
$PSC_{strict}(\%)$	2.59	2.51	-0.08
$\left(\frac{\dot{A}_{prop}-\dot{A}_{iso}}{\dot{A}_{iso}}\right)_{TE}(\%)$	-0.0703	0.142	NA
$\frac{D_{propulsor}}{D_{fuselage}} = 0.5$			
C_D	0.08371	0.074758	-10.69 %
C_P	0.033436	0.032620	-2.44 %
$C_{\dot{A}S}$	0.032466	0.031674	-2.44 %
$PSC_{strict}(\%)$	7.04	7.10	0.06
$\left(\frac{\dot{A}_{prop}-\dot{A}_{iso}}{\dot{A}_{iso}}\right)_{TE}(\%)$	0.12	0.33	NA

Table 4.2: BLI configuration results for two afterbody shapes (RANS). $F_x = 0$, and $M = 0.8$.

4.2. PROPULSOR RADIUS

The radius of the propulsor plays an important role in the pressure gradient created. This is assumed to cause a change in the propulsor-airframe interference. This can also be observed form the integrated pressure and friction forces on the fuselage body with propulsors of different sizes placed at the aft (C_D values in table 4.2).

Although some evidence regarding the effect on power consumption have already been presented for different fuselage geometries, a formal analysis of the dependence on the propulsor radius would be very interesting. Mainly because the Euler-IBLT solver does not function correctly at smaller radii, a deeper analysis using RANS solver becomes necessary.

4.2.1. ANALYSIS USING EULER-IBLT SOLVER

First, the results using the Euler-IBLT solver would be presented. For this, the propulsor radius is kept above the displacement thickness value (only then the results can be obtained). It is again mentioned that there exists no flow field below the displacement thickness and the propulsor becomes useless below that size. Then a question arises regarding how a propulsor model operates on the boundary layer in the Euler-IBLT solver? Theoretically speaking, it could be argued that once the propulsor is larger than the displacement thickness, it changes the pressure field in the inviscid part changing values like the edge velocity and edge pressure. Any change to the edge pressure is transmitted across the boundary layer by assumptions in Prandtl's boundary layer equations (as mentioned in section 2.5.2). But the requirement as described in appendix A.2 is that the propulsor must be at least as large as the boundary layer thickness. Thus, the incorrect results for propulsor size below boundary layer thickness value would also be shown to highlight the extent of validity of the Euler-IBLT solver.

The results are shown for different values of propulsor radius in figure 4.7. The ratio of propulsor to the fuselage radius tried are 0.55, 0.65, 0.75, 0.85, 1, 1.25, 1.5, 1.75, and 2.

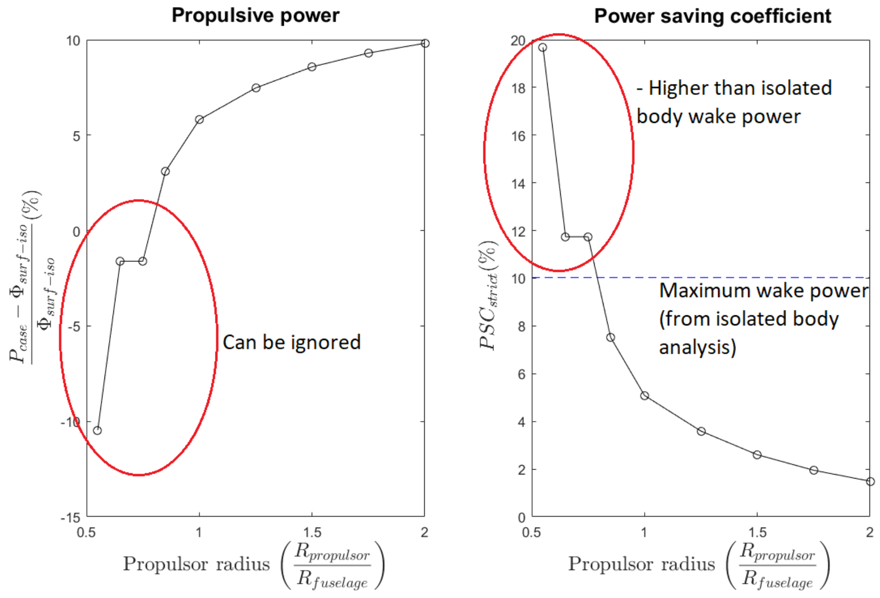

Figure 4.7: Design space exploration (Euler-IBLT) results for baseline fuselage geometry with propulsors of different radius. Maximum wake power in the isolated body flow is marked as dashed line. $F_x = 0$, and $M = 0.8$.

It can be observed from the results that for propulsor to fuselage radius ratios of lesser than 0.85, the results are absurd. One fact is that the power saved by adding the propulsor is more than the power available in the wake of the isolated body flow. Further, the shape factor at the fuselage trailing edge is given in figure 4.8 and the change in surface dissipation (when compared to baseline isolated fuselage value) is given in figure 4.9. The shape factor at fuselage TE changes little when compared to baseline fuselage isolated simulation value of 1.6742. The change in dissipation as observed again is negligible.

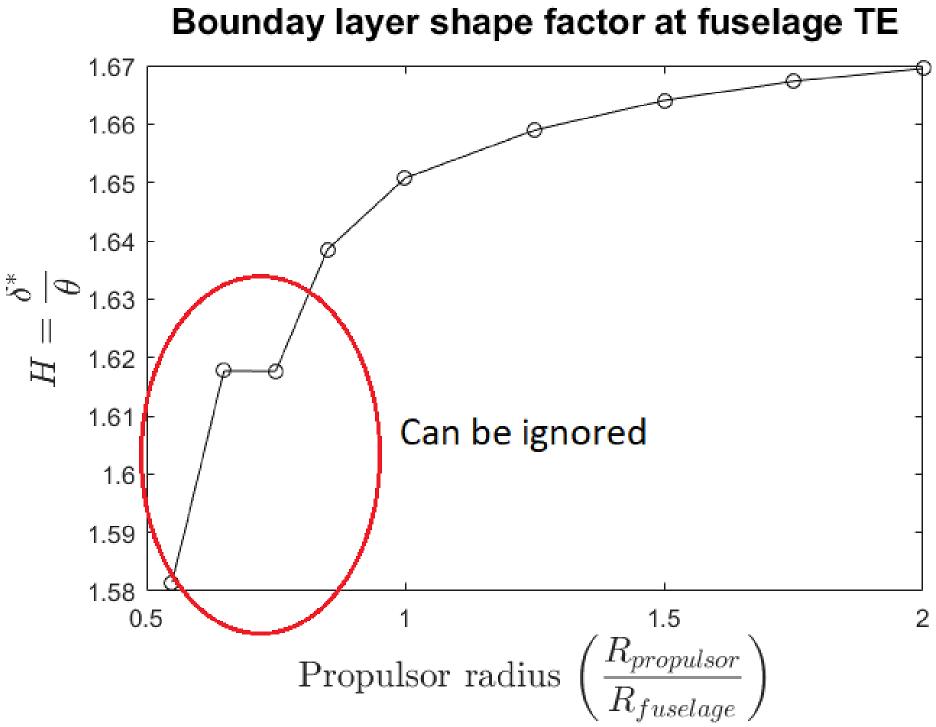

Figure 4.8: Shape factor at the fuselage TE for different propulsor radius (Euler-IBLT). $F_x = 0$, and $M = 0.8$.

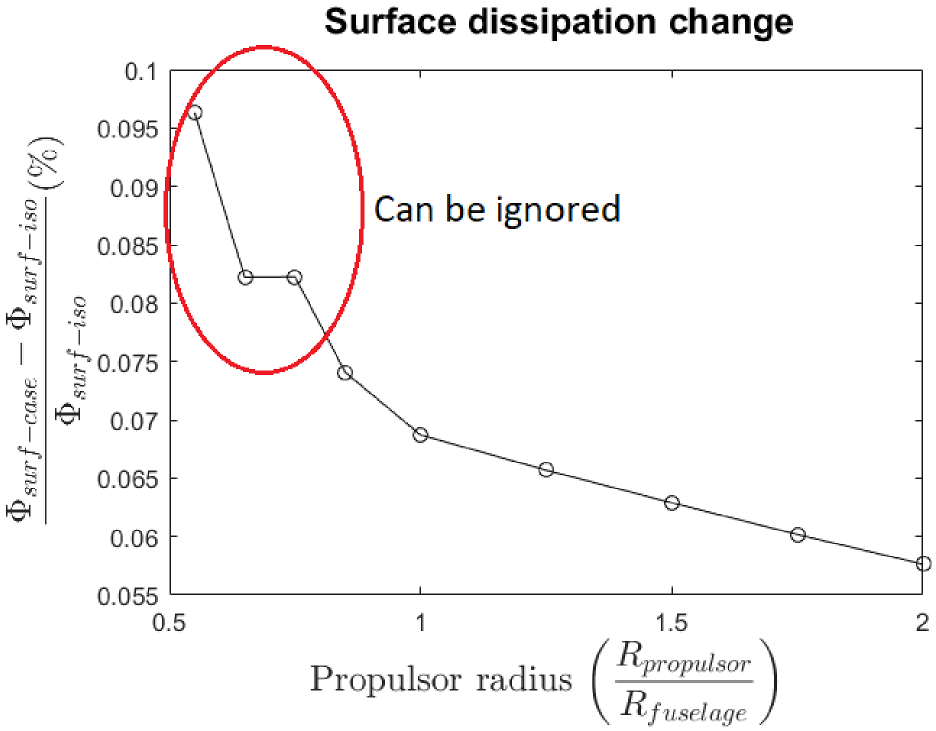

Figure 4.9: Surface dissipation change due to propulsor for different propulsor radius (Euler-IBLT). $M = 0.8$.

The results observed from the Euler-IBLT solver for these cases must be analyzed with caution and it becomes important to analyze the lower propulsor radii using a RANS solver. This constitutes the next subsection.

4.2.2. ANALYSIS USING RANS SOLVER

It should be clear from the previous section that a RANS analysis is imperative for understanding the complete effect of propulsor radius. The propulsor as shown in the example domain in figure 4.6 is divided into smaller propulsors as required and the simulations are performed. As already mentioned, the integrated pressure and friction forces on the fuselage body are equated to the force added through momentum source in the propulsor. The energy (actually power) sources corresponding to the momentum sources are added as mentioned before in subsection 4.1.2. The added momentum source is uniform in the propulsor volume as before for all cases.

The effect of pressure ratio as covered in the work of Hall et al. [6] is mostly similar (in effect) in a way to changing the propulsor radius. But using a RANS analysis to measure the change in surface anergy rate is more appropriate and useful. Apart from this, Gray et al. [13] present a sensitivity result of force benefit (for a fixed power) with respect to fan pressure ratio in a RANS based framework. A separate 1-D solver is used for propulsor analysis and such a framework is suggested for future studies.

First, the result for the power saving coefficient (strict) is given in figure 4.10. It can be observed that the power saving coefficient is maximum for a propulsor radius close to $0.5 \times R_{fuselage}$ (r50 case). The power saving reduces on either side of this propulsor radius. This can be easily explained. Since the momentum source is uniform in the propulsor volume, lesser of the boundary layer is filled with increasing propulsor size (this is especially true once the propulsor is larger than the boundary layer thickness). On the other hand, propulsors smaller than the boundary layer ingest lesser boundary layer but achieve more filling due to higher pressure gradient required to achieve cruise. After a particular size, the reduced propulsor size results in more loss in the propulsor jet as the flow velocity there becomes faster than freestream. In extreme cases like for the propulsor with the lowest considered radius, the jet flow is supersonic and this results in a heavy penalty as can be observed in figure 4.10. The jet flow (Mach contour) for this propulsor is shown in figure 4.11.

It should be noted that there is no issue with PSC_{strict} being negative. It just means that the non-ideal BLI propulsor consumes more power than the ideal non-BLI propulsor. It is possible to check the actual power saving coefficient (PSC_{actual} as defined in section 2.2) for such propulsors. This can be done by using the same size propulsor model without the fuselage to allow freestream operation. The thrust can be specified as that for the isolated fuselage (=drag for cruise) and results could be obtained. This is done for the $r100$ and $r12.5$ propulsors and the PSC_{actual} values are also provided in figure 4.10. The $r100$ propulsor operating in freestream (non-BLI) already performs well due to large radius. This is because, the larger the propulsor radius, the higher will be the propulsive efficiency (defined in section 2.2) due to reduced exit jet velocity at fixed thrust. Also much boundary layer filling is not achieved by the $r100$ BLI propulsor due to the large radius. The combination of these factors ultimately result in PSC_{actual} of the $r100$ BLI propulsor being lower than that of the $r12.5$ BLI propulsor.

Next, moving on to the surface anergy rate change and the fuselage drag change due to the addition of the propulsor, the plots can be found in figure 4.12. It can be clearly observed that the change in surface anergy rate is negligible for all propulsor radii and the statement about the possibility of using an isolated body analysis to evaluate the fuselage aerodynamic performance even for BLI configurations is strengthened. Further, the fuselage drag (integrated pressure and viscous forces) shows similar behavior as the power saving but the peak is found to be for a lower propulsor radius ($R_{propulsor} = 0.25 \times R_{fuselage}$). The drag change is just presented to show how misleading it can be to use forces for evaluating performance in a BLI configuration.

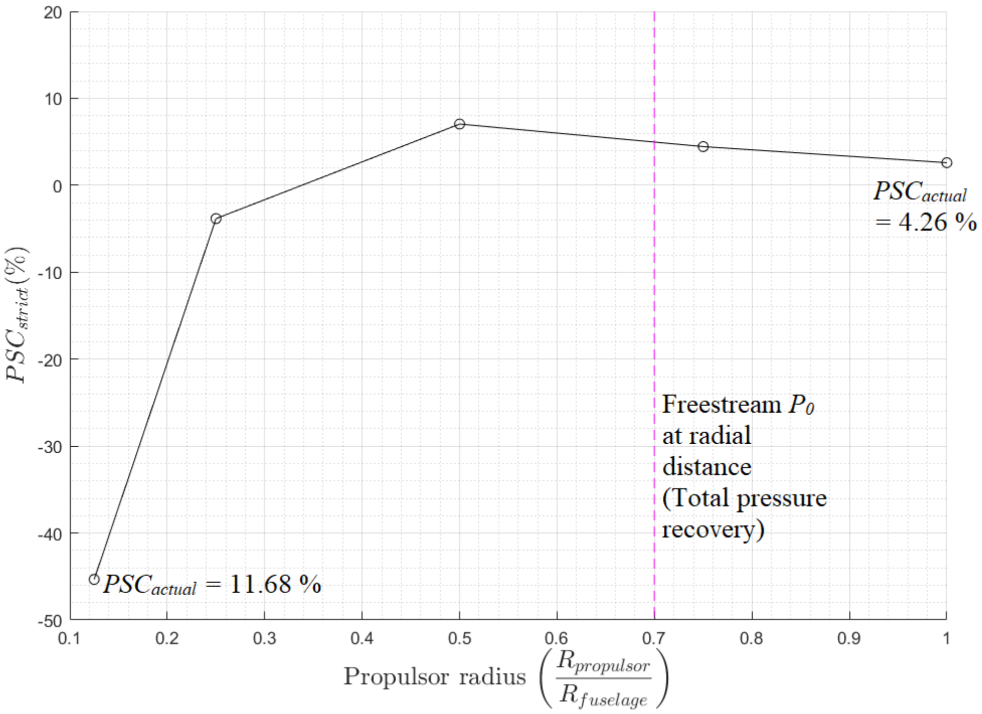

Figure 4.10: Design space exploration (RANS) results for different propulsor radius. The PSC_{actual} values are calculated using propulsors of the same respective sizes for both BLI and freestream ingestion. $F_x = 0$, and $M = 0.8$.

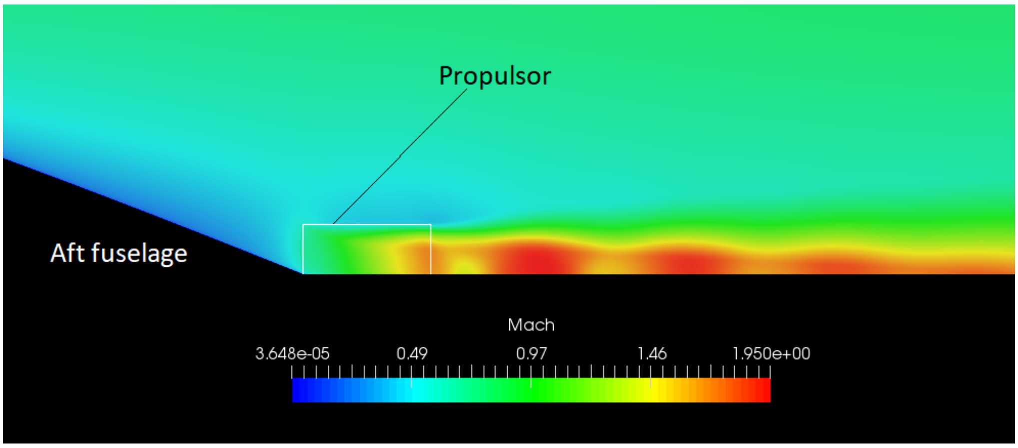

Figure 4.11: Supersonic jet at the aft of the small propulsor ($R_{propulsor}/R_{fuselage} = 0.125$) (RANS). $F_x = 0$, and $M = 0.8$.

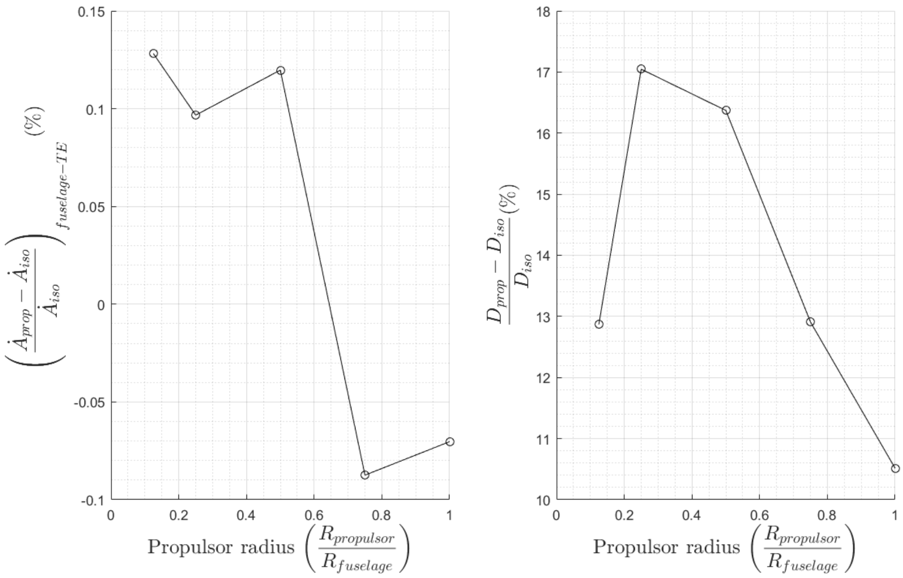

Figure 4.12: Change in fuselage surface anergy rate and drag due to the addition of propulsors of different radius (RANS). $M = 0.8$.

4.3. FUSELAGE AFTERBODY SLENDERNESS

It is a known fact that the aerodynamic drag of a fuselage depends on the wetted area and changing the fuselage slenderness has a direct impact on the wetted area. Increasing the slenderness of a body for a fixed length would result in the decrease of the wetted area and a corresponding decrease in drag. This variation of drag with afterbody slenderness can be observed clearly in [42]. The requirement of power is, of course, lower for fuselages with lesser drag if a freestream ingesting propulsor is used. The dependence of surface dissipation and anergy rate are left to be verified when a propulsor is added to the aft of the fuselages. Also, the variation of the maximum power saving coefficient with the fuselage shape could be verified. These are the goals of the present section.

4.3.1. ANALYSIS USING EULER-IBLT SOLVER

To start with, the Euler-IBLT solver would be used for the analysis. The length of the fuselage is fixed and the afterbody slenderness is varied. The shape of the afterbody is defined by the same shape (that is the baseline shape of ESDU II class with $paramsh = 0.5$) for all afterbody slenderness values.

The slenderness values for the fuselage afterbody can be considered based on the values provided in [46] for different aircraft classes. The table from [46] is repeated in appendix B.1 for quick reference. The various values of afterbody slenderness used are $2, 2.5, 3, 3.5, 4, 4.5, 5, 5.5$, and 6. The variation in afterbody slenderness is expected to cause some noticeable change in shape factor due to the change in pressure gradient. Thus, this effect on the boundary layer is worth investigating. The main result of the study is presented in figure 4.13.

The surface dissipation is observed to behave like the isolated body drag as before. The reduction in dissipation is much larger for changing afterbody slenderness when compared to changing afterbody shape. The power saving coefficient (PSC_{ideal}) can be observed to approximately reduce by 2% as the afterbody slenderness is increased. This hints at the fact that less slender bodies give lesser benefit. But this is not observed in the result from RANS as will be discussed later and the PSC_{ideal} result must be viewed with caution.

Next, the effect of the propulsor can be studied. For the same values of the afterbody slenderness, the results with the propulsor (in the aft) are presented in figure 4.14. The power consumption plot matches with the dissipation variation. The percentages match well as can be noticed. The power saving coefficient (strict) does not change much ($< 1\%$) for different afterbody slenderness values which is a bit different from the PSC_{ideal} trend from the isolated body simulations (but this is, of course, possible).

Finally, the shape factor change at the fuselage TE due the propulsor addition is provided in the figure 4.16 and the surface dissipation change caused by the presence of propulsor is shown in figure 4.15. The surface dissipation is still not affected by the presence of the propulsor and the shape factor values can be used to give an explanation as done previously (for the different afterbody shapes).

4.3.2. ANALYSIS USING RANS SOLVER

Again it becomes imperative to verify at least some results from the Euler-IBLT solver using a RANS analysis. To perform this, the upper bound value of the afterbody slenderness of 6 which was tested in the Euler-IBLT solver is chosen. Isolated body simulation results for this chosen fuselage and baseline fuselage are provided in table 4.3. It can be observed that the variation in the value of fuselage surface dissipation and surface anergy are close to the variation in the surface dissipation value from the Euler-IBLT solver as can be observed from figure 4.13 and table 4.3. The PSC values (ideal and strict) can be conveniently noted from the chart in figure 4.34 (result summary). A possible explanation for the differences is also provided in that section (section 4.8).

Next, the results for the fuselage with a propulsor at the aft are provided for the baseline fuselage (afterbody slenderness of 2.5) and for the fuselage with afterbody slenderness of 6. These can be found in table 4.4. The obtained results again demonstrate the insensitivity of the surface anergy to the addition of propulsor. The value of the difference in the power consumed (can be obtained from power coefficient C_P) has a close match with the result from the Euler-IBLT solver (figure 4.14). The power saving coefficient (PSC_{strict}) as such can be observed to show very little change for different fuselage afterbody slenderness. Finally, the inte-

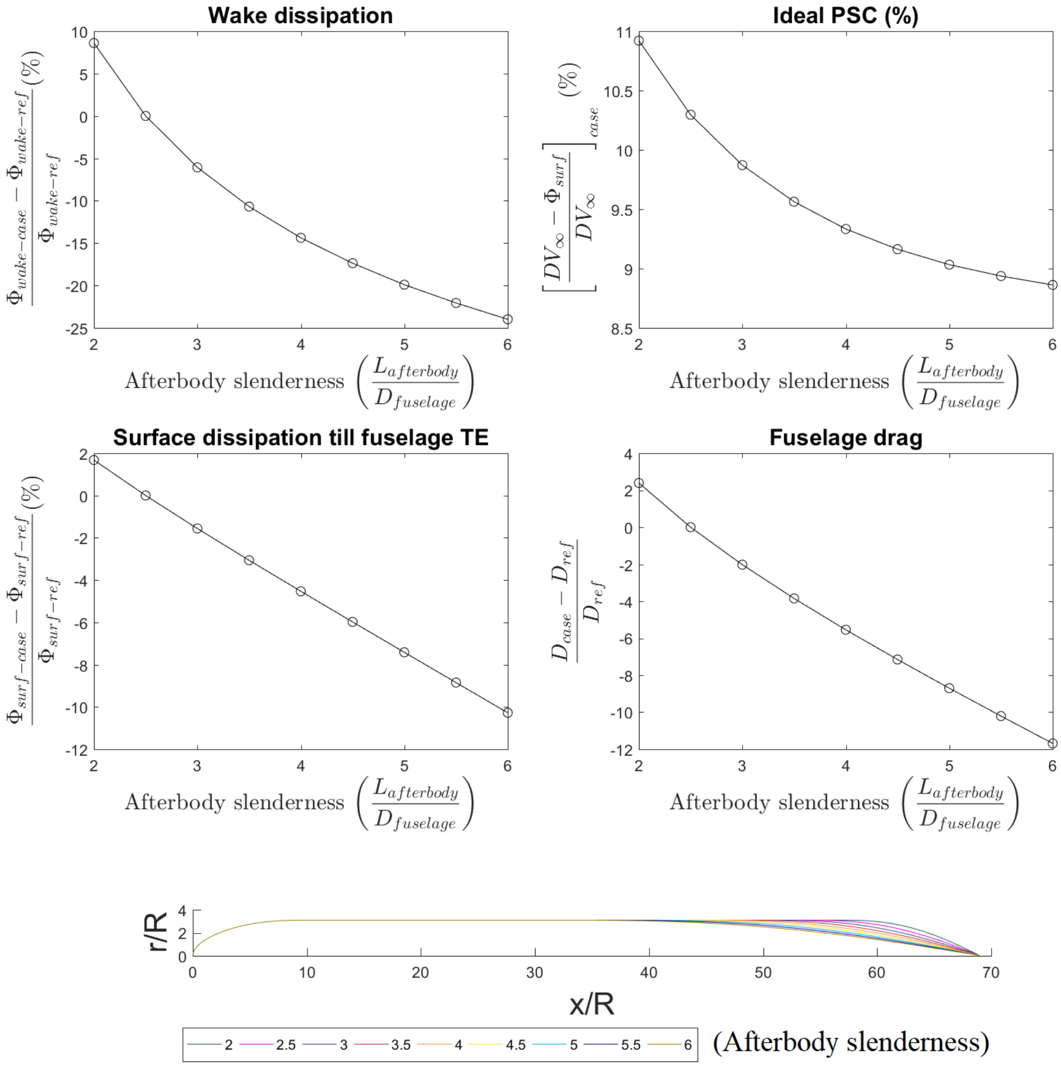

Figure 4.13: Design space exploration (Euler-IBLT) results for different afterbody slenderness for a fixed fuselage length (isolated body). $F_x = D$, and $M = 0.8$.

Quantity	$\frac{L_{afterbody}}{D_{fuselage}} = 2.5$	$\frac{L_{afterbody}}{D_{fuselage}} = 6$	Difference
C_D	0.071934	0.063089	-12.30 %
$C_{\Phi S}$	0.031160	0.027518	-11.69 %
$C_{\dot{A}S}$	0.032427	0.028538	-11.99 %
$\left(\frac{\dot{E}-P_V}{DV_\infty}\right)_{TE}$ (%)	13.36	12.77	-0.6
$\left(\frac{\Phi}{DV_\infty}\right)_{TE}$ (%)	86.64	87.23	0.6
$\left(\frac{\dot{\varepsilon}}{DV_\infty}\right)_{TE}$ (%)	9.84	9.53	-0.3
$\left(\frac{\dot{A}}{DV_\infty}\right)_{TE}$ (%)	90.16	90.47	0.3

Table 4.3: Isolated body results for two fuselage afterbody slenderness values (RANS). $F_x = D$, and $M = 0.8$.

grated pressure and friction forces on the fuselage (drag) show the opposite trend when compared to power consumption for different propulsor sizes used in the same fuselage. This is a bit non-intuitive and such force

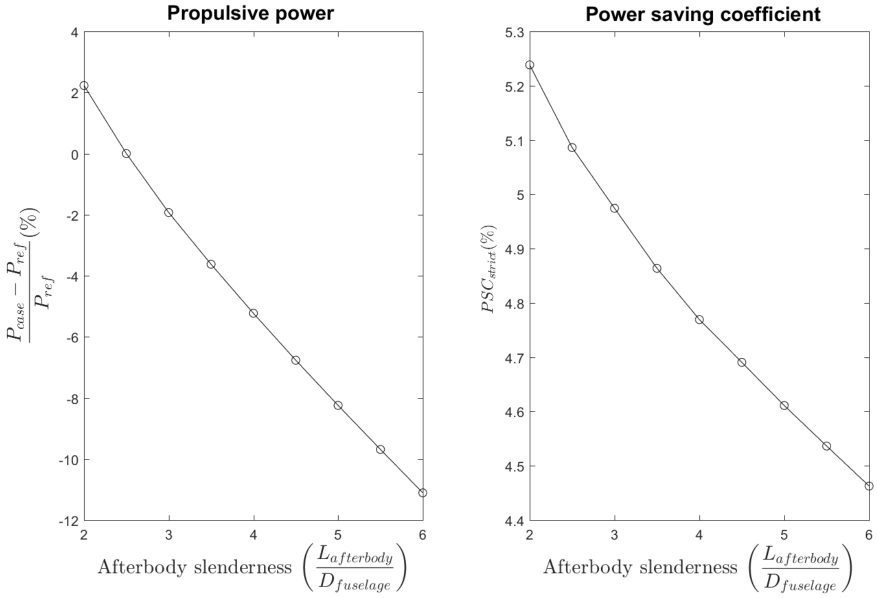

Figure 4.14: Design space exploration (Euler-IBLT) results for different afterbody slenderness for a fixed fuselage length (BLI configuration). $F_x = 0$, and $M = 0.8$.

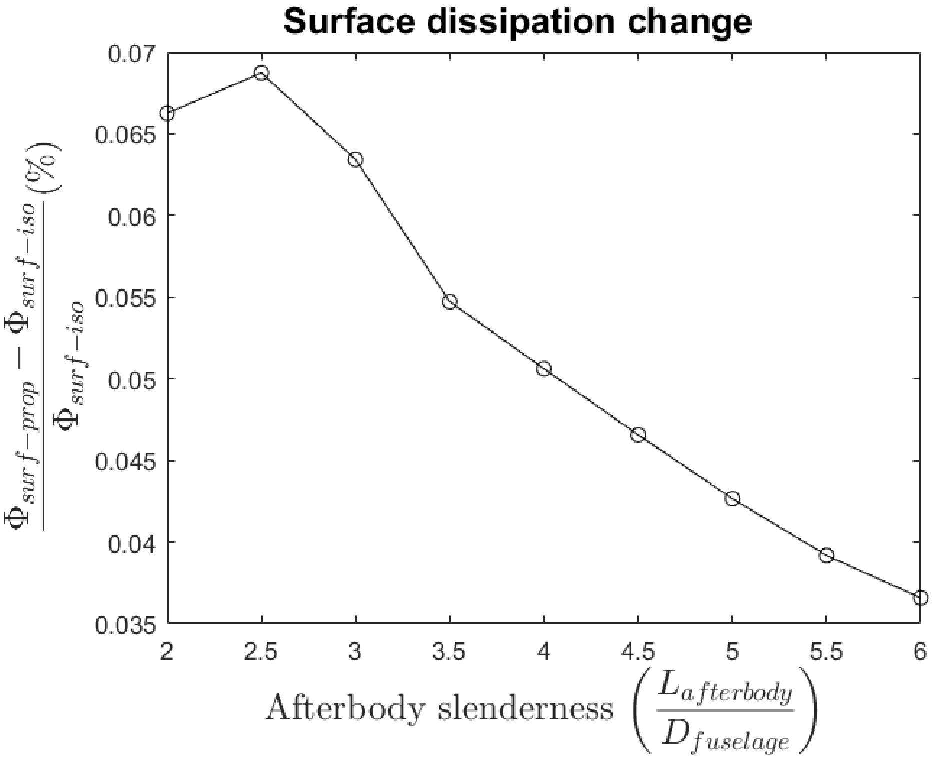

Figure 4.15: Surface dissipation change due to propulsor for different fuselage afterbody slenderness (Euler-IBLT). $M = 0.8$.

values must be avoided while analyzing performance of BLI configurations.

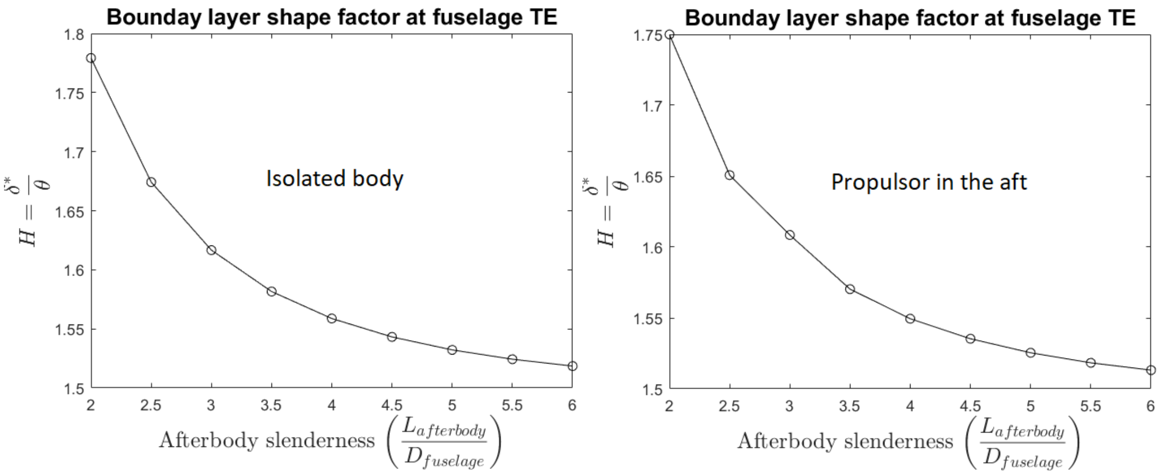

Figure 4.16: Change in shape factor at the fuselage TE due to propulsor for different fuselage afterbody slenderness values (Euler-IBLT). $M = 0.8$.

Quantity	$\frac{L_{afterbody}}{D_{fuselage}} = 2.5$	$\frac{L_{afterbody}}{D_{fuselage}} = 6$	Difference
$\frac{D_{propulsor}}{D_{fuselage}} = 1$			
C_D	0.079498	0.064927	-18.33 %
C_P	0.035034	0.030835	-11.99 %
$C_{\dot{A}S}$	0.032404	0.028584	-11.79 %
$PSC_{strict}(\%)$	2.59	2.25	-0.34
$\left(\frac{\dot{A}_{prop}-\dot{A}_{iso}}{\dot{A}_{iso}}\right)_{TE}(\%)$	-0.0703	0.16	NA
$\frac{D_{propulsor}}{D_{fuselage}} = 0.5$			
C_D	0.08371	0.065652	-21.57 %
C_P	0.033436	0.029476	-11.84 %
$C_{\dot{A}S}$	0.032466	0.028611	-11.87 %
$PSC_{strict}(\%)$	7.04	6.56	-0.48
$\left(\frac{\dot{A}_{prop}-\dot{A}_{iso}}{\dot{A}_{iso}}\right)_{TE}(\%)$	0.12	0.26	NA

Table 4.4: BLI configuration results for two fuselage afterbody slenderness values (RANS). $F_x = 0$, and $M = 0.8$.

4.4. FUSELAGE SLENDERNESS

The effect of afterbody slenderness has already been studied and the slenderness of fuselage on the whole is another possibility for study. Varying the length of the fuselage by fixing all other parameters is indeed a study of the effect of Reynolds number. It is a well-known fact that the increase in fuselage length with all other parameters fixed causes an increase in drag and naturally the surface dissipation in an isolated configuration. The exact benefit due to BLI, on the other hand, can still be analyzed by calculating the ideal and the strict PSC values. This section thus presents an analysis of boundary layer ingestion for different fuselage slenderness.

4.4.1. ANALYSIS USING EULER-IBLT SOLVER

Starting as usual with the Euler-IBLT solver, the analysis is performed for different fuselage slenderness values which are 5, 6, 7, 8, 9, 10, 11, 11.12 (baseline) , and 12. The Reynolds number varies corresponding to the fuselage length. All other parameters like the fuselage diameter, shape curves and the flow conditions are kept the same as that of the baseline (details in table 3.8). The selection of fuselage slenderness values is based on the possible values for different conventional aircraft types as given in [46] (table in appendix B.1). An important aspect of the present section is the laminar to turbulent transition location with respect to the total fuselage length. Since the fuselage length is considerably reduced at lower fuselage slenderness values, the region of laminar and turbulent flow become comparable which is expected to cause an increase in the ideal power saving coefficient.

The DSE results are presented in figure 4.17 for different fuselage slenderness values. The results confirm to the intuitive expectations in a qualitative sense. The PSC_{ideal} value decreases as there is turbulent flow over a greater percentage of the fuselage length at higher fuselage slenderness values as described in the previous paragraph.

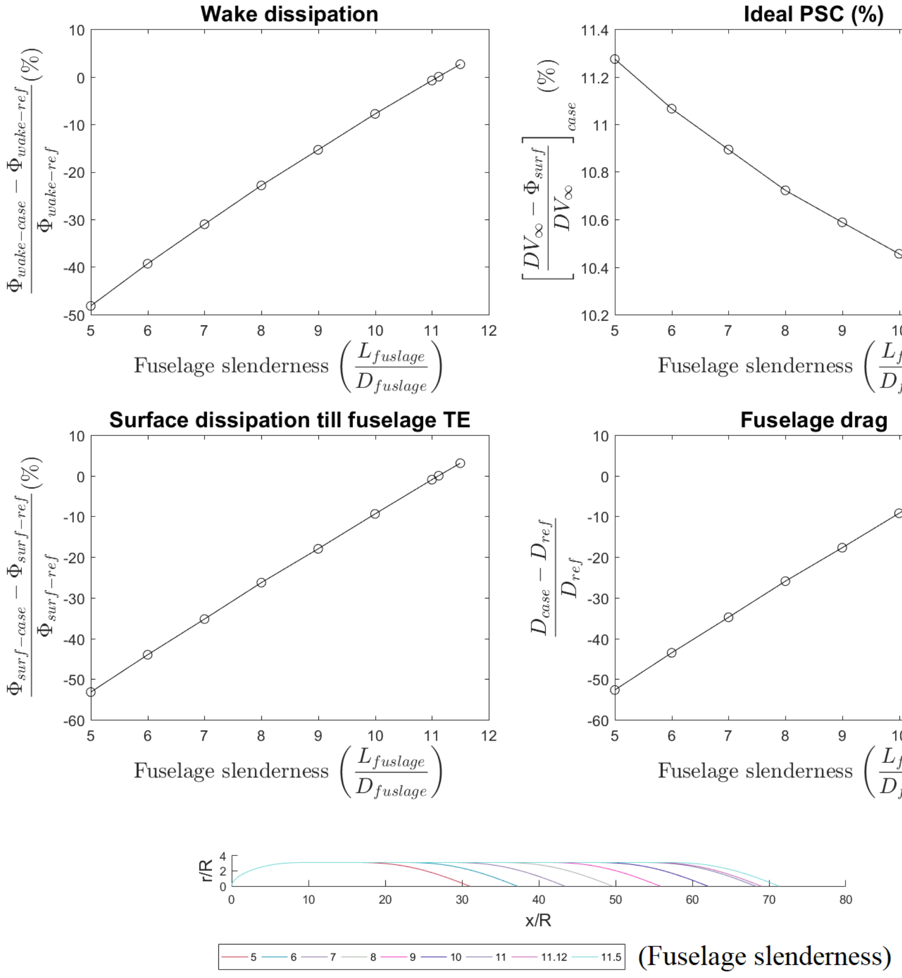

Figure 4.17: Design space exploration (Euler-IBLT) results for different overall fuselage slenderness (isolated body). $F_x = D$, and $M = 0.8$.

Further adding a propulsor at the aft of the fuselages, the power consumed and PSC_{strict} can be analyzed. These results are presented in figure 4.18. The results again highlight the validity of the isolated body dissipation analysis when comparing the power consumption of the BLI configurations. The surprise here is the fact that the PSC_{strict} behaves opposite to the PSC_{ideal}. It would be rather wiser to do a clearer analysis using the RANS solver before arriving at any conclusions. The surface dissipation change and the boundary shape factor change at fuselage TE are as usual presented in figures 4.15 and 4.16 respectively.

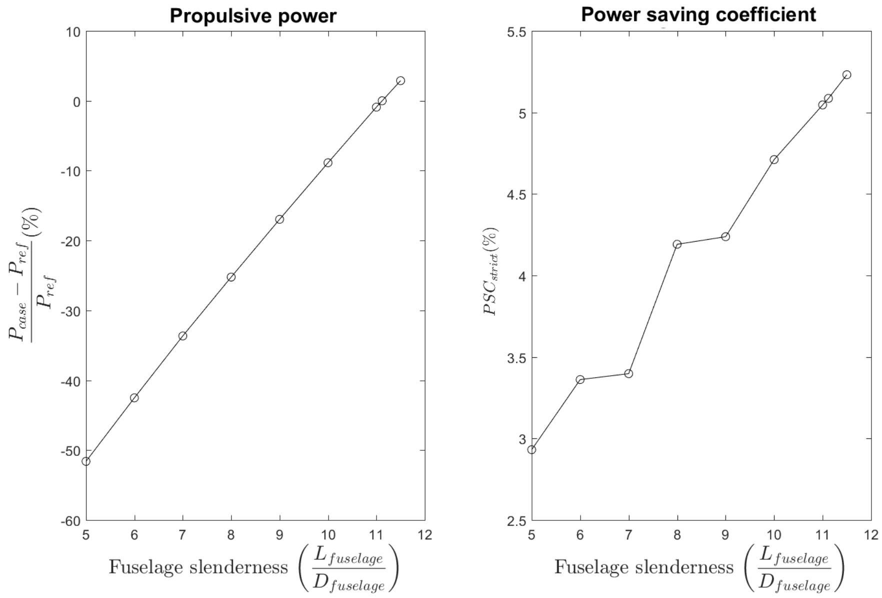

Figure 4.18: Design space exploration (Euler-IBLT) results for different overall fuselage slenderness (BLI configuration). $F_x = 0$, and $M = 0.8$.

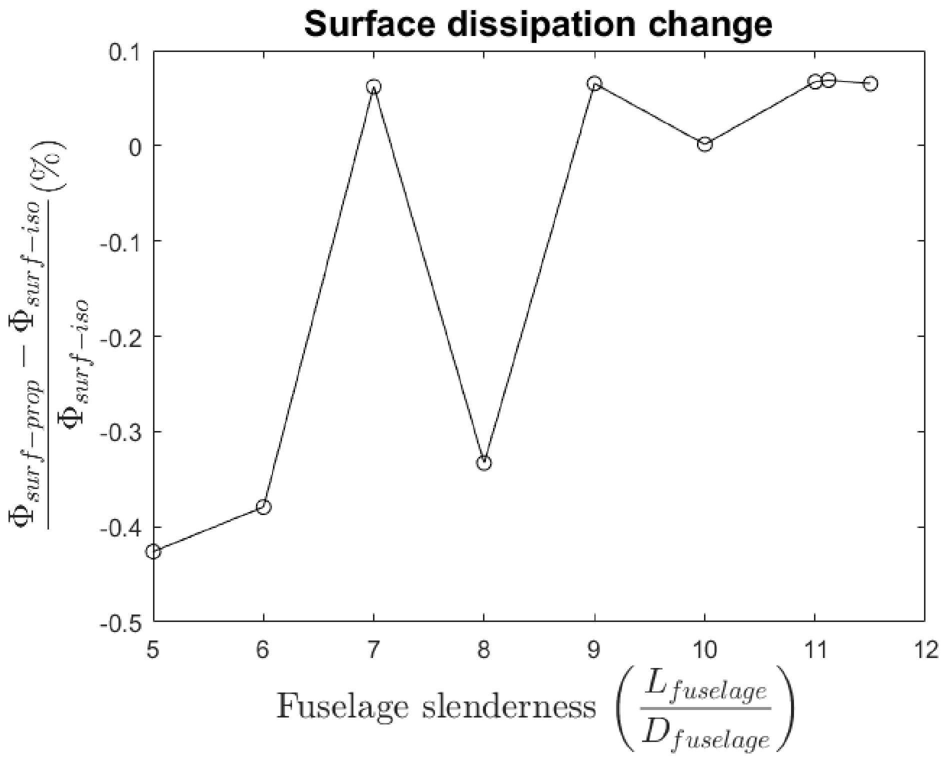

Figure 4.19: Surface dissipation change due to propulsor for different overall fuselage slenderness (Euler-IBLT). $M = 0.8$.

It is clear again from figure 4.19 that the surface dissipation is not changed to any appreciable value and also from this specific case it is quite clear that any attempt to provide a qualitative reasoning for the dissipation change for different designs is meaningless as the change is in the same order of the numerical error. The

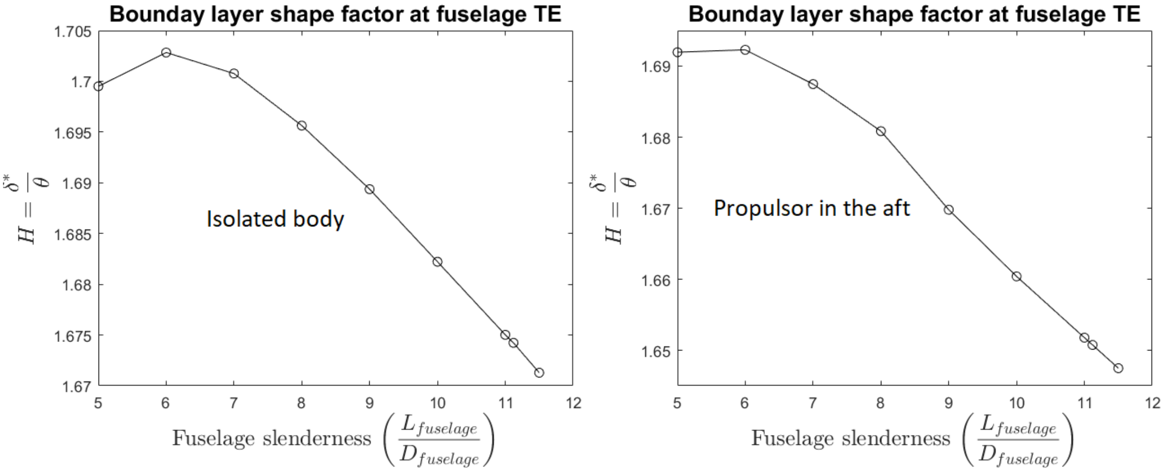

Figure 4.20: Change in shape factor at the fuselage TE due to propulsor for different overall fuselage slenderness (Euler-IBLT). $M = 0.8$.

change in the boundary layer shape factor (as given in figure 4.20) at the fuselage trailing edge, as usual, is expected to decrease when the propulsor is added. Also, the decreasing trend of the shape factor (at fuselage TE) with the fuselage slenderness is expected due to increasing Reynolds number (due to more turbulent flow over the fuselage).

4.4.2. ANALYSIS USING RANS SOLVER

Analysis using RANS solver becomes important again. Especially, for this case, the opposite PSC_{ideal} and PSC_{strict} trend needs a clarification for which RANS results of different cases are necessary to arrive at some meaningful conclusion. The RANS results are considered for the fuselage slenderness of 5 (and for the baseline). The comparison of the isolated body result for this fuselage slenderness and the baseline value of 11.12 are given in table 4.5.

Quantity	$\frac{L_{fuselage}}{D_{fuselage}} = 11.12$	$\frac{L_{fuselage}}{D_{fuselage}} = 5$	Difference
C_D	0.071934	0.033886	-52.89 %
$C_{\Phi S}$	0.031160	0.014087	-54.79 %
$C_{\dot{A}S}$	0.032427	0.014830	-54.27 %
$\left(\frac{\dot{E}-P_V}{DV_\infty}\right)_{TE}$ (%)	13.36	16.85	3.49
$\left(\frac{\Phi}{DV_\infty}\right)_{TE}$ (%)	86.64	83.14	-3.49
$\left(\frac{\dot{\varepsilon}}{DV_\infty}\right)_{TE}$ (%)	9.84	12.47	2.63
$\left(\frac{\dot{A}}{DV_\infty}\right)_{TE}$ (%)	90.16	87.53	-2.63

Table 4.5: Isolated body results for two overall fuselage slenderness values (RANS). $F_x = D$, and $M = 0.8$.

The results for surface dissipation and drag are close to the Euler-IBLT predictions on the basis of the difference from the baseline case. Also, the PSC_{ideal} results from the Euler-IBLT solver show at least a qualitative match with the percentage of $\dot{E} - P_V$ and $\dot{\varepsilon}$ in wake flow from RANS solver (meaning the quantities decrease with increasing slenderness). Next the results for the BLI configuration are presented in table 4.6.

The result for the BLI configurations now indeed suggests that the modeled propulsor is unable to effectively use the power available in the wake at lower fuselage slenderness. To analyze this a splitting of the composition of exergy can be used to get an idea. But this is better to be done separately for all cases and is presented in section 4.8 in figure 4.37. The reason is mentioned here to be due to the high thermal exergy at the fuselage TE. The propulsor modeled is naturally less efficient in utilizing this.

Quantity	$\frac{L_{fuselage}}{D_{fuselage}} = 11.12$	$\frac{L_{fuselage}}{D_{fuselage}} = 5$	Difference
$\frac{D_{propulsor}}{D_{fuselage}} = 1$			
C_D	0.079498	0.037046	-53.40 %
C_P	0.035034	0.016641	-52.50 %
$C_{\dot{A}S}$	0.032404	0.014729	-54.55 %
$PSC_{strict}(\%)$	2.59	1.78	-0.81
$\left(\frac{\dot{A}_{prop}-\dot{A}_{iso}}{\dot{A}_{iso}}\right)_{TE}$ (%)	-0.0703	-0.68	NA
$\frac{D_{propulsor}}{D_{fuselage}} = 0.5$			
C_D	0.08371	0.038968	-53.45 %
C_P	0.033436	0.016033	-52.05 %
$C_{\dot{A}S}$	0.032466	0.014748	-54.57 %
$PSC_{strict}(\%)$	7.04	5.37	-1.67
$\left(\frac{\dot{A}_{prop}-\dot{A}_{iso}}{\dot{A}_{iso}}\right)_{TE}$ (%)	0.12	-0.55	NA

Table 4.6: BLI configuration results for two overall fuselage slenderness values (RANS). $F_x = D$, and $M = 0.8$.

4.5. FLIGHT SPEED

An important aspect of power consumption is the speed of flight. For example, the cruise Mach number of the D8 Double Bubble concept aircraft by MIT was reduced from 0.8 to 0.72 to allow for the better BLI engine performance by reducing the incoming flow distortion as explained in [47]. Low Mach numbers also help improve nacelle aerodynamic performance by eliminating wave drag [47]. As such the study of the flow distortion is out of the scope of the present thesis and the power consumption variation with flight speed and the respective effect of the BLI engine at the chosen speeds would be presented in the present section. Since the flight speed is considered, the Mach number can be used to present the results but it must be clear that the Reynolds number is still variable since the fluid properties and the fuselage length are fixed during the studies which are a requirement for realistic flights.

4.5.1. ANALYSIS USING EULER-IBLT SOLVER

The study is not only fast but is much simpler especially for the present case as compared to the RANS solver as the mesh details and the flight speed are interdependent for successful RANS simulations. For example the $y^+ < 1$ condition needs to be carefully considered for the required cases (depending on the turbulence model) and also the presence of shock waves requires careful handling of the mesh details in the RANS solver. The Euler-IBLT solver, on the other hand, does not require any special effort but still, an important limitation is that the calculation of dissipation due to shock is not very straightforward at least when a propulsor is attached (or if the flow has swirl).

The DSE results are presented for the baseline fuselage geometry (as defined in table 3.27) with variable flight speed. The Mach numbers corresponding to the flight speeds explored are $0.2, 0.3, 0.4$, $0.5, 0.6$, $0.7, 0.8, 0.85, 0.9$, and 0.95. The results for isolated body analysis are presented in figure 4.21. The surface dissipation is expected to increase with flight speed and is clear from the figure 4.21. The sudden rise in the dissipation towards the end is due to the generation of shock waves. A shock wave is actually generated at the Mach of 0.9 also but is weak unlike the one at Mach 0.95. The power saving coefficient is not observed to vary much except at Mach 0.95 where there is a sudden drop of power saving due to the presence of a strong shock wave which results in a higher dissipation.

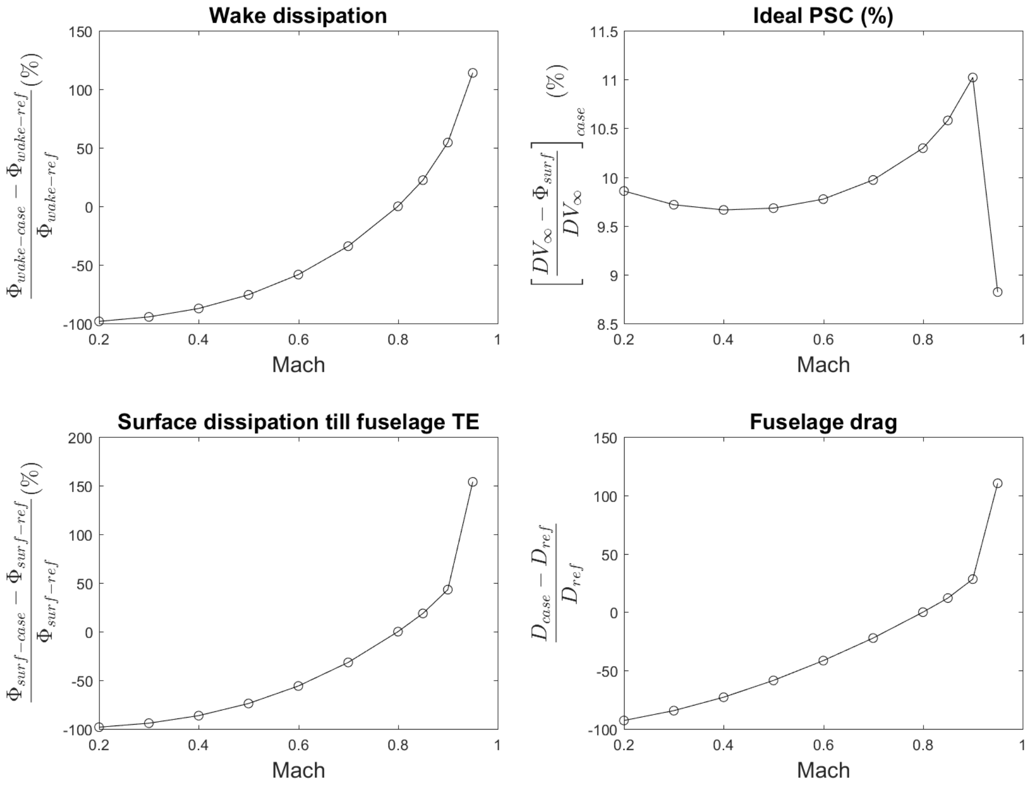

Figure 4.21: Design space exploration (Euler-IBLT) results for baseline fuselage geometry at different flight speeds (isolated body). $F_x = D$.

Since attaching a BLI propulsor has the capability to change the flow speed ahead of it, the effect of it at near sonic speeds could be interesting. The Mach 0.9 case is chosen for this as the Mach 0.95 case is not of much interest for transonic flights due to the bad performance as a result of high wave drag. The study of the Mach 0.9 case would be done later using RANS solver. Also, the changing transition location with Mach number could result in interesting results at lower Mach numbers as well. The results of Mach number DSE for BLI configuration is given in figure 4.22. Again it is trivial that the lower Mach numbers require less power. The power saving coefficient (PSC_{strict}), on the other hand, increases almost by 3% from Mach 0.2 to Mach 0.9. This will be discussed once the results from the RANS solver are presented for verification. And it becomes quite clear based on all the design space exploration studies that the fuselage drag in isolated configuration itself is a sufficiently good qualitative indicator of the fuselage aerodynamic performance even if the configuration is a BLI setup (at least for the considered type of setups).

Next, as usual, the change in dissipation and shape factor at fuselage trailing edge are presented in figures 4.23 and 4.24 respectively. It should be noted that the dissipation change results are not presented for Mach 0.9 and 0.95 as the inviscid drag coefficient result from MTFLOW (definition can be found in manual [21]) was used during isolated body analysis to predict the wave drag power but this is not separable from the propulsor thrust contribution in integrated configuration. The only other method is to perform integral calculations (based on total pressure change as described in [1]) close to the shock location in the inviscid field. A definite demarcation of such a location is not a very straightforward to arrive at any reliable quantitative result and is not done as anyways the performance of fuselage is bad at such high Mach numbers. The dissipation change is negligible as can be observed from figure 4.23. Also, as usual, the propulsor is observed to cause a minor change in boundary layer shape factor at fuselage TE. The variation of the shape factor with flight speed shows a decreasing trend.

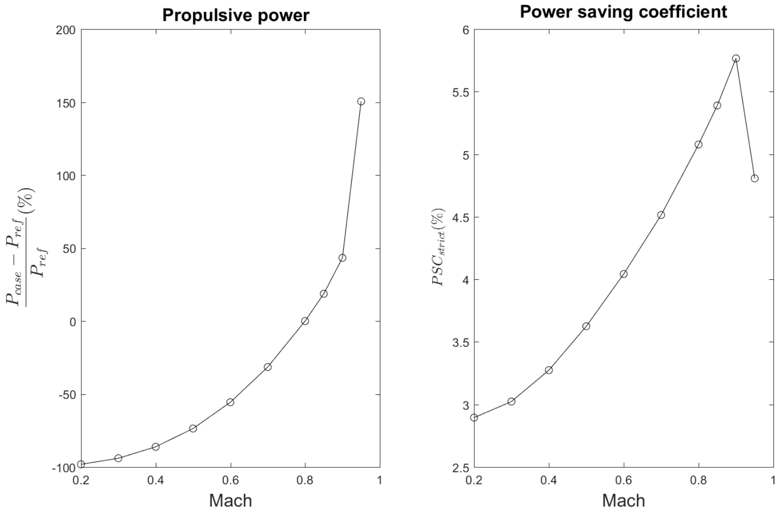

Figure 4.22: Design space exploration (Euler-IBLT) results for baseline fuselage geometry at different flight speeds (BLI configuration). $F_x = 0$.

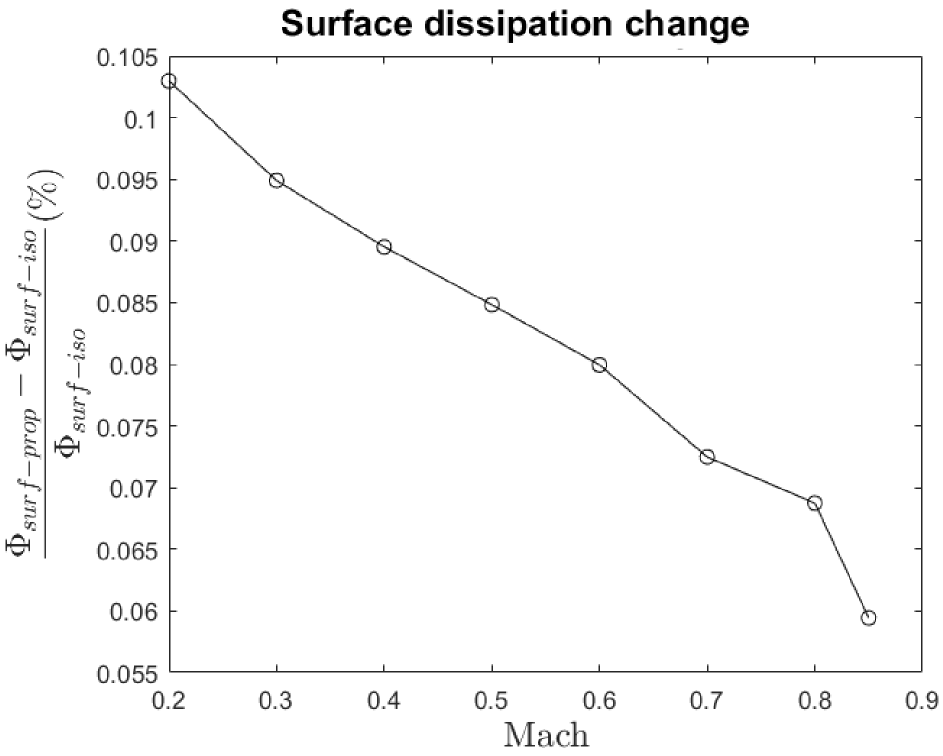

Figure 4.23: Surface dissipation change due to propulsor for different flight speeds (Euler-IBLT).

4.5.2. ANALYSIS USING RANS SOLVER

This analysis becomes important as usual especially to obtain a more dependable value of PSC (ideal and strict). It should also be noted that the shock waves cause a conversion of mechanical energy to heat which can still be an exergy source. This analysis can be performed at least for the case of Mach 0.9 which has a weak shock. At Mach 0.95, the performance is deteriorates anyways and this case is avoided as it has less significance for transonic flights. To start with, the results for isolated fuselage analysis are presented for the flight speeds corresponding to Mach numbers of 0.2, 0.8 and 0.9 in table 4.7.

The results obtained suggest various important details. First, the variation of the surface dissipation and

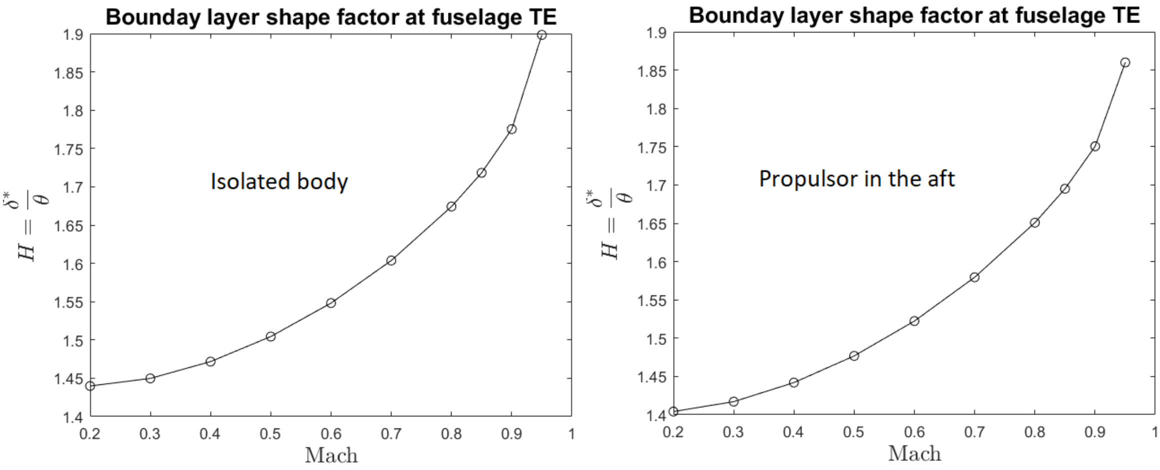

Figure 4.24: Change in shape factor at the fuselage TE due to propulsor for different flight speeds (Euler-IBLT).

Quantity	$M = 0.8$ (baseline)	$M = 0.2$	$M = 0.9$	Difference (for $M = 0.2$)	Difference (for $M = 0.9$)
C_D	0.071934	0.08521	0.07357	-92.60 % (for drag)	29.44 % (for drag)
$C_{\Phi S}$	0.031160	0.03842	0.0307	-98.07 % (for Φ)	40.28 % (for Φ)
$C_{\dot{A}S}$	0.032427	0.03898	0.03242	-98.12 % (for $\dot{A}$)	42.36 % (for $\dot{A}$)
$\left(\frac{\dot{E}-P_V}{DV_\infty}\right)_{TE}$ (%)	13.36	9.82	16.55	-3.56	3.18
$\left(\frac{\Phi}{DV_\infty}\right)_{TE}$ (%)	86.64	90.18	83.46	3.56	-3.18
$\left(\frac{\dot{\varepsilon}}{DV_\infty}\right)_{TE}$ (%)	9.84	8.51	11.86	-1.34	2.02
$\left(\frac{\dot{A}}{DV_\infty}\right)_{TE}$ (%)	90.16	91.49	88.14	1.34	-2.02

Table 4.7: Isolated body results for three different flight speeds (RANS). The difference values next to coefficients are for the actual variable (like drag) and not the coefficients. $F_x = D$.

the surface anergy rate match closely with the solution from the Euler-IBLT solver (comparing differences from baseline as in figure 4.21). The variation of PSC_{ideal} is qualitatively similar to the result from the Euler-IBLT solver for $M = 0.2$ when compared with the baseline ($M = 0.8$). The lesser PSC_{ideal} at lower Mach numbers could be attributed to the lower boundary layer shape factor in general (can be observed in figure 4.24 at fuselage TE). The differences in the values of shape factor (at fuselage TE) are especially more noticeable for the flight speed parameter. Higher shape factor value at fuselage TE (at higher flight speeds) means that the dissipation in wake would be higher (hinted from figure A.2) giving higher PSC_{ideal} with increasing flight speeds (till a strong shock is produced). At $M = 0.2$, the fuselage surface anergy rate and the dissipation match closely due to effective flow incompressibility. Also, the variation in PSC_{ideal} based on $\dot{E} - P_V$ value for $M = 0.2$ case is closer to the result from the Euler-IBLT solver. One reason for this can be argued to be due to less significant thermal effects in the flow. But other modeling details of the Euler-IBLT solver must also be considered and the results must be viewed critically.

The result for $M = 0.9$, on the other hand, shows a qualitative match with the PSC_{ideal}. Difference between the percentage of $\dot{E} - P_V$ and $\dot{\varepsilon}$ is quite high due to the higher temperature gradients in the system (due to weak shock) compared to other cases. The results for fuselage surface dissipation and anergy rate match closely with the result from the Euler-IBLT solver (when comparing with respect to the baseline value as usual).

Next, the results for the cases with the propulsor installed are presented in table 4.8. The results of the power consumption are in agreement with the result from the Euler-IBLT solver and also the surface anergy rate is not affected by the propulsor pressure field for high and low Mach numbers of interest. As far as the power saving coefficient (strict) is concerned, the trend is opposite to that observed in the Euler-IBLT solver. Although the available exergy is low at lower Mach number, the modeled propulsor is able to extract the most of it due to the fact that thermal energy is lesser at lower Mach number (the thermal energy effects, on the other hand, are not captured correctly by the Euler-IBLT solver). The modeled propulsor is more effective in extracting mechanical energy. At higher Mach number, the production of shock results in the conversion of more of the power into heat and this may need a special propulsor design. Also, in reality, on a quantitative perspective, the PSC_{strict} value is not very different for the different Mach numbers (when compared to changes in power consumption) and an analysis of trend may not be very interesting in the first place.

Quantity	$M = 0.8$ (baseline)	$M = 0.2$	$M = 0.9$	Difference (for $M = 0.2$)	Difference (for $M = 0.9$)
$\frac{D_{propulsor}}{D_{fuselage}} = 1$					
C_D	0.079498	0.091950	0.082596	-92.77 % (for drag)	31.49 % (for drag)
C_P	0.035034	0.041339	0.035815	-98.16 % (for power)	45.56 % (for power)
$C_{\dot{A}S}$	0.032404	0.039122	0.032479	-98.11 % (for $\dot{A}$)	42.71 % (for $\dot{A}$)
$PSC_{strict}(\%)$	2.59	2.97	2.64	0.38	0.05
$\left(\frac{\dot{A}_{prop}-\dot{A}_{iso}}{\dot{A}_{iso}}\right)_{TE}$ (%)	-0.0703	0.36	0.17	NA	NA
$\frac{D_{propulsor}}{D_{fuselage}} = 0.5$					
C_D	0.08371	0.09582	0.087439	-92.85 % (for drag)	32.20 % (for drag)
C_P	0.033436	0.03935	0.034243	-98.16 % (for power)	45.82 % (for power)
$C_{\dot{A}S}$	0.032466	0.0391822	0.032564	-98.11 % (for $\dot{A}$)	42.81 % (for $\dot{A}$)
$PSC_{strict}(\%)$	7.04	7.64	6.91	0.62	-0.13
$\left(\frac{\dot{A}_{prop}-\dot{A}_{iso}}{\dot{A}_{iso}}\right)_{TE}$ (%)	0.12	0.52	0.44	NA	NA

Table 4.8: BLI configuration results for three different flight speeds (RANS). The difference values next to coefficients are for the actual variable (like drag) and not the coefficients. $F_x = 0$.

Also, the PSC_{strict} value for the $M = 0.2$ case with the smaller propulsor (in table 4.8) is very close to the maximum exergy value (PSC_{ideal}) from isolated body simulation (in table 4.7). This is, on one hand, possible due to the high shape factor value (as compared to a flat plate) of the boundary layer at the fuselage trailing edge but at the same time could be a minor over prediction due to random numerical error. It should be noted that the high shape factor of boundary layer implies a requirement of a close to uniform pressure jump (or uniform momentum source) for achieving a boundary layer/wake filling.

4.6. PROPULSOR LOCATION

Different design space studies performed before clearly highlight the fact that the surface dissipation and surface anergy is unaffected by the addition of propulsor at the immediate aft of the fuselage in the considered flight regimes. But an important concern in all the above studies is the fact that the propulsor installation location should be actually possible in practice. Even if one attaches an open rotor at the aft part of the fuselage afterbody, some of the surface dissipation would still take place after the propeller on the remaining fuselage body. Also, the available power (or exergy) in the flow is modified depending on the propulsor location. This section aims to perform a preliminary analysis of the effect of the location of the propulsor on different details relevant to BLI. Fuselage geometry is not specially modified for the Novel concept in anyways in this section and is kept for the next chapter.

4.6.1. ANALYSIS USING EULER-IBLT SOLVER

Starting with the Euler-IBLT solver, the total surface dissipation is analyzed. It should be understood that this solver as such causes certain changes to the already existing boundary layer on the surface by changing the static pressure field. Unlike most of the previous cases, the propulsor position ahead of the trailing edge results in an inevitable interaction of the propulsor plume with the surface boundary layer behind the propulsor. Although the previous results are very convincing from the perspective of the surface dissipation and surface anergy flow change, the presence of a fuselage part behind the propulsor leads to additional confusion related to the interaction of exhaust plume and boundary layer. As such this problem cannot be completely handled using the Euler-IBLT solver due to its limitations on the allowed propulsor size.

Anyways, it is still possible to analyze the power consumed by the propulsor for different propulsor positions. For the analysis, the area of the propulsor sections (like frontal and exit sections and rest interpolated linearly) are maintained the same as that of the propulsor at the fuselage TE. The result for fuselage surface dissipation change is given in figure 4.25. The results clearly show certain important aspects of BLI. The propulsors away from fuselage in the wake do not lose much performance (slow deterioration is, of course, expected) due to the fact that the dissipation in the wake is always slower than on the surface of a body as observed from the different power balance plots of various bodies throughout the thesis. The modeled propulsors located on the fuselage body cannot effectively achieve a good filling due to the presence of the fuselage surface in their aft. This results in more noticeable performance deterioration.

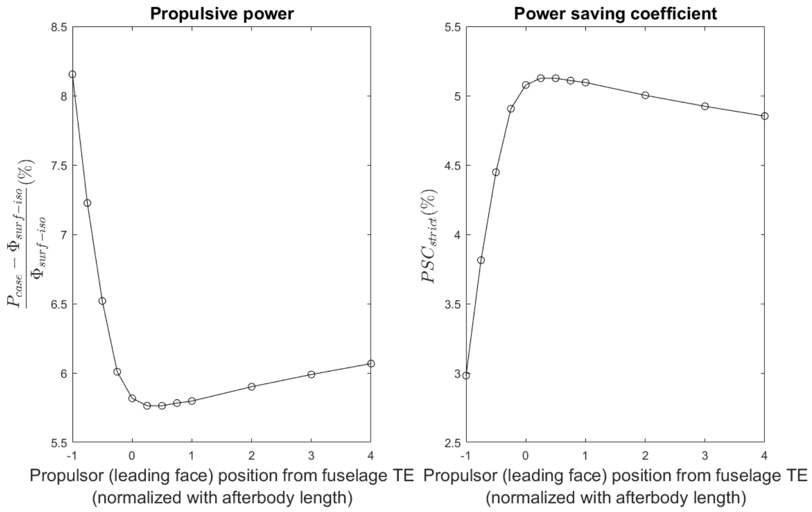

Figure 4.25: Design space exploration (Euler-IBLT) results for baseline fuselage geometry with propulsor at different locations (BLI configuration). $F_x = 0$, and $M = 0.8$.

Further, the change in dissipation at the fuselage TE could be obtained but only one propulsor radius is not sufficient to arrive at conclusions. It should be noted that smaller propulsors are more interesting due to practical reasons. Also, the benefit of BLI must not be offset too much due to an increase in propulsor weight (the analysis of weight is out of scope). But in any case, for the chosen propulsor radius (equal to fuselage radius), the surface dissipation change results are presented in figure 4.26. It should be noted that the separation of the dissipation due to the exhaust plume (till fuselage TE) and the fuselage surface dissipation is not very straightforward. Actually, the exhaust plume is difficult to be separately defined. But it should also be noted that exhaust plume of the modeled propulsor has no separate viscous effects (apart from interacting with the body boundary layer and wake) in the Euler-IBLT solver. This means that calculating the fuselage (with the propulsor) boundary layer dissipation is an attempt to capture the surface dissipation and the probable interaction of the propulsor plume with the boundary layer. But the boundary layer also changes the exhaust plume due to coupling and the exact dissipation which is responsible for power consumption is still a bit hazy for such cases. Anyways the dissipation observed till the fuselage TE from figure 4.26 is less than a percent for all cases except the most extreme case of placing the propulsor at the start of the fuselage afterbody. Thus, this does suggest that the propulsor plume interaction with the fuselage surface could cause a minor increase in the surface dissipation due to the boundary layer.

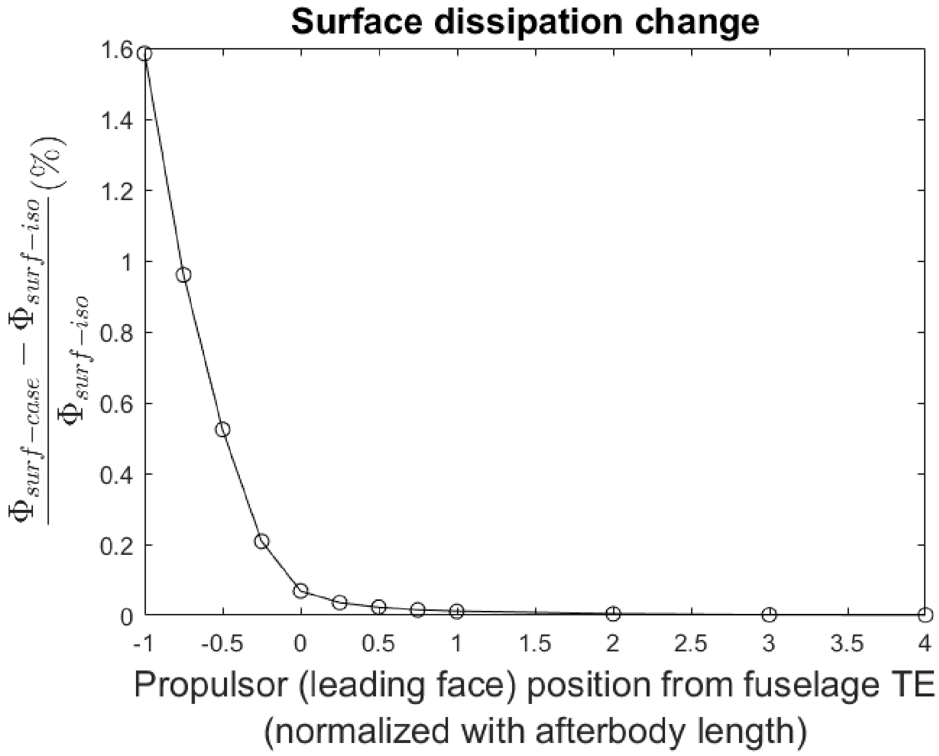

Figure 4.26: Dissipation (till fuselage TE) change due to propulsor for different propulsor installation locations (Euler-IBLT). $M = 0.8$.

4.6.2. ANALYSIS USING RANS SOLVER

As mentioned earlier it becomes imperative to perform RANS analysis using smaller propulsors to study the relevant anergy changes and power savings. It should be noted that it is still not straightforward to directly obtain the actual surface anergy rate change as done in previous cases. This is because the surface anergy at the fuselage TE would include the anergy rate change due to the exhaust plume also and it is not possible to separate the contributions of the fuselage part boundary layer behind the propulsor and the exhaust plume (not even to the extent to which it was possible in the Euler-IBLT solver). This makes one depend on the propulsor power consumption (which may just be satisfactory for preliminary suggestions) to determine if there could possibly be any significant interaction of propulsor exhaust plume and the fuselage part behind the propulsor.

Thus, for this study, propulsors of three different sizes are chosen. The areas of the sections of the propulsors are maintained (like front and exit sections and rest linearly interpolated) the same as the propulsors that can be placed in the fuselage TE. For example, a propulsor corresponding to a fuselage TE propulsor of $R_{propulsor}/R_{fuselage} = 0.5$ at some other location on the fuselage would have the same corresponding cross-sectional areas. The propulsors are chosen to be located at $-0.75 \times L_{afterbody}$ from the fuselage TE. The relevant results are presented in figures 4.27 and 4.28.

The results for PSC_{strict} show that the propulsor located at $L_{fuselage} - 0.75 L_{afterbody}$ performs similar to the propulsor at fuselage TE at least qualitatively. But the difference in the PSC_{strict} value, especially for the smallest considered propulsor, is much lesser for the propulsor on the fuselage than the one at fuselage TE. The reason could vary from the available exergy in the boundary layer upstream of the propulsor to a possible unfavorable interaction of propulsor plume with the fuselage boundary layer. But a definite conclusion cannot be drawn.

The anergy rate change results on the other hand in figure 4.28 clearly show that the fuselage surface anergy rate upstream of the propulsor is unaffected irrespective of the propulsor size. But the anergy rate at the fuselage TE is quite different for the different propulsor sizes which is, of course, expected as the exhaust plume of the smaller propulsor is bound to cause more losses due to higher flow speeds. The main issue here

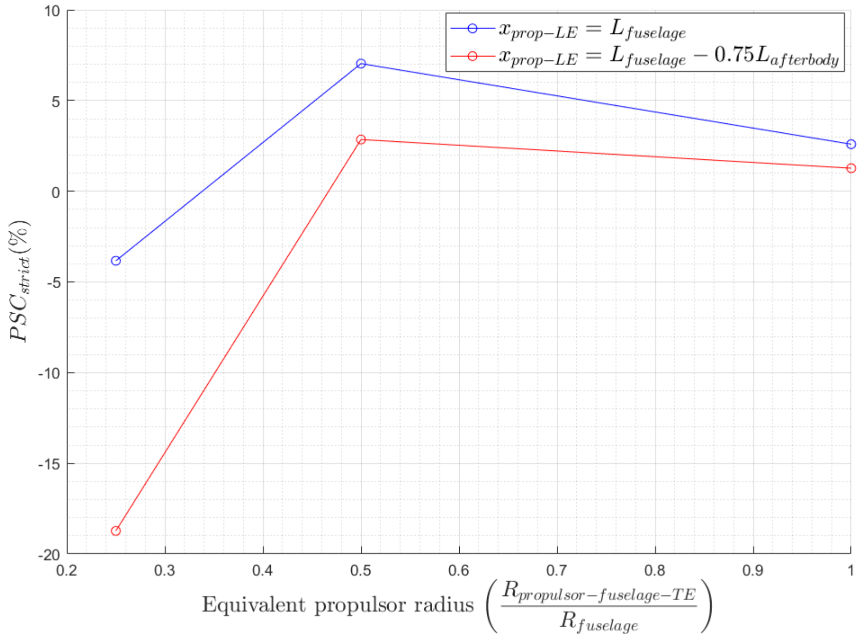

Figure 4.27: PSC_{strict} for different propulsor sizes located at $L_{fuselage} - 0.75L_{afterbody}$ (RANS). $F_x = 0$, and $M = 0.8$.

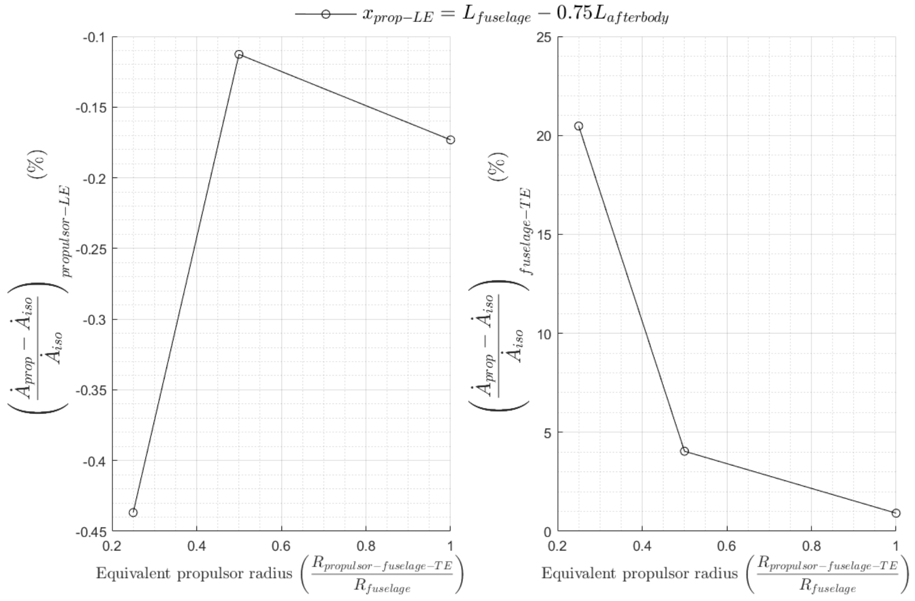

Figure 4.28: Change in anergy rate (at propulsor upstream and till fuselage TE) for different propulsor sizes located at two different locations (RANS). $M = 0.8$.

is that the interaction of the exhaust plume with the fuselage boundary layer cannot be explicitly determined. But one fact is very clear, that is the propulsor placed more ahead of the fuselage TE anyways performs badly whether or not there is any significant interaction of exhaust plume with fuselage surface. Also, from the Euler-IBLT dissipation change results (4.26), it is suggested that the interaction of propulsor exhaust plume and fuselage boundary layer could be more unfavorable if the fuselage part behind the propulsor is longer. Thus, attempt should be made to place the propulsor as close to fuselage TE as possible.

4.7. ALTITUDE

The aim of this section is just to give some idea regarding the variation of the fuselage surface dissipation and propulsor power consumption with flight altitude for a fixed Mach number. This would, of course be relevant for higher altitudes where transport flight usually takes place. But the results for a wide range of altitudes are given anyways. The pressure, density and temperature variations are calculated based on the ISA guidelines as described in [48]. Only the Euler-IBLT solver is used for the exploration in this case to keep the results short and to give a minimal idea about the sensitivities.

4.7.1. ANALYSIS USING EULER-IBLT SOLVER

The analysis for the isolated fuselage is first presented in figure 4.29. The power analysis for the propulsor in the BLI configuration is given figure 4.30. It is again mentioned that the Mach is fixed to be equal to that of the baseline (= 0.8). This results in decreasing velocity (and dynamic pressure) with increasing altitude (thus reducing drag). Finally, the change in surface dissipation when a propulsor is installed is shown figure 4.31.

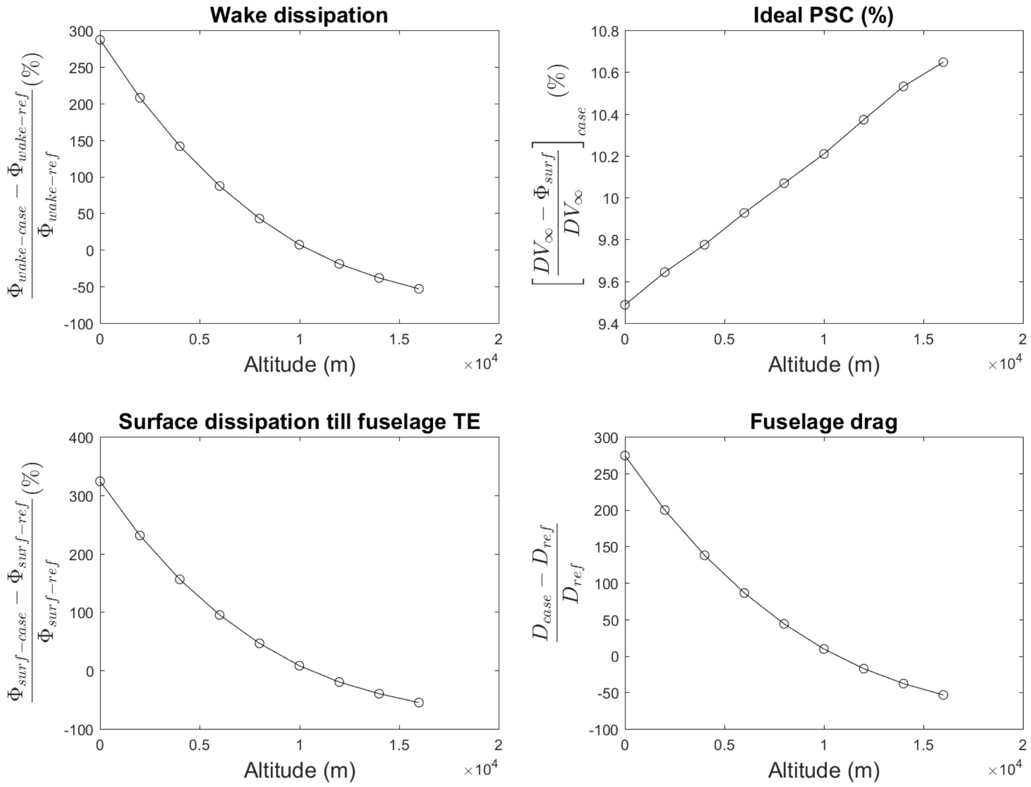

Figure 4.29: Design space exploration (Euler-IBLT) results for baseline fuselage geometry flying at different altitudes (isolated body). $F_x = D$, and $M = 0.8$.

The results for fuselage surface dissipation (isolated body analysis) and BLI propulsor power consumption (BLI analysis) show a matching trend as seen in figures 4.29 and 4.30. The PSC_{ideal} and PSC_{strict} show only a minor variation for the wide range of altitudes. Also, the surface dissipation does not change between propulsor installed and uninstalled setups as seen in figure 4.31.

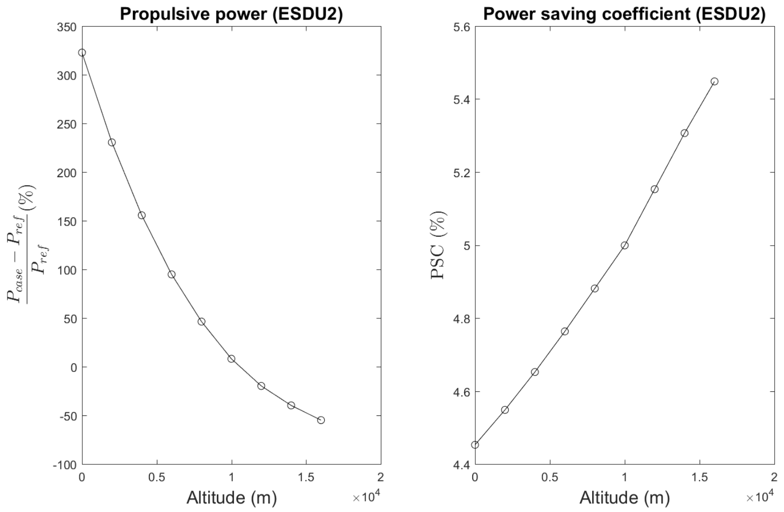

Figure 4.30: Design space exploration (Euler-IBLT) results for baseline fuselage geometry flying at different altitudes (BLI configuration). $F_x = 0$, and $M = 0.8$.

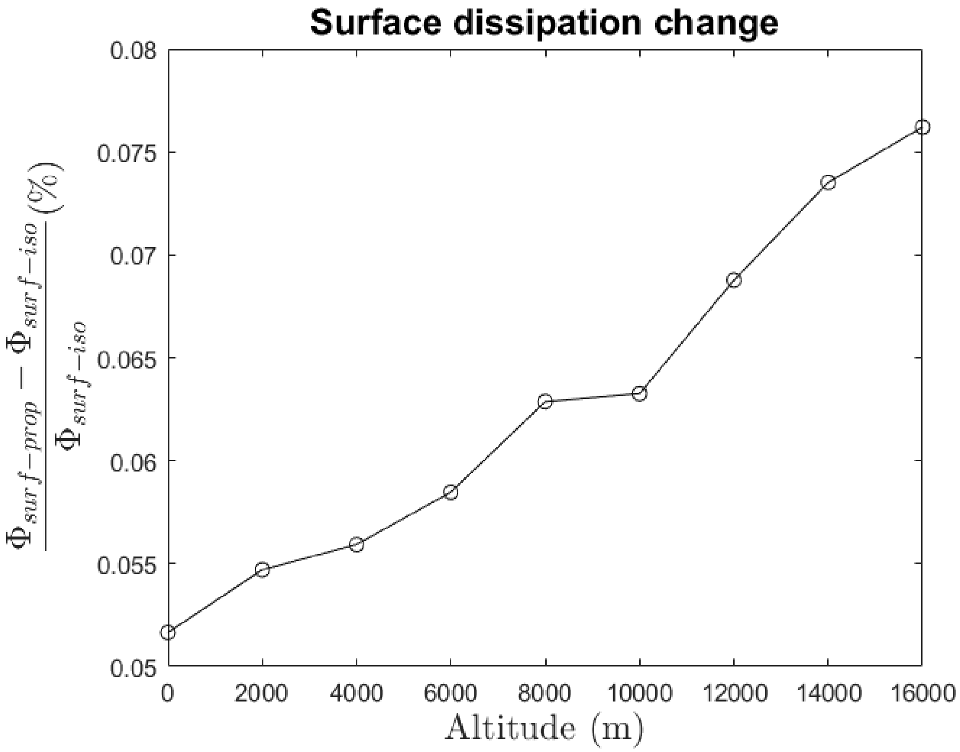

Figure 4.31: Surface dissipation change due to propulsor for different flight altitudes (Euler-IBLT). $M = 0.8$.

4.8. RESULT SUMMARY

Important results from the previous sections are put together for easy overall analysis in this section. Thus, a compilation of all the RANS results and important comparisons with the Euler-IBLT solver results are presented in this section.

The first important task would be to produce the available RANS results and the Euler-IBLT results in the same figure. The change in various quantities as compared to the baseline case is shown in different bar charts for the different fuselage geometry and flight condition parameters in figure 4.32. The changes from baseline, of course, have been calculated separately using the baseline results from the respective solvers. The results obtained clearly display that for comparing the differences between fuselage designs (or flight conditions), both the RANS and the Euler-IBLT solvers give close results (which is clearer to observe from figure 4.33). It should be noted that these differences in results between the solvers are only minor as in figure 4.33 when compared to the percentages shown in figure 4.32. It can also be noted that the surface dissipation and the anergy rate results (changes from the baseline case) are close for the RANS solver results. Finally, the isolated body analysis results (surface dissipation and anergy rate) and the BLI configuration results (power from different propulsors) are close (when changes from the baseline value are compared) suggesting that the isolated body analysis sufficiently covers the performance of fuselages for aft installed BLI propulsors. Also, since increasing the length of the afterbody is deteriorating for a simple isolated body and for a BLI configuration (with or without considering the probable unfavorable exhaust plume and fuselage interaction), in general, an isolated body analysis is already a good indicator of aerodynamic performance of fuselage even for BLI configurations. The minor differences in the results as in figure 4.33 (especially at Mach=0.9) is due to the difference in modeling between the solvers. It should be noted that the surface dissipation becomes less meaningful (and surface anergy rate must be used) at very high Mach numbers when thermal effects become important. The details regarding the exergy flow splitting is available in figure 4.37.

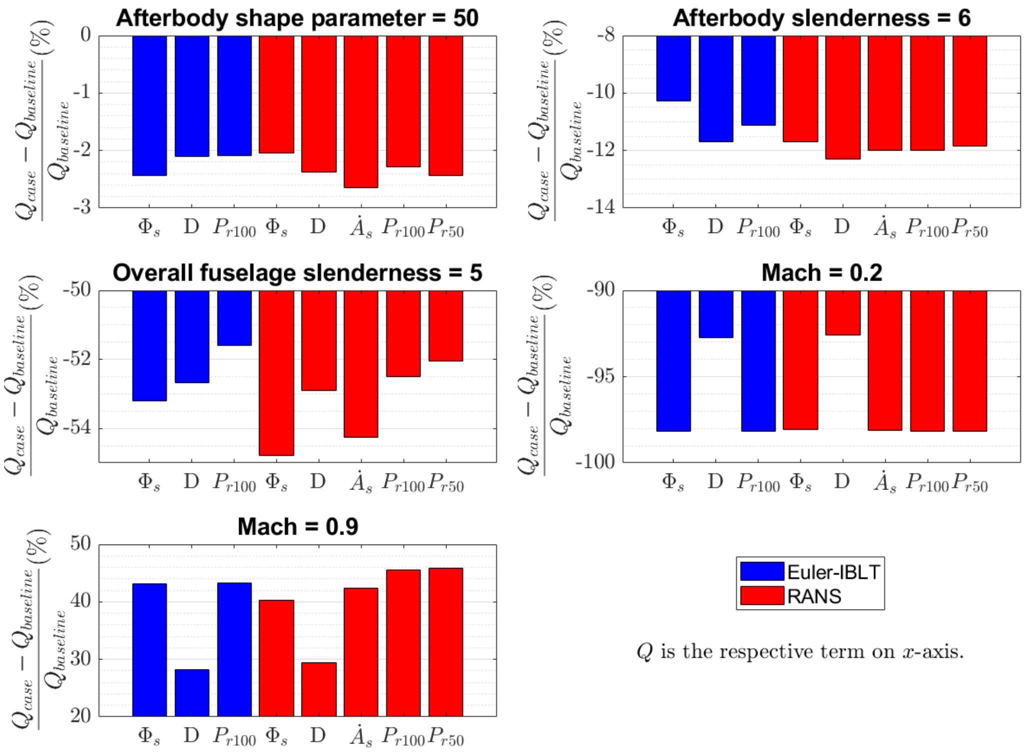

Figure 4.32: Comparison of changes (with respect to baseline) in power related terms and drag from Euler-IBLT and RANS solvers.

Next, it is also interesting to analyze the power saving coefficients as predicted by the different solvers. A comparison of the power saving coefficients as obtained using the Euler-IBLT and the RANS solvers for different cases can be found in figure 4.34 (difference are clearer in the chart in figure 4.35). It can be observed that except for the case of Mach 0.2 flight, the $\frac{\dot{E}-P_V}{DV_\infty}$ do not match (for the two solvers) but strangely the Euler-IBLT $\frac{\dot{E}-P_V}{DV_\infty}$ and RANS $\frac{\dot{\varepsilon}}{DV_\infty}$ match more closely (for most cases) which is good anyways (but must be viewed critically at the same time). It should be noted that the PSC_{strict} predicted by the Euler-IBLT solver is mostly higher than the value predicted by the RANS solver (except for Mach 0.2 case). All these seem to be an issue with capturing thermal effects correctly in the Euler-IBLT solver. For example, from equation 2.35 it can be observed that if the fluid thermal conductivity and viscous heating are not modeled (in the boundary layer),

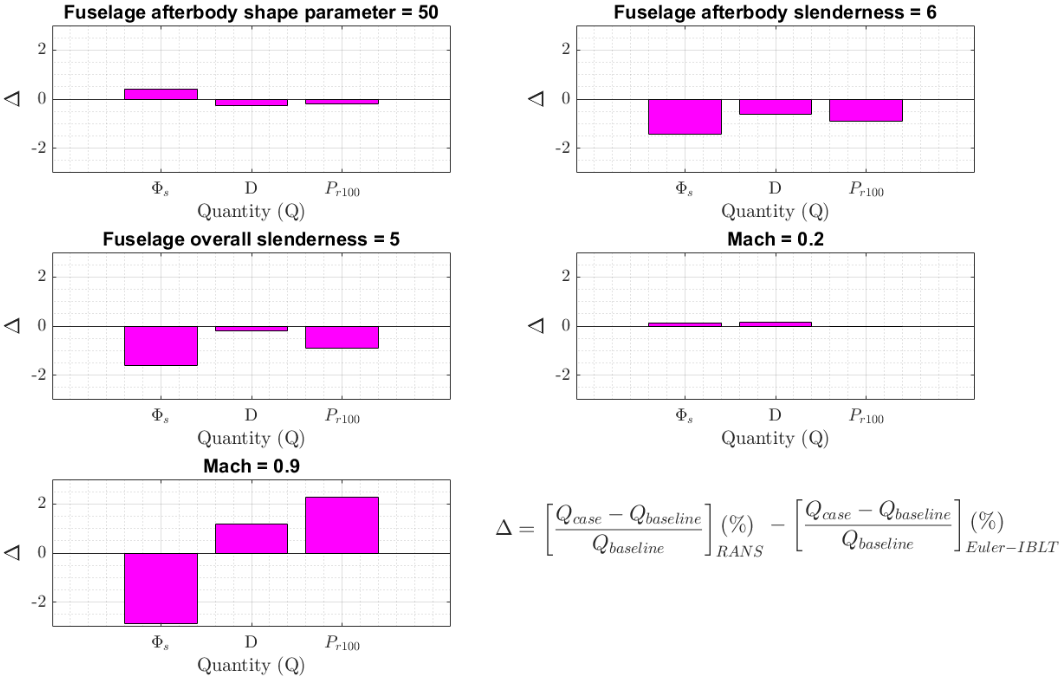

$$\Delta = \left[\frac{Q_{case} - Q_{baseline}}{Q_{baseline}}\right](\%)_{RANS} - \left[\frac{Q_{case} - Q_{baseline}}{Q_{baseline}}\right](\%)_{Euler-IBLT}$$

Figure 4.33: Differences of changes (with respect to baseline) in power related terms and drag from Euler-IBLT and RANS solvers.

the difference between dissipation and anergy rate would be zero. Since at higher Mach numbers, the thermal effects become more important, and since the boundary layer uses a mechanical energy formulation (in Euler-IBLT solver), the obtained value of viscous dissipation from the Euler-IBLT solver seems over-predicted. Also, the complete details of the modeled terms in the equations 2.50 and 2.51 can be found in [20]. The over prediction of the fuselage surface dissipation value in the Euler IBLT solver (leading to a lower $\frac{\dot{E}-P_V}{DV_\infty}$) at higher Mach numbers must be more carefully analyzed on the basis of validity of the thin boundary layer assumption and all the terms which are modeled in different ways for closure as well (which makes it even more complicated). It should be noted that the presence of thermal effects cannot be the only reason for the over prediction of the percentage of fuselage surface dissipation in the Euler-IBLT solver. This is especially because the over prediction was also observed for the NACA0040 BOR (which was at very low Mach and hence negligible thermal effects) as analyzed in section 3.3 (results in table 3.7). Thus, a combination of various modeling details in the Euler-IBLT solver can be concluded to be the reason for the differences as compared to the RANS results. Since the values of $\frac{\dot{E}-P_V}{DV_\infty}$ from the Euler-IBLT solver are close to the $\frac{\dot{\varepsilon}}{DV_\infty}$ values from the RANS solver, the over-prediction of PSC_{strict} when a propulsor is present can be argued to be due to the complete mechanical energy formulation of the boundary layer (unlike in RANS simulations where the propulsor may be affected by the thermal fields in the flow). But, on the other hand, the selection of a safe propulsor size is still a point to note which can cause mild over-predictions as seen before. But in any case unlike surface dissipation (or surface anergy rate) and the power consumed, the exact PSC_{strict} behavior may not be very interesting when comparing different fuselage designs (or flight conditions) as the changes involved are very small compared to the power related terms (like surface dissipation, surface anergy, and propulsor power). Thus, the absolute PSC_{ideal} and the PSC_{strict} values from the Euler-IBLT solver must be viewed with caution. However, for qualitative comparison of the fuselage designs (or flight conditions), they do not cause much of an issue.

Then to actually understand the differences in PSC_{ideal} and PSC_{strict} for different fuselage designs and flight conditions, figure 4.36 gives a grouped bar chart with all the values from the RANS solver. This clearly highlights the differences in different fuselage designs (or flight conditions). Certain details from the charts are worth mentioning. For example, the difference in percentages of $\dot{\varepsilon}$ and $\dot{E} - P_V$ is less for the Mach 0.2 case as the flow is effectively incompressible and thermal effects are not very significant. Also, the r50 propulsor

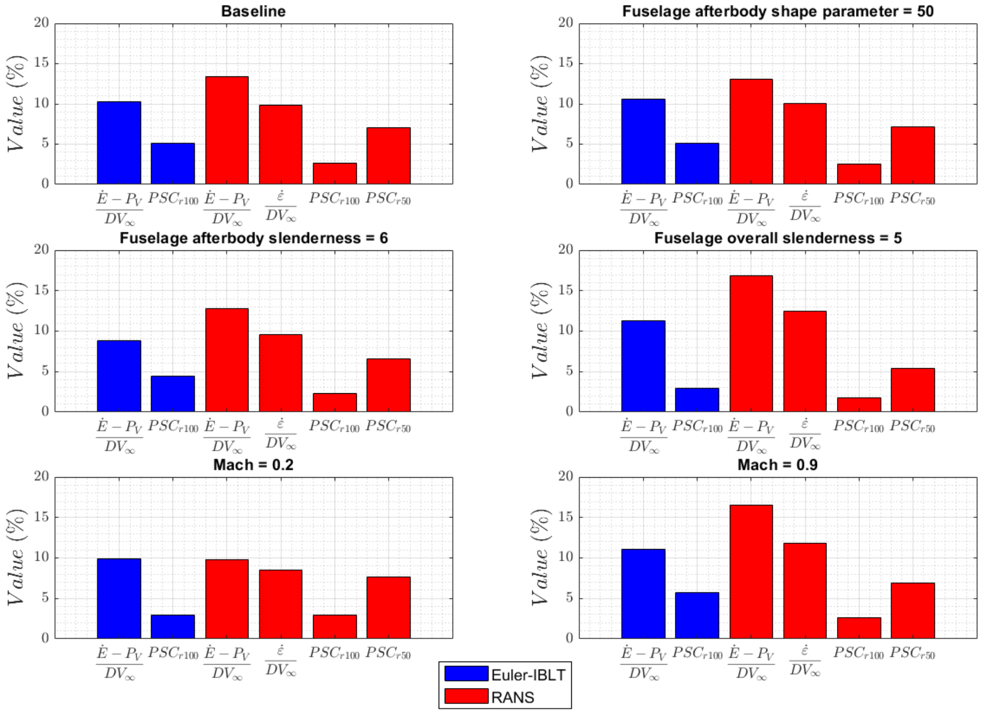

Figure 4.34: Comparison of PSC results from Euler-IBLT and RANS solvers.

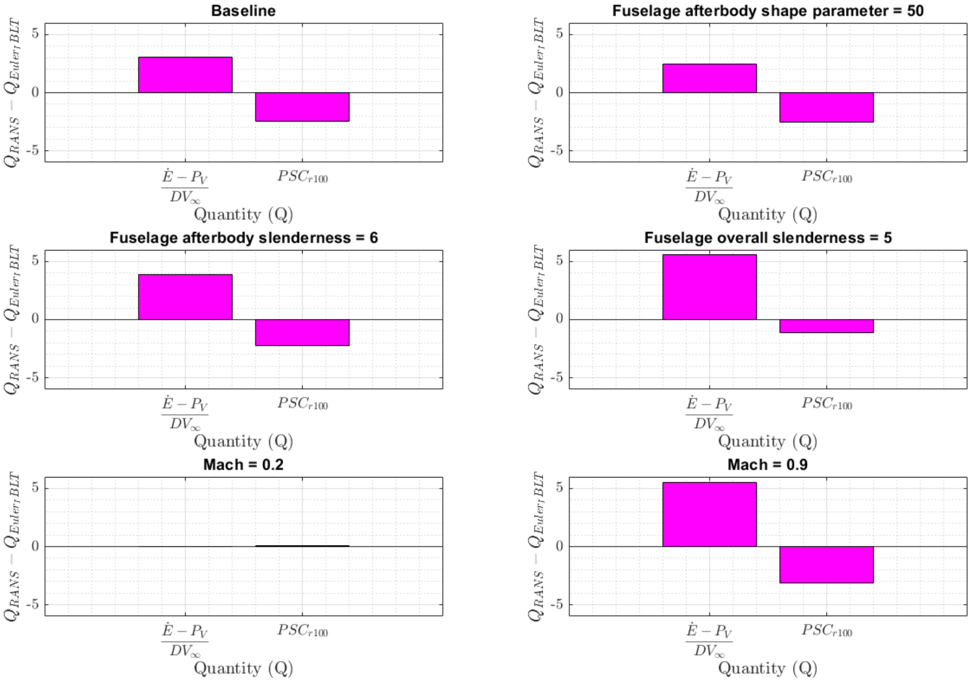

Figure 4.35: Differences of PSC results from Euler-IBLT and RANS solvers.

effectively utilizes the BLI benefit as observed from the PSC_{strict} value which is very close to the maximum isolated body exergy flow. The Mach 0.9 and the $\frac{L_{fuselage}}{D_{fuselage}} = 5$ cases have a significant amount of exergy flow in thermal form (as shown in figure 4.37) and thus the propulsor performance deteriorates. On the whole, the respective PSC values are not very different for the different cases. $\frac{L_{fuselage}}{D_{fuselage}} = 5$ is an outlier to this as laminar flow contributes to a major portion of the available boundary layer exergy (as the fuselage is short). The Mach 0.9 case also has higher exergy flow (at fuselage TE). Finally, the fuselage surface anergy (upstream) is not changed by adding propulsors (meaning the static pressure differences caused do not affect the fuselage surface dissipation and surface anergy rate).

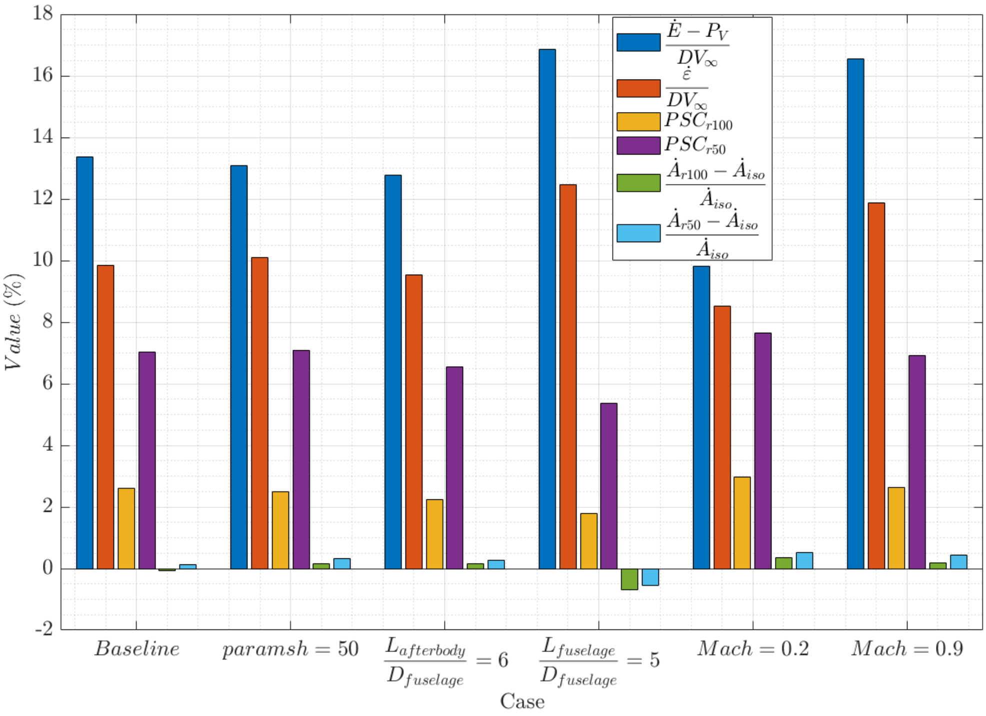

Figure 4.36: Summary of PSC and Surface anergy rate change results (RANS).

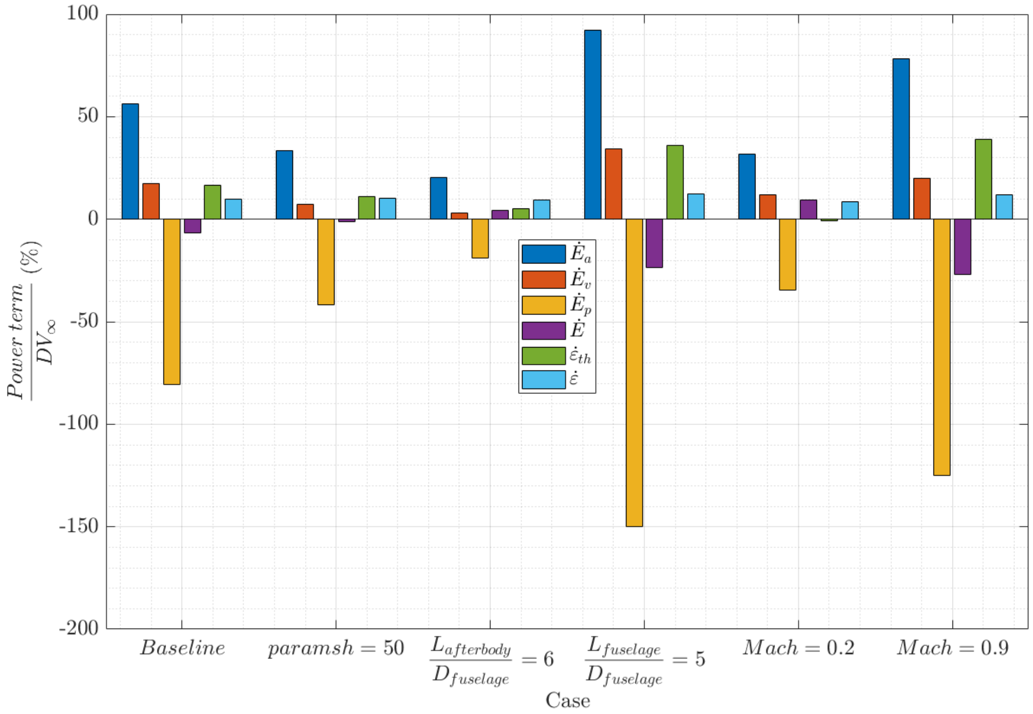

Figure 4.37: Exergy flow splitting (at fuselage TE) for different cases (RANS).

5

OPTIMIZATION STUDY

The vast knowledge gained from different literature and from the Design space exploration studies gives sufficient understanding to perform a general optimization of the fuselage geometry for unducted propulsors. The limitations of the Euler-IBLT solver have been highlighted in section 4.8. It is clear that for a comparison of fuselage geometries (with or without propulsor) at different flight conditions, the Euler-IBLT solver is still a good choice. The efficiency in terms of computational time of the Euler-IBLT solver makes it an ideal choice for the optimization study.

In this chapter optimization studies would be performed with a special focus on the fuselage afterbody geometry. The studies will be performed for both isolated and BLI configurations. Since it has already been recognized that the Euler-IBLT solver has certain limitations when considering the propulsor size, appropriate measures will be taken to arrive at the best configuration for boundary layer application. The optimized geometries will be used for further analysis (like exergy analysis). As such it is otherwise quite clear from the previous chapter that for the qualitative comparison of different isolated fuselage geometries, surface dissipation and anergy rate are not very different in the design space tested. Thus, the isolated body dissipation analysis using the Euler-IBLT solver is already expected to correctly identify the best fuselage geometry.

5.1. FUSELAGE PARAMETERIZATION

The simplistic parameterization as done previously is extended by adding more detail to the afterbody to achieve better control. To do this, different methods can again be used. For example, the entire afterbody could be parameterized using a CST [43] formulation. Another method could be to split the afterbody into different pieces with parameterization for each part. The later is more comfortable due to its simplistic yet powerful nature. The inspiration for parameterization can be obtained from the existing BLI tube fuselage configurations like the PFC as described in [22] or the STARC-ABL concept aircraft by NASA. The work by Pettruson [18] also contains several shapes generated using CST parameterization. These geometries (for fuselage afterbody) can be effectively extrapolated to be constructed of three main parts consisting of a leading section, a cylindrical mid-body, and an exit section. This is shown in figure 5.1. This parameterization is quite similar to the core of the engine design for the D8-Double bubble concept aircraft by MIT as described in [28] with the front hub modified into a leading section which merges with the fuselage tube. The parameterization is also comfortable to give rough arguments regarding the placement of novel engine components. For example, an electric motor (for an electric propeller) and cooling systems could be placed in the cylindrical section similar to the descriptions in [28].

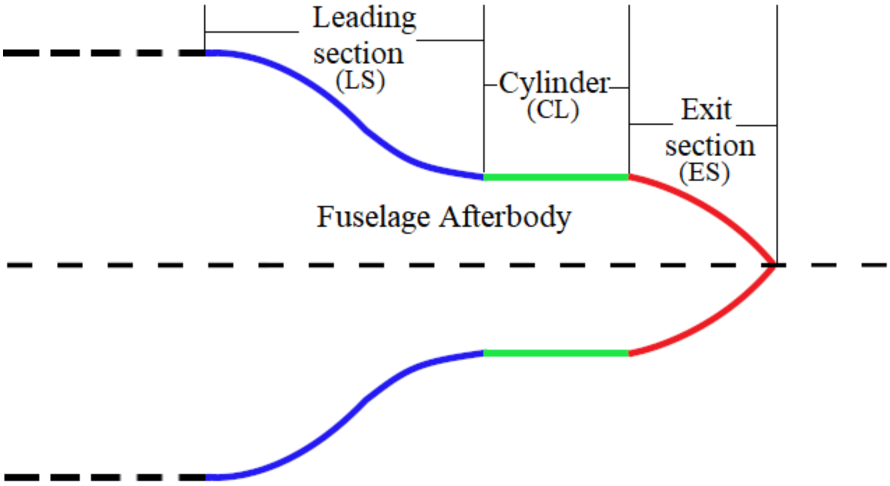

Figure 5.1: Three-curve parameterization for fuselage afterbody.

5.2. PROBLEM DEFINITION

The attempt to optimize the fuselage geometry for the novel application can be done in two ways using the Euler-IBLT solver:

1. Isolated body surface dissipation analysis

2. BLI configuration propulsor power (or net force) analysis

To start with, constraints and bounds would have to be decided upon. For this, important fuselage parameters like the volume and the floor area would be included. Since the main concern of the present thesis is to analyze the performance of fuselage for BLI, the architectural details within the fuselage will not be considered. Also, the exact details of the propulsor like the arrangement of its components are out of scope.

For the study, certain simple assumptions are made regarding the volume and floor area details of the fuselage. These are mentioned in figure 5.2. The floor area of the front section and the volume of the remaining fuselage afterbody are maintained constant during the optimization. This firstly would prevent too much change in fuselage weight (structural weight analysis is not done). Also, the front section can have the last few seat rows and the other stuff for which floor area is important. The bottom volume of the front section may not be a very comfortable location for cargo and thus only the floor area of the front section is considered. Further, the cylinder and the exit section need to contain the engine parts and other systems (like cooling) similar to the details in [28]. Since the configuration is novel and a clear description of the engine type etc. are not considered, the volume of the cylinder and the exit section is important. Even extra fuel may be stored in these parts of the afterbody if necessary. For example, the engine considered in the work by Isikveren et al. [22], the considered engine is a gas turbine engine and on the other hand, the D8 transport has been studied with electric propulsors [10, 28]. Thus, with room for these vast differences, the constraints have been considered.

5.2.1. ISOLATED FUSELAGE PROBLEM

As already mentioned in section 4.8, isolated body surface dissipation is a good indicator when comparing the performance of different fuselages even if a BLI configuration is to be constructed. Thus, a dissipation minimization problem can be formulated to handle the performance optimization. To do this, the above constraints are used and the following problem can be defined:

$$\begin{aligned}
&\min_{X} && \frac{\Phi_{fuselage}}{\Phi_{ref}}\\
&s.t. && \frac{AR_{LS}-AR_{ref}}{AR_{ref}}=0\\
& && 0.7\le\frac{L_{afterbody}}{L_{afterbody_{ref}}}\le 1.2\\
& && 0.8\le\frac{L_{LS}}{L_{LSref}}\le 1.1\\
& && 0.7\le\frac{L_{CL}}{L_{CLref}}\le 1.2\\
& && 0.08\le\frac{paramsh_{LS}}{paramsh_{LS_{ref}}}\le 10\\
& && 0.08\le\frac{paramsh_{ES}}{paramsh_{ES_{ref}}}\le 10
\end{aligned}\tag{5.1}$$

The design vector is given by:

$$\left[\frac{L_{afterbody}}{L_{afterbody_{ref}}},\frac{L_{LS}}{L_{LSref}},\frac{L_{CL}}{L_{CLref}},\frac{paramsh_{LS}}{paramsh_{LS_{ref}}},\frac{paramsh_{ES}}{paramsh_{ES_{ref}}}\right]\tag{5.2}$$

It should be observed that the radius of the cylinder is not required as a design variable because the volume of the exit section (calculated using the formula from the ESDU document [17] as repeated in appendix B.2) and the cylinder are readily known and are used to remove one design variable. The bounds have been carefully determined so that the solver is able to handle the slope changes and curvatures in the geometries (which is essential for successful convergence and physically meaningful results). For example, the solver is found to give physically incorrect swirl (resulting in incorrect surface dissipation) if the afterbody is too short and blunt (which can cause flow separation or significant flow unsteadiness).

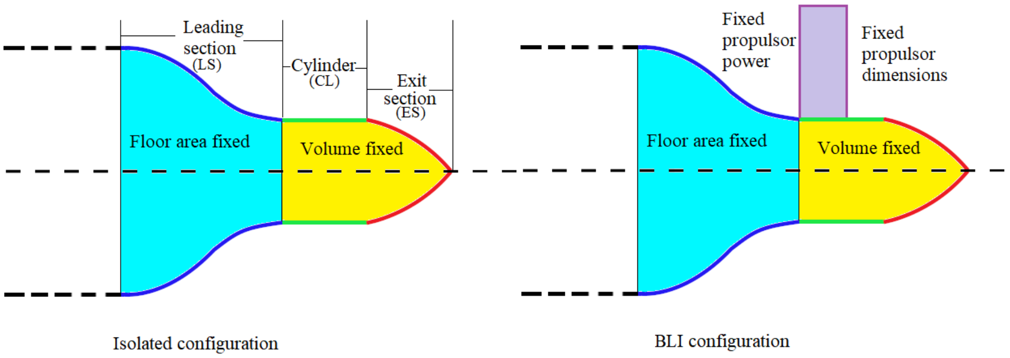

Figure 5.2: Constraints on the fuselage configurations for the optimization studies.

5.2.2. BLI CONFIGURATION PROBLEM

To verify the results from the isolated body optimization it is good to perform an optimization using a BLI configuration as well. Again the constraints are given in figure 5.2. It should be noted that the propulsor size in the Euler-IBLT solver must be carefully selected due to the limitation described in appendix A.2. Thus, it was found that the propulsor size with section areas equal to that of r_{125} (radius 25% higher than the fuselage radius) propulsor at fuselage TE is a good and a safe choice. The r_{100} propulsor equivalent clearly displayed issues while finding the cruise power using a zero search (to get zero net force) for an initial geometry.

It should be further noted that the Euler-IBLT solver is much slower when solving with a propulsor model as the enthalpy equation is also activated as described in [21]. Thus, to perform a zero search for every function call during the optimization would increase the number of function calls by approximately 4 to 5 times.

This clearly is not very good and a zero search to achieve cruise is avoided completely. A much better alternative would be to fix the engine power and perform a net force maximization. This would just require approximately the same number of function calls as that in the isolated body case. Thus, the problem can be defined as follows:

$$\begin{aligned}
\underset{X}{min} \quad & -C_{F_x}+1 \\
s.t. \quad & \frac{AR_{LS}-AR_{ref}}{AR_{ref}}=0 \\
& 0.7 \le \frac{L_{afterbody}}{L_{afterbody_{ref}}} \le 1.2 \\
& 0.8 \le \frac{L_{LS}}{L_{LSref}} \le 1.1 \\
& 0.7 \le \frac{L_{CL}}{L_{CLref}} \le 1.2 \\
& 0.08 \le \frac{paramsh_{LS}}{paramsh_{LS_{ref}}} \le 10 \\
& 0.08 \le \frac{paramsh_{ES}}{paramsh_{ES_{ref}}} \le 10 \\
& 0 \le \frac{x_{ple}}{L_{CL}} \le 1
\end{aligned} \tag{5.3}$$

The design vector is given by:

$$\left[\frac{L_{afterbody}}{L_{afterbody_{ref}}}, \frac{L_{LS}}{L_{LSref}}, \frac{L_{CL}}{L_{CLref}}, \frac{paramsh_{LS}}{paramsh_{LS_{ref}}}, \frac{paramsh_{ES}}{paramsh_{ES_{ref}}}, \frac{x_{ple}}{L_{CL}}\right] \tag{5.4}$$

The objective $-C_{F_x}+1$ was defined with an added constant of 1 to allow an easy tracking of minimization starting from unity (if the initial C_{F_x} is close to zero). The last bound specified in 5.3 is for the position of the propulsor on the cylinder of the afterbody. This completes the definition of the optimization problems.

5.3. OPTIMIZATION METHOD

Optimization in aerodynamics has already been quite well addressed in the literature. Aerodynamic shape optimization (ASO) was first practically used by Hicks et al. [49] to design two-dimensional transonic airfoils. Hicks and Henne [50] further used gradient-based ASO for a 3D transonic wing. It should be noted that the subject of optimization is vast with various methods and algorithms. They can be in general divided into gradient-based and non-gradient-based methods [51]. Each method has its own pros and cons. For the case of gradient-based methods, a gradient calculation method called Adjoint method is available first introduced by Pironneau [52] and later developed by Jameson [53] for aerodynamic shape optimization. Adjoint shape optimization is more useful when the number of design variables is high and function evaluations are costly. Wolpert and Macready [54] state that no optimization algorithm is the best for all problems and any optimization algorithm gives an average performance if tested over a set of problems. This is called the No Free Lunch Theorem for optimization. But it should be noted that the requirement for any optimization varies and the pros and cons of any optimization algorithm could be predicted for a given type of problem. Skinner and Zare-Behtash [51] give a performance review of the most common optimization architectures and algorithms used in ASO by analyzing a total of 229 published papers in more than 120 journals and conference proceedings. It can be found from [51] that a multi-start gradient-based algorithm performs well in an overall sense for ASO problems.

The fmincon function of MATLAB with Sequential quadratic programming (SQP) algorithm is used for the optimization (gradient based) study. Different start points are used wherever necessary to gain more confidence regarding the global nature of the obtained optimum.

The optimization for the isolated body is performed with three different start points to gain some confidence regarding the global nature of the obtained optimum in the design space. Whereas for the BLI case, different propulsor powers (constant during optimizations) are used to achieve different start points. This also allows one to compensate for the fact that the usable size of the propulsor is limited in the Euler-IBLT solver. It should be noted that a higher propulsor power (implying higher thrust) than the amount required for cruise can be useful to imitate the pressure ratios of smaller propulsors during cruise (which cannot be modeled in MTFLOW otherwise).

For the optimization, an exaggerated geometry would be used as the first baseline (Base-1) as shown in figure 5.3. The reason for this would be clear from the result of the optimization study which is the fact that minor changes in the afterbody geometry while maintaining the floor area and volume, constant as shown in figure 5.2, do not produce much effect on the surface dissipation. Thus, an exaggerated geometry (which is not very good aerodynamically) had to be defined in order to run the optimization with noticeable changes to the initial geometry to achieve an optimum.

5.4. OPTIMIZATION RESULTS

This section discusses the main details and results of the optimization studies. Two optimization studies are performed:

- Isolated fuselage surface dissipation minimization (for zero net force).
- BLI configuration force maximization (fixed power).

The isolated dissipation minimization is expected to generate a fuselage geometry which requires the least power consumption for cruise if an ideal propulsor is used to extract the complete wake power. On the other hand, the net force maximization of BLI configuration is expected to generate a fuselage geometry which requires the least power for cruise (and for some other propulsor pressure ratios which are tried).

5.4.1. ISOLATED BODY DISSIPATION MINIMIZATION

The minimization of the fuselage surface dissipation as defined in subsection 5.2.1 is performed using three different start points (that is with different initial design variable values). The optimization results are summarized in table 5.1 for the different start points. The geometries are plotted in figure 5.3.

Objective $\left(\frac{\Phi_{fuselage}}{\Phi_{ref}}\right)$ improvement (%)	Time for optimization (sec)	Number of iterations
$X_0 = [1, 0.2, 0.1, 1, 1]$ $X_{optim} = [0.7003, 0.3202, 0.1073, 0.9647, 1.0097]$		
2.30	1234.19	9
$X_0 = [0.85, 3.5, 0.1, 1.05, 0.7]$ $X_{optim} = [0.7053, 3.2687, 0.5139, 0.9909, 0.7343]$		
2.46	1249.87	11
$X_0 = [0.7, 10, 0.08, 1.019, 1.2]$ $X_{optim} = [0.7000, 10.0000, 0.1345, 1.0145, 1.1586]$		
2.35	340.64	2

Table 5.1: Results of isolated fuselage surface dissipation minimization using Euler-IBLT solver.

It is observed that different start points indeed produce different design vectors but all of those lead to the same fuselage geometry in different ways as can be observed in figure 5.3. The optimized fuselage looks more like a conventional tube wing aircraft fuselage with minor adjustments for attaching the BLI parts. This suggests that the for the specified constraints, the optimized fuselage for BLI application may not be very different from a conventional fuselage in terms of surface dissipation.

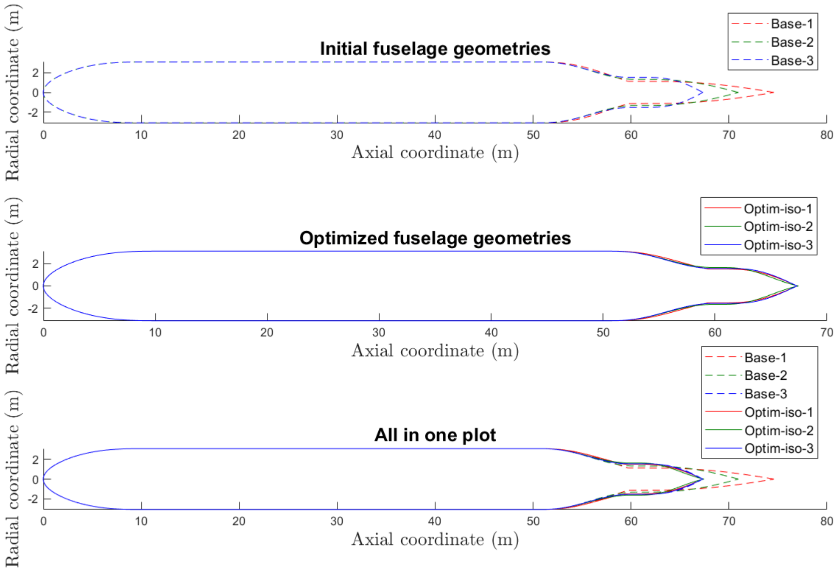

Figure 5.3: Results of isolated fuselage surface dissipation minimization using Euler-IBLT solver.

5.4.2. BLI CONFIGURATION NET FORCE MAXIMIZATION

The maximization of the net force of the BLI configuration is done by using different values of the initial net force in three different optimizations. The different values of net force allow the exploration of the interaction effect of the exhaust plume and the fuselage which may have a deteriorating effect as noticed in section 4.6. The results of the optimization are presented in table 5.2. The optimized fuselage geometries are shown in figure 5.4.

<table>
<tr><th>Initial net force ($\frac{F_{xcase}}{D_{Base-1}}$)</th><th>Force count increase ($\Delta C_{F_x} \times 10^4$)</th><th>Time for optimization (sec)</th><th>Number of iterations</th></tr>
<tr><td colspan="4">$X_0 = [1, 0.2, 0.1, 1, 1, 0]$
$X_{optim} = [0.7021, 0.7329, 0.1353, 0.9849, 1.0000, 0.0000]$</td></tr>
<tr><td>0</td><td>13.55</td><td>5854.94</td><td>7</td></tr>
<tr><td colspan="4">$X_0 = [1, 0.2, 0.1, 1, 1, 1]$
$X_{optim} = [0.7028, 0.8814, 0.1752, 0.9891, 1.1380, 1.0000]$</td></tr>
<tr><td>1</td><td>14.22</td><td>6227.07</td><td>10</td></tr>
<tr><td colspan="4">$X_0 = [1, 0.2, 0.1, 1, 1, 0]$
$X_{optim} = [0.7000, 0.0800, 0.3424, 0.9224, 1.0000, 0.0000]$</td></tr>
<tr><td>2</td><td>11.54</td><td>3579.89</td><td>5</td></tr>
</table>

Table 5.2: Results of BLI configuration net force maximization using Euler-IBLT solver.

The results of optimization clearly produce very close geometries for the different net force values. Also, the optimized fuselage geometry for the BLI configuration matches with the optimized isolated fuselage geometry confirming the fact that an isolated body analysis sufficiently covers the required details even for a BLI application. The minor differences in the net force counts as observed in table 5.2 are due to the specified optimization tolerances which were chosen so as not to stress the optimizer too much for minor differences in results. Another important aspect to note is that the propulsor position on the cylinder (of afterbody) does not cause much of a difference on the optimized fuselage as the cylinder itself becomes short. For example, for the second optimization run the propulsor was initially chosen to be on the aft of the cylinder as can be

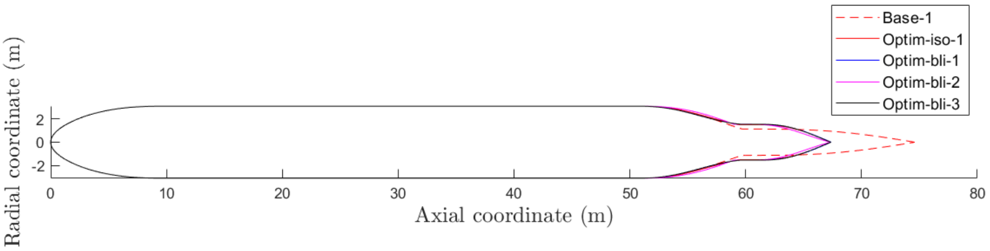

Figure 5.4: Results of BLI configuration net force maximization using Euler-IBLT solver.

noticed from the design vector values specified in table 5.2 and for the other runs it (the leading plane of propulsor) was specified to be located at the start of the cylinder. This position value was not changed by the optimizer for any case (though the power/net force difference is noticeable if the position is changed on the baseline fuselage (Base-1 geometry as in figure 5.3)).

5.5. RANS SIMULATIONS

It is again convincing to verify the important results using a RANS analysis. This section focuses on analyzing the baseline (Base-1 geometry as in figure 5.3) and the optimized fuselage, as usual, using an isolated body analysis and a BLI analysis with at least two different propulsors (r125 and r50 are selected this time). Only cruise will be studied in RANS as it is the most relevant flight phase as far as the power consumption is concerned.

The results of the RANS simulation including several important quantities like the PSC_{ideal} and PSC_{strict} are mentioned in table 5.3 along with the important values from the Euler-IBLT solver.

Quantity	Base-1	Optim-iso-1	Difference
RANS			
C_D	0.069233	0.068476	-1.09 %
$C_{\Phi S}$	0.030161	0.029495	-2.21 %
$C_{\dot{A}S}$	0.030575	0.029917	-2.15 %
$\left(\frac{\dot{E}-P_V}{DV_\infty}\right)_{TE}$ (%)	12.87	13.85	0.98
$\left(\frac{\Phi}{DV_\infty}\right)_{TE}$ (%)	87.13	86.14	-0.98
$\left(\frac{\dot{\varepsilon}}{DV_\infty}\right)_{TE}$ (%)	11.67	12.62	0.95
$\left(\frac{\dot{A}}{DV_\infty}\right)_{TE}$ (%)	88.33	87.38	-0.95
Euler-IBLT			
C_D	0.072461	0.071191	-1.75 %
$C_{\Phi S}$	0.03279	0.032038	-2.30 %
$\left(\frac{\dot{E}-P_V}{DV_\infty}\right)_{TE}$ (%)	9.50	10.00	0.5
$\left(\frac{\Phi}{DV_\infty}\right)_{TE}$ (%)	90.50	90.00	-0.5

Table 5.3: Isolated body simulation (RANS) results of the baseline and optimized geometry. $F_x = D$.

The RANS surface dissipation result is quite comparable to the Euler-IBLT result (when comparing the difference of the value of the optimum geometry from that of the baseline geometry). The PSC_{ideal} on the other hand are a bit different and, as usual, the Euler-IBLT solver over predicts the dissipation (this time the resulting wake power is a bit off even from the exergy based PSC_{strict}). This problem with PSC_{ideal} is that it does not really show a clear pattern apart from being over-predicted which can be due to the way in which certain terms in the integral boundary layer equations are modeled in the Euler-IBLT solver.

The RANS results with the propulsors attached are given in table 5.4. All results are quite as expected based on the DSE. The smaller propulsor shows better performance (as expected) as it is able to use more from the boundary layer due to higher pressure ratio created by it for cruising.

Quantity	Base-1	Optim-iso-1	Difference
$\frac{D_{propulsor}}{D_{fuselage}} = 1.25$ (RANS)			
C_D	0.078613	0.074840	-4.80 %
C_P	0.034136	0.033784	-1.03 %
$PSC_{strict}(\%)$	1.39	1.34	-0.06
$\frac{D_{propulsor}}{D_{fuselage}} = 0.5$ (RANS)			
C_D	0.090394	0.082393	-8.85 %
C_P	0.032756	0.032335	-1.28 %
$PSC_{strict}(\%)$	5.37	5.56	0.18
$\frac{D_{propulsor}}{D_{fuselage}} = 1.25$ (Euler-IBLT)			
C_P	0.035129	0.034465	-1.93 %
$PSC_{strict}(\%)$	3.14	3.28	0.14

Table 5.4: BLI configuration simulation (RANS) results of the baseline and optimized geometry. $F_x = 0$.

6

OBSERVATIONS, CONCLUSIONS AND RECOMMENDATIONS

Starting with the discussion on the application of power balance and exergy analysis to a CFD framework followed by a design space exploration and an optimization of tube fuselage geometry for boundary layer application have been covered in the previous chapters. The important observations from the results obtained and discussed in previous chapters are mentioned again in the present chapter. This is followed by conclusions and recommendations for future work.

6.1. OBSERVATIONS

The observations worth mentioning during the application of Power balance and exergy analysis methods to different geometries in a CFD framework include:

- The application of the power balance or the exergy analysis in a CFD framework needs to be done carefully. Energy/Power conservation in each cell during a CFD simulation does not necessarily guarantee that the power balance or exergy analysis integrals are free from error build up as observed in subsection 3.1.1 while analyzing the F_x formula (can be observed in figure 3.9).
- The nature of the flow plays an important role in determining the power benefit (in terms of PSC) for BLI/WI. Laminar flow gives a much higher power saving than turbulent flow as observed in figure 3.22 (for flow over flat plate). Thus, the percentage of laminar or turbulent flow over a body is an important factor to consider for maximizing the benefit of BLI/WI.
- Compressible flows can be better understood with an exergy analysis rather than a power balance analysis. However, power balance analysis still proved to be satisfactory qualitatively as seen later during design space and optimization studies.
- The absolute values of drag, power balance and exergy analysis related quantities are a bit different between the Euler-IBLT and RANS solvers. This can mostly be attributed to the difference in the flow modeling. The exact percentages are shown for two cases in tables 3.7 (NACA0040 BOR) and 3.11 (tube fuselage geometry).

Next the design space exploration studies result in the following set of observations:

- The fuselage surface dissipation (Euler-IBLT or RANS) and surface anergy rate (RANS) of the isolated body gives a good indication of the fuselage performance at different flight conditions. The surface anergy rate is the minimum amount of power that needs to be supplied by an ideal propulsor to propel the fuselage (for zero net force).
- The fuselage surface dissipation (Euler-IBLT or RANS) and surface Anergy rate (RANS) upstream of a propulsor in a BLI configuration is not different from the respective values till the same location for the isolated fuselage for the wide range of designs (and flight speeds) considered.

- The power saving coefficients (PSC_{ideal} and PSC_{strict}) are not very different when compared between different fuselage designs (or flight conditions) except for certain cases like short fuselages (low slenderness) in which the percentage of laminar and turbulent flow over the body become comparable. Mach number variations also give some exceptions. Some important results can be observed from the figure 4.36.
- The minor changes (≈ 3%) in power saving coefficients (PSC_{ideal} and PSC_{strict}) which is observed in some cases (like for Mach = 0.9 and $\frac{L_{fuselage}}{D_{fuselage}} = 5$) is accompanied by large changes (≈ 45%) in power quantities like surface dissipation, surface anergy rate, or propulsor power. Thus, the effect on BLI itself is not very high for variations in fuselage geometries (and flight conditions).
- The ideal power saving coefficient ($\frac{\dot{E}-P_V}{DV_\infty}$) from the Euler-IBLT solver is under-predicted in most cases when compared to the results from the RANS solver (except at low Mach). This can be observed in figure 4.34. However, it should also be noted that for the NACA0040 BOR (which is analyzed at a low Mach), the under-prediction is seen again. Thus, no definite pattern can be determined. This under-prediction can as such be due to the difference in flow modeling. The differences in capturing of thermal effects and turbulence all together could be responsible for the difference in results between the solvers. Also, the PSC values are anyways of lesser importance than the surface dissipation (or surface anergy rate) and absolute power consumption when comparing the performance of different fuselage designs (or flight conditions).
- The fuselage surface dissipation (isolated body analysis) and propulsor power consumption (BLI configuration) results from the Euler-IBLT solver display close match with the respective values (and surface anergy rate) from the RANS solver when the values are compared with a baseline (in the respective solvers). This can be observed from the figure 4.32.
- Also, the design space studies show that for qualitative comparison of fuselage designs (or flight conditions), the isolated body drag is also a good performance parameter as it gives qualitatively a similar behavior to surface dissipation (at least for the considered design space which covers a wide range of designs and flight conditions). The minor variations in PSC values as compared to the large variations in the power quantities for fuselage design changes (or flight condition changes) can be used to explain this point.
- If the propulsor is attached before the fuselage TE, the exhaust plume may interact with the fuselage surface downstream and cause an additional dissipation as observed in figure 4.26. However, as such propulsor must be placed as close to trailing edge as possible for maximum benefit anyways (it should be noted that no additional aerodynamic interaction due to bodies like nacelle is considered in this argument).

Finally, observations form the optimization study are stated below:

- The isolated body and BLI configuration simulations both result in the same optimum fuselage geometry for the given constraints.
- The optimization results in a small improvement as seen in section 5.4. It should be noted that the baseline geometry used for optimization is already a bit exaggerated when compared to conventional transport aircraft (due to stretching of the fuselage afterbody).

6.2. CONCLUSIONS

The current project involved the aero-propulsive performance analysis of aircraft fuselage designs for Boundary layer ingestion (BLI). Design space exploration was carried out to analyze the performance of different fuselage designs (and flight conditions). Euler-IBLT solver (dissipation analysis of isolated fuselage and propulsor power analysis of BLI configuration) was used for the explorations and important results were further verified using RANS simulations (dissipation and anergy rate analysis of isolated fuselage and propulsor power analysis of BLI configuration). The isolated body simulation results indicated the same qualitative fuselage performance as BLI configuration simulations. The anergy rate (or viscous dissipation) upstream of the propulsor does not change as compared to that of the isolated fuselage (calculated till the same location in both cases). Also, the PSC_{ideal} and PSC_{strict} were not very sensitive to the fuselage designs or flight conditions (at least for the design space considered which sufficiently covers a wide range) except for minor changes for some cases. For the isolated body analysis, the fuselage surface dissipation variation is not different from that of the fuselage drag qualitatively. The optimization study also gives the same optimum for both isolated body and BLI configuration analysis for the specified constraints. From these observations, it is clear that even for a BLI configuration (tube fuselage with propulsor at aft), fuselage with lesser surface area would require lesser power for transport aircraft and the benefit due to BLI itself will not be affected much for different fuselage designs and flight conditions (at least for unducted propulsors).

To wrap up, the following points can be stated:

- The effect of fuselage design (and flight conditions) on BLI itself is much lower when compared to the effect on drag power. Thus, fuselage performance for BLI configurations are comparable on a qualitative basis using the isolated body drag value itself.
- The surface dissipation is a more informative parameter for fuselage performance comparison. However, the surface anergy rate is the most appropriate (especially for transonic flights) to quantify the exact possible benefit when using a fuselage design (or flight condition) as it handles the thermal effects more neatly than the surface dissipation as explained in section 2.4.
- Qualitatively, the variation in the surface dissipation and surface anergy rate (unchanging value between isolated and BLI configuration) matches that of the propulsor power consumption in BLI configuration for different fuselage designs (and flight conditions).
- The typical conventional fuselage afterbody geometry with necessary modifications for the BLI engine attachment should already give a good performance and no special aerodynamic modifications are necessary for BLI in specific.

The research goals and sub-goals formulated at the beginning of the thesis can be analyzed to verify to what extant they have been achieved. The following points can be stated:

- The power balance method and exergy analysis methods have been carefully understood and their successful application in different CFD problems can be observed in different parts of the thesis. The important errors when applying the methods to a CFD framework were also identified.
- Design space explorations and optimization studies were carried out using the Euler-IBLT solver (with power balance method) to study different fuselage designs (and flight conditions). Important results were verified using RANS simulations (with power balance and exergy analysis methods).
- The inclusion of a propulsor nacelle and swirl would have been better and these constitute the immediate goals for a future study.

6.3. RECOMMENDATIONS FOR FUTURE WORK

Results of the present study, give more clarity regarding fuselage design for BLI configurations. Some details like the unchanging value (between isolated fuselage and BLI configuration) of fuselage surface dissipation (upstream of fuselage) as hinted in [6] is verified for a wide range of fuselage designs and flight conditions. Also, the fuselage surface anergy rate (which is theoretically better if considered) is also verified to show the same unchanging behavior like the surface dissipation. The dependability on isolated body analysis for qualitative for comparison of fuselage performance is confirmed for transport aircraft for a wide range of designs (at least for unducted propulsors configurations). These analyses especially are important and implicitly lead to the different conclusions in the thesis. Thus, future studies can use these studies when changing different aspects of the analysis. The following points could be beneficial for the future:

- Ducted propulsor configurations could be considered and the surface dissipation and anergy rate behavior could be studied.
- Effect of swirl also needs to be considered depending on the type of propulsor to be used for the BLI application. Also, the use of swirl recovery vanes for BLI propulsors could be an interesting option. Some details of swirl recovery vanes applied to an isolated and wing-mounted freestream ingesting propulsors can also be found in [37].

- The design of propulsor is indeed the next important step. One example of such an attempt can be found in [37] in which the rotor blade is optimized for BLI application.
- Further, a multi-disciplinary analysis of the fuselage in which the propulsion cycles and the fuselage structure and weight are also given importance could be performed.
- It should be noted that the present study only considers axisymmetric fuselage geometries. Thus three-dimensional simulations which include the effect of flow distortion on propulsor performance are also required. An example of the inclusion of the inlet flow distortion can be found in [16]. Also, a full three-dimensional analysis allows the consideration of the takeoff afterbody ground clearance.
- Finally, the effect of wing and empennage also become important.

A

BOUNDARY LAYERS

A.1. BOUNDARY LAYER DEFINITIONS

Some important definitions used in the Integral boundary layer theory are mentioned next.

Mass defect [1]:

$$\rho_e u_e \delta^* = \int_0^{y_e} (\rho_e u_e - \rho u).dy_n \tag{A.1}$$

Momentum defect [1]:

$$\rho_e u_e^2 \theta = \int_0^{y_e} (u_e - u)\rho u.dy_n \tag{A.2}$$

Kinetic energy defect [1]:

$$\rho_e u_e^3 \theta^* = \int_0^{y_e} (u_e^2 - u^2)\rho u.dy_n \tag{A.3}$$

Density defect [1]:

$$\rho_e u_e \delta^{**} = \int_0^{y_e} (\rho_e - \rho) u.dy_n \tag{A.4}$$

Wake kinetic energy excess [1]:

$$\rho_e u_e^3 (2\theta - \theta^*) = \int_0^{y_e} (u_e - u)^2 \rho u.dy_n \tag{A.5}$$

Kinematic shape parameter [20]:

$$H_k = \int_0^{y_e} \frac{\left(1 - \frac{u}{u_e}\right).dy_n}{\left(1 - \frac{u}{u_e}\right)\frac{u}{u_e}.dy_n} \tag{A.6}$$

A.2. BLI PROPULSOR MODEL IN EULER-IBLT SOLVER

The equations used in the Euler-IBLT solver to capture the flows with energy addition are mentioned in subsection 2.5.2. It should be noted that to model a propulsor ingesting the boundary layer flow, certain confusions can arise. For example, a propulsor smaller than the local displacement thickness would not result in any thrust production as the propulsors of these sizes do not operate on any flow field. Thus it is very clear that for any flow to exist through the propulsor, it has to be bigger than the displacement thickness. But the results in subsection 4.2.1, clearly show that some issue exists at small propulsor radii (just larger than the displacement thickness). To reason this out it is necessary to consider the nature of the flow model in the Euler-IBLT solver as compared to an actual flow field. To consider this, a simple case of a flat plate boundary layer with a BLI propulsor plane (assuming that it does not cause any changes to the upstream flow field) is used as shown in figure A.1.

The propulsor modeling in MTFLOW is equivalent to adding body forces and the corresponding power to the flow. Since it is already known that the propulsor is ineffective (physically incorrect) if smaller than the

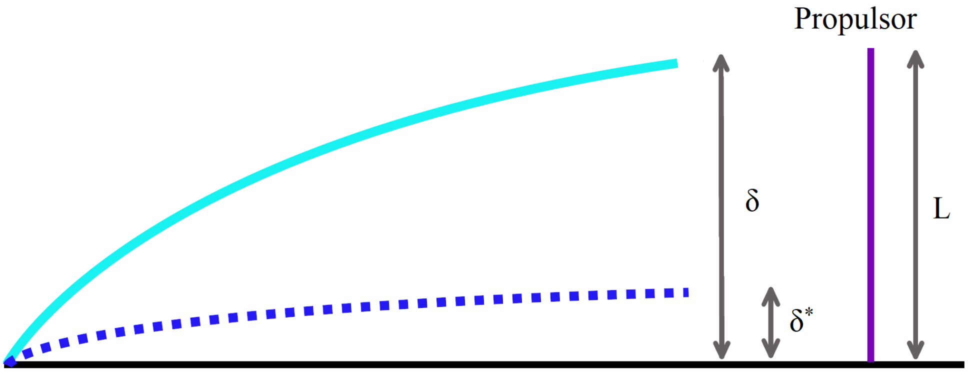

Figure A.1: Boundary layer ingesting propulsor for a flat plate.

displacement thickness and the minimum size of the propulsor required to correctly model a physical flow is necessary before performing BLI simulations in the Euler-IBLT solver. For this, it is possible to consider the mass flow through the propulsor plane (assuming that upstream flow is unaffected) as shown in figure A.1. Starting with the definition of the boundary layer thickness as in [34]:

$$\rho_e u_e \delta^* \ = \rho_e u_e \delta - \int_0^{\delta} \rho u . dy \, . \tag{A.7}$$

Then an equation for the mass flow through the propulsor of size L could be written for the case of Euler-IBLT (EI) and actual (RVF) flows. For the Euler-IBLT (EI) formulation, the following can be written (at least for a flat plate):

$$\dot{m}_{EI} \ = \rho_e u_e (L - \delta^*) \, , \tag{A.8}$$

where it should be noted that by the definition of displacement thickness, the boundary layer edge velocity and edge density should be constant from the displacement thickness onwards (equal to the freestream values for a flat plate without pressure gradient).

For real viscous flows (RVF), a general mass flow equation is (applies for any L):

$$\dot{m}_{RVF} \ = \int_0^{L} \rho u . dy = \int_0^{\delta} \rho u . dy - \int_L^{\delta} \rho u . dy \, , \tag{A.9}$$

Using equation A.7 in equation A.9:

$$\dot{m}_{RVF} \ = \rho_e u_e (\delta - \delta^*) - \int_L^{\delta} \rho u . dy \, , \tag{A.10}$$

For the mass flows in the two cases (EI and RVF) to be equal, the valid relation between L and δ needs to be found:

$$\dot{m}_{EI} \ ? \ \dot{m}_{RVF} \, , \tag{A.11}$$

where '?' is a mathematical relation (like '=') and the expression can be further written based on equations A.8 and A.10:

$$L \ ? \ \delta - \int_L^{\delta} \frac{\rho u}{\rho_e u_e} . dy \, . \tag{A.12}$$

Now if $L \geq \delta$, then $\rho u = \rho_e u_e$ for any L implying:

$$L \ ? \ \delta - (\delta - L)\,, \tag{A.13}$$

which gives:

$$L \ ? \ L\,, \tag{A.14}$$

where the '?' can be replaced with '=' giving:

$$L \ = \ L\,, \tag{A.15}$$

which can be easily traced back to:

$$\dot{m}_{EI} \ = \ \dot{m}_{RVF}\,. \tag{A.16}$$

Thus, if $L \geq \delta$, then $\dot{m}_{EI} = \dot{m}_{RVF}$.
Next, if $L < \delta$, then let:

$$\int_L^\delta \frac{\rho u}{\rho_e u_e} .dy \ = \ (\delta - L)k \tag{A.17}$$

where k is a real number < 1 because $\rho u < \rho_e u_e$ always for a boundary layer. Thus the expression A.12 can be written as:

$$L \ ? \ \delta - (\delta - L)k\,, \tag{A.18}$$

$$L(1-k) \ ? \ \delta(1-k)\,, \tag{A.19}$$

since $k < 1$, $1 - k$ must be positive and $1 - k$ can be canceled safely on both sides without changing the nature of '?':

$$L \ ? \ \delta\,, \tag{A.20}$$

which leads to (according to initial assumption):

$$L \ < \ \delta\,, \tag{A.21}$$

which is traced back to:

$$\dot{m}_{EI} \ < \ \dot{m}_{RVF}\,, \tag{A.22}$$

which is clearly valid if $L < \delta^*$ where $\dot{m}_{EI} = 0$ whereas $\dot{m}_{RVF}$ is finite and positive.

Thus, if $L < \delta$, then $\dot{m}_{EI} \neq \dot{m}_{RVF}$.

Thus, for the flow to be physically correct, the propulsor must be at least bigger than or equal to the boundary layer thickness. The results are bound to be non-physical if the condition $L \geq \delta$ is not satisfied. But determining a boundary layer thickness from the displacement thickness may not be very straightforward and thus a RANS simulation could be performed to obtain the total pressure contour which could be used to determine a minimum safe propulsor size.

Also, it is easy to see that the above can be easily extended to an axisymmetric case by considering the axisymmetric flow over a hypothetical cylindrical of radius r. The mass flow of the EI and RVF can be put in the same expression using '?' as follows:

$$(L+r)^2 \ ? \ (\delta + r)^2 - 2\int_L^\delta \frac{\rho u}{\rho_e u_e} y.dy \tag{A.23}$$

It is again easy to verify the fact that the size of the propulsor plane normal to the boundary layer flow has to be bigger than the local boundary layer thickness for capturing the correct mass flow.

Next, the angle of the boundary layer with respect to the propulsor plane is also an easy consideration. Since the projection of the boundary layer on to the propulsor plane could be considered and the boundary layer thickness is again good to go. Though a smaller size propulsor could be used depending on the projection of the boundary layer thickness on the required plane.

Further, it should be noted that the boundary layer displacement thickness is reduced by the application of a favorable pressure gradient by the propulsor. Thus, a safe propulsor size can be selected based on an isolated body simulation also. Another important aspect is the question of whether a fixed propulsor size is fair to use when the fuselage geometry changes ahead of it produce boundary layers of different displacement thickness. This means that the propulsor intake area is changed when displacement thickness of boundary layer changes in the Euler-IBLT solver. But it should be noted that if the propulsor is bigger than the boundary layer thickness, the mass flow becomes equal to a real flow whatsoever. This means that from a mass flow perspective, the propulsor of a fixed size is the same as that in real flow making is fair irrespective of the local fuselage displacement thickness (unless the propulsor size becomes lesser than the boundary layer thickness).

A.3. BOUNDARY LAYER DISSIPATION BEHAVIOR

The variation of dissipation coefficient with shape factor is an important aspect which can hint at the possible reason as to why the surface dissipation is not noticeably changed by the propulsor static pressure field. This variation is given in figure A.2. The local dissiaption coefficient is found to be a function of importantly three parameters which are the kinematic shape parameter (H_k which depends on the shape factor H and edge Mach number M_e as given in [20]), edge Mach number (M_e), and momentum thickness Reynolds number (Re_θ). Also after a $Re_\theta = 6000$, turbulence is assumed to reach an asymptotic state [55].

From figure A.2, it can be noted that for the case of turbulent flow, above a shape factor value of a little lesser than 1.5 (for higher Re_θ values), the dissipation coefficient increases with the shape factor value and vice versa. At the same time, the pressure gradient (due to the propulsor for example) produces an opposite effect on the edge velocity. Since the total dissipation is given by the following integral:

$$\Phi(x) = \int_0^{x_n} \rho_\infty u_e^3 C_\Phi b dx_n \,, \tag{A.24}$$

the opposite behavior of C_Φ and u_e with respect to each other for changing shape factor, the overall Φ value is less affected (if change in H is less as in the case of propulsor addition). On the other hand this is not very true for the case of laminar flows especially at lower shape factor values (the reason for why different wake fillers had different performance). Also, the C_f does not show such a behavior and there can be an increase in integrated friction force on the body if a propulsor is closely integrated.

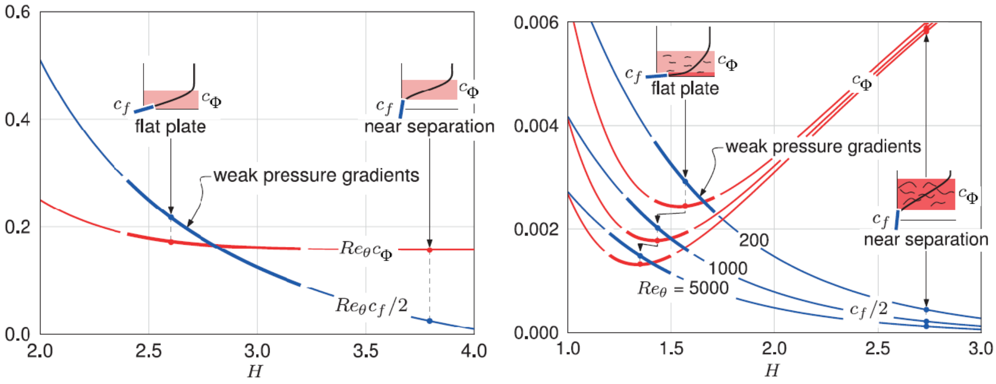

Laminar flow Turbulent flow

Figure A.2: Variation of local dissipation coefficient with boundary layer shape factor. Reproduced from [6].

B

FUSELAGE

B.1. SLENDERNESS VALUES

The different slenderness values used for fuselage geometries throughout the thesis were decided based on typical values for conventional aircraft as mentioned [46]. The table from [46] is repeated in figure B.1.

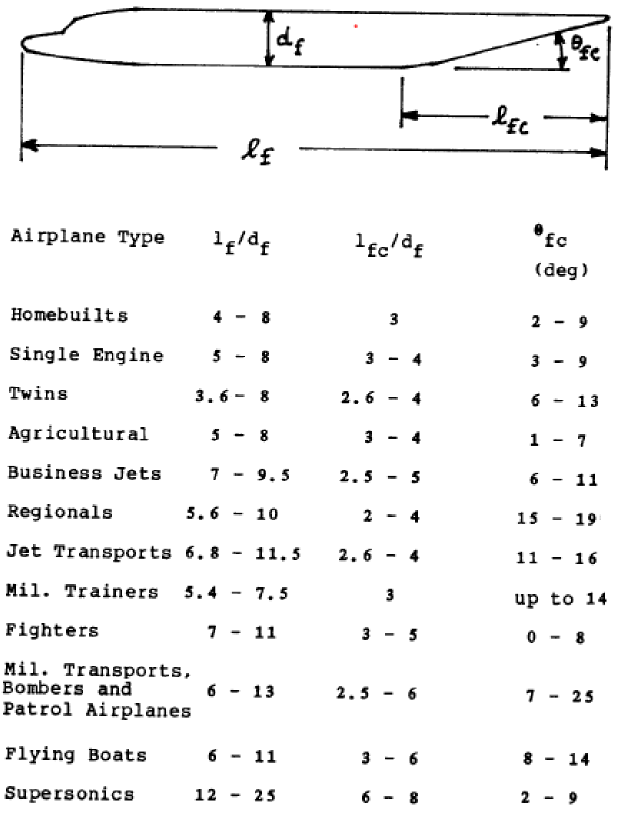

Airplane Type	l_f/d_f	l_{fc}/d_f	θ_{fc} (deg)
Homebuilts	4 - 8	3	2 - 9
Single Engine	5 - 8	3 - 4	3 - 9
Twins	3.6 - 8	2.6 - 4	6 - 13
Agricultural	5 - 8	3 - 4	1 - 7
Business Jets	7 - 9.5	2.5 - 5	6 - 11
Regionals	5.6 - 10	2 - 4	15 - 19
Jet Transports	6.8 - 11.5	2.6 - 4	11 - 16
Mil. Trainers	5.4 - 7.5	3	up to 14
Fighters	7 - 11	3 - 5	0 - 8
Mil. Transports, Bombers and Patrol Airplanes	6 - 13	2.5 - 6	7 - 25
Flying Boats	6 - 11	3 - 6	8 - 14
Supersonics	12 - 25	6 - 8	2 - 9

Figure B.1: Typical slenderness values for aircraft fuselage. Reproduced from [46].

B.2. FUSELAGE ESDU PARAMETERIZATION

The shape of the fuselage Afterbody (and forebody) have been parameterized according to shapes described in [17]. Although different shapes from the classes of Modified Ellipsoid, Myring Cubic, Power Law, and Tangent-Ogive were tried apart from (ESDU II and ESDU I) especially for the afterbody, the results found were very similar and finally only one class of shapes (ESDU II) were used for the *paramsh* studies. It is mentioned here that the Power Law curves (for *paramsh* > 1) produced afterbody geometries with much higher surface dissipation values compared to the other shape classes. These results will not be repeated to save space as they are easily repeatable (and less important) if required. The shapes and the equations are mentioned in figure B.2.

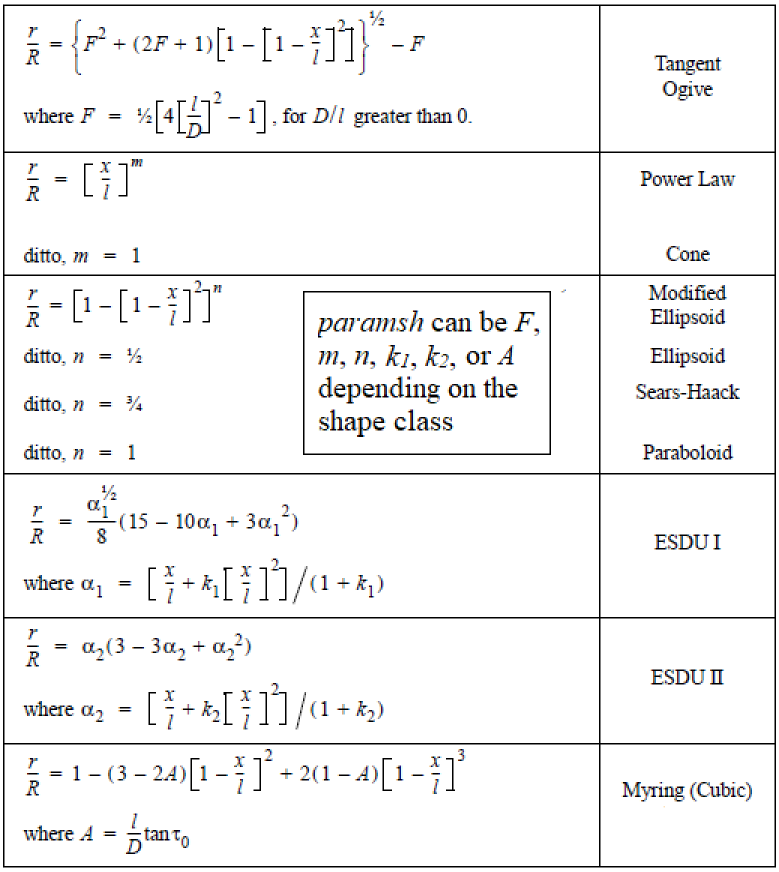

$\frac{r}{R} = \left\{F^2 + (2F+1)\left[1 - \left[1 - \frac{x}{l}\right]^2\right]\right\}^{1/2} - F$	Tangent Ogive
where $F = \frac{1}{2}\left[4\left[\frac{l}{D}\right]^2 - 1\right]$, for D/l greater than 0.	
$\frac{r}{R} = \left[\frac{x}{l}\right]^m$	Power Law
ditto, $m = 1$	Cone
$\frac{r}{R} = \left[1 - \left[1 - \frac{x}{l}\right]^2\right]^n$	Modified Ellipsoid
ditto, $n = \frac{1}{2}$	Ellipsoid
ditto, $n = \frac{3}{4}$	Sears-Haack
ditto, $n = 1$	Paraboloid
$\frac{r}{R} = \frac{\alpha_1^{1/2}}{8}(15 - 10\alpha_1 + 3\alpha_1^2)$ where $\alpha_1 = \left[\frac{x}{l} + k_1\left[\frac{x}{l}\right]^2\right] / (1 + k_1)$	ESDU I
$\frac{r}{R} = \alpha_2(3 - 3\alpha_2 + \alpha_2^2)$ where $\alpha_2 = \left[\frac{x}{l} + k_2\left[\frac{x}{l}\right]^2\right] / (1 + k_2)$	ESDU II
$\frac{r}{R} = 1 - (3 - 2A)\left[1 - \frac{x}{l}\right]^2 + 2(1 - A)\left[1 - \frac{x}{l}\right]^3$ where $A = \frac{l}{D}\tan\tau_0$	Myring (Cubic)

paramsh can be F, m, n, k_1, k_2, or A depending on the shape class

Figure B.2: Typical curve equations for parameterization of axisymmetric fuselage. Reproduced from [17]. Few example diagrams of the shapes can also be found in [17]. Also, for the exact meaning of the symbols, the reader is referred to [17].

Further, the formulas of volume and surface area of the fuselage geometries created by using different shapes can also be found in [17]. The only formula required for the present thesis is the volume of the ESDU II shape class based BOR. The equation is given as:

$$V_{ESDU2BOR} = \left[\frac{1}{12012}\left[\left(\frac{1}{1+k_2}\right)^6 - 19\left(\frac{1}{1+k_2}\right)^5 + 158\left(\frac{1}{1+k_2}\right)^4\right] - \frac{1}{30030}\left[1441\left(\frac{1}{1+k_2}\right)^3 - 1175\left(\frac{1}{1+k_2}\right)^2 - 6407\left(\frac{1}{1+k_2}\right) - 12814\right]\right] \times \left(\pi R_{max}{}^2_{BOR} \times L_{BOR}\right) \quad \text{(B.1)}$$

C

CODES

C.1. MATLAB CODES

The codes given in this section are the main post-processing codes used after saving the data by reading the MTFLOW/Fluent output files and storing the data in different matrices. The stored data are loaded directly from '.mat' files. The actual number of codes including the once made to automate the DSE and perform the optimization study are too many to be neatly included in the present report.

C.1.1. EULER-IBLT POST-PROCESSOR

The boundary layer file (xxxBL.mat) is the most important file that is used in post processing. Although, the inviscid data file (xxxIVF.mat) could also be loaded. The forces must be inserted in the source code directly or automated when necessary.

```
% MT pbm post
% Variable 'L' give the body (fuselage) length. Use variable 'tp_loc_a' to control the
% location of the trefftz plane accordingly

clear all
close all
clc

load('./flowres/esdurefBL.mat');    % Read boundary layer field saved data
load('./flowres/esdurefIVF.mat');   % Read inviscid field saved data (actually not necessary)
V_inf=2.425663513680329e+02;   % Freestream Velocity
rho=0.363007; % Ambient density
L=69;  % Fuselage length

tp_loc_a = 69;    % Location of trefftz plane (in global x coordinate)
sp_loc=0;         % Survey plance location (in global x coordinate)

% Interpolate all data  (Note that variables starting with caps have been multiplied with
%the local effective circumference for capturing the axis symmetry in calculation)

ybl=griddedInterpolant(sbl_data,ybl_data,'linear');            % radial coordinate
sbl=griddedInterpolant(xbl_data,sbl_data,'linear');            % arc length (local x coordinate)
ue_n=griddedInterpolant(sbl_data,ue_n_data,'linear');          % BL edge velocity
rhoe_n=griddedInterpolant(sbl_data,rhoe_n_data,'linear');      % BL edge mass density
cp=griddedInterpolant(sbl_data,cp_data,'linear');              % Pressure coefficient
deltastar=griddedInterpolant(sbl_data,deltastar_data,'linear'); % Displacement thickness
theta=griddedInterpolant(sbl_data,theta_data,'linear');         % Momentum thickness
thetastar=griddedInterpolant(sbl_data,thetastar_data,'linear'); % Kinetic energy thickness
Cfby2=griddedInterpolant(sbl_data,Cfby2_data,'linear');         % Local friction coefficient
CDisp=griddedInterpolant(sbl_data,CDisp_data,'linear');         % Local Dissipation coefficient
Theta=griddedInterpolant(sbl_data,Theta_data,'linear');         % Momentum thickness * b
Thetastar=griddedInterpolant(sbl_data,Thetastar_data,'linear'); % Kinetic energy thickness * b
Deltastarstar=griddedInterpolant(sbl_data,Deltastarstar_data,'linear'); % density-flux thickness * b

CN = -2.2799;             % force coefficient (drag coefficient as it is isolated body)
tp_loc = sbl(tp_loc_a);   % Location of trefftz plane (converted to local x coordinate)

Nf = (CN)*0.5*rho*(V_inf^2);  % Drag

NVinf=-Nf*V_inf;            % Drag power

% Wake power
E_dot =0.5*rho*rhoe_n([tp_loc])*((V_inf*ue_n([tp_loc]))^3)*...
((2*Theta([tp_loc]))-Thetastar([tp_loc])); %Wake power

% Dissipation
phi = (0.5*rho*rhoe_n([tp_loc])*((V_inf*ue_n([tp_loc]))^3)*...
(Thetastar([tp_loc])));  % Based on Kinetic energy thickness formula

phi_func = @(x) rho*rhoe_n([x])*((V_inf*ue_n([x]))^3)*...
(CDisp([x]))*(Theta([x])/((theta([x]))));   % Based on dissipation coefficient integration

phi2 = integral(phi_func,sp_loc,tp_loc,'ArrayValued',true);   % The integral value (phi)

pb=100*(E_dot+phi-NVinf)/NVinf;      % Power balance check (0 % is perfect balance)
```

C.1.2. RANS POST-PROCESSOR

```
% FLUENT post-processing for Dissipation analysis/Anergy analysis.

close all; clear all; clc;
load('./flowres/soldata.mat');  %Load solution data

%CV definition
bound{1}=[-200,0;-200,300];         % Survey plane before the aerodynamic body
bound{2}=[-200,300;69,300];         % Boundary defining the side cylinder
bound{3}=[69,0;69,300];             % Treffetz plane after the bli/non-bli body

% Interpolation to generate the whole mesh with the flow data
F_cfd = scatteredInterpolant(x_data,y_data,xvelocity_data,'linear','none'); % Interpolation function

F_Ux=F_cfd;       % Interpolated x velocity

F_cfd.Values=yvelocity_data; % Allows use of the interpolation function only once (to save time)
F_Uy=F_cfd;       % Interpolated y velocity

F_cfd.Values=pressure_data;
F_p=F_cfd;        % Interpolated pressure

F_cfd.Values=density_data;
F_rho=F_cfd;      % Interpolated density

F_cfd.Values=dubydx_data;
F_dubydx=F_cfd;      % Interpolated du by dx

F_cfd.Values=dvbydy_data;
F_dvbydy=F_cfd;    % Interpolated dv by dy

F_cfd.Values = dtbydx_data;
F_dtbydx = F_cfd;  % Interpolated dT by dx

F_cfd.Values = dtbydy_data;
F_dtbydy = F_cfd;  % Interpolated dT by dy

F_cfd.Values=tempr_data;
F_tempr=F_cfd;     % Interpolated static temperature

F_cfd.Values=entropy_data;
F_entropy=F_cfd;     % Interpolated entropy

F_cfd.Values=effk_data;
F_effk=F_cfd;     % Interpolated effective thermal conductivity

V_inf=2.425292439603934e+02;    % Freestream velocity
T_inf=2.287380000000000e+02;    % Freestream temperature
entropy_inf=-2.324235789000000e+02;         % Freestream entropy

% Dissipation analysis/Anergy analysis integrals

% Surface integrals calculation (TP outflows)

y_lim=bound{1,3}(2,2);
x_tp=bound{1,3}(1,1);

Ea_dot_part_func = @(y) 2*pi*y*(0.5*F_rho(x_tp,y)*((F_Ux(x_tp,y)-V_inf)^2)...
    *(F_Ux(x_tp,y))); % Axial kinetic energy deposition rate function

Ev_dot_part_func = @(y) 2*pi*y*(0.5*F_rho(x_tp,y)*(F_Uy(x_tp,y)^2)...
    *(F_Ux(x_tp,y))); % Normal kinetic energy deposition rate function

Ep_dot_part_func = @(y) 2*pi*y*(F_p(x_tp,y)*...
    (F_Ux(x_tp,y)-V_inf)); % Pressure defect energy deposition rate function

Ew_dot_part_func = @(x) 2*pi*y_lim*(F_p(x,y_lim) + (0.5*F_rho(x,y_lim)*...
    (((F_Ux(x,y_lim)-V_inf)^2)+(F_Uy(x,y_lim)^2)))))...
    *F_Uy(x,y_lim); % Shock wave energy outflow function

anergy_part_func = @(y) 2*pi*y*T_inf*(F_rho(x_tp,y)*(F_entropy(x_tp,y)-entropy_inf)*F_Ux(x_tp,y));

Ea_dot=integral(Ea_dot_part_func, bound{1,3}(1,2),...
    bound{1,3}(2,2), 'ArrayValued',true);  % Axial kinetic energy deposition rate
Ev_dot=integral(Ev_dot_part_func, bound{1,3}(1,2),...
    bound{1,3}(2,2), 'ArrayValued',true);  % Normal kinetic energy deposition rate
Ep_dot=integral(Ep_dot_part_func, bound{1,3}(1,2),...
    bound{1,3}(2,2), 'ArrayValued',true);  % Pressure defect energy deposition rate
Ew_dot=integral(Ew_dot_part_func, bound{1,2}(1,1),...
    bound{1,2}(2,1),'ArrayValued',true);  % Pressure volme work (Side of CV - significant if strong shocks exist)
anergy=integral(anergy_part_func, bound{1,3}(1,2),...
    bound{1,3}(2,2), 'ArrayValued',true);  % Anergy generation rate

PV_func = @(x,y) 2*pi*(F_p(x,y).*...
    (F_dubydx(x,y)+F_dvbydy(x,y)+(F_Uy(x,y)./y))).*y; % Pressure volume work function

[wall_x,indx]=sort(wall_x);
wall_y=wall_y(indx,:);
body_wall=spline(wall_x,wall_y);   % Interpolation of fuselage geometry

tanergy_func = @(x,y) 2*pi*(T_inf./(F_tempr(x,y).^2)).*...
    (F_effk(x,y).*((F_dtbydx(x,y).^2)+(F_dtbydy(x,y).^2))).*y;   % Thermal anergy function

% Volume integrals calculation
x_min= bound{1,1}(1,1);
x_max=bound{1,3}(1,1);
y_min1=bound{1,3}(1,2);
y_min2=@(x) ppval(body_wall,x);
y_max=bound{1,3}(2,2);

if x_max > max(wall_x)
    PV1 = integral2(PV_func,x_min,min(wall_x),y_min1,y_max,'AbsTol',0,'RelTol',1e-2);
    PV2 = integral2(PV_func,min(wall_x),max(wall_x),y_min2,y_max,'AbsTol',0,'RelTol',1e-2);
    PV3 = integral2(PV_func,max(wall_x),x_max,y_min1,y_max,'AbsTol',0,'RelTol',1e-2);
    PV = PV1+PV2+PV3; % Pressure volume work rate
    tanergy1 = integral2(tanergy_func,x_min,min(wall_x),y_min1,y_max,'AbsTol',0,'RelTol',1e-2);
    tanergy2 = integral2(tanergy_func,min(wall_x),max(wall_x),y_min2,y_max,'AbsTol',0,'RelTol',1e-2);
    tanergy3 = integral2(tanergy_func,max(wall_x),x_max,y_min1,y_max,'AbsTol',0,'RelTol',1e-2);
    tanergy = tanergy1+tanergy2+tanergy3; % Thermal anergy
elseif x_max < min(wall_x)
```

```
% Condition will not be used
else
    PV1 = integral2(PV_func,x_min,min(wall_x),y_min1,y_max,'AbsTol',0,'RelTol',1e−2);
    PV2 = integral2(PV_func,min(wall_x),max(wall_x),y_min2,y_max,'AbsTol',0,'RelTol',1e−2);
    PV = PV1+PV2; % Pressure volume work rate
    tanergy1 = integral2(tanergy_func,x_min,min(wall_x),y_min1,y_max,'AbsTol',0,'RelTol',1e−2);
    tanergy2 = integral2(tanergy_func,min(wall_x),max(wall_x),y_min2,y_max,'AbsTol',0,'RelTol',1e−2);
    tanergy = tanergy1+tanergy2; % Thermal anergy rate
end

E_dot = Ea_dot + Ev_dot + Ep_dot + Ew_dot;  % Mechanical energy outflow

NVinf=(0)∗V_inf; % Use only when required
```

C.2. UDF CODES IN C

This section lists the codes written in C programming language for forcing a propulsor model to achieve cruise condition in the RANS solver (Ansys Fluent). It should be noted that incompressible flows require only momentum sources for modeling the propulsor, whereas, compressible flows require momentum and the corresponding power source. The internal energy changes in compressible flow when adding momentum source and thus power source must be added to compensate for it.

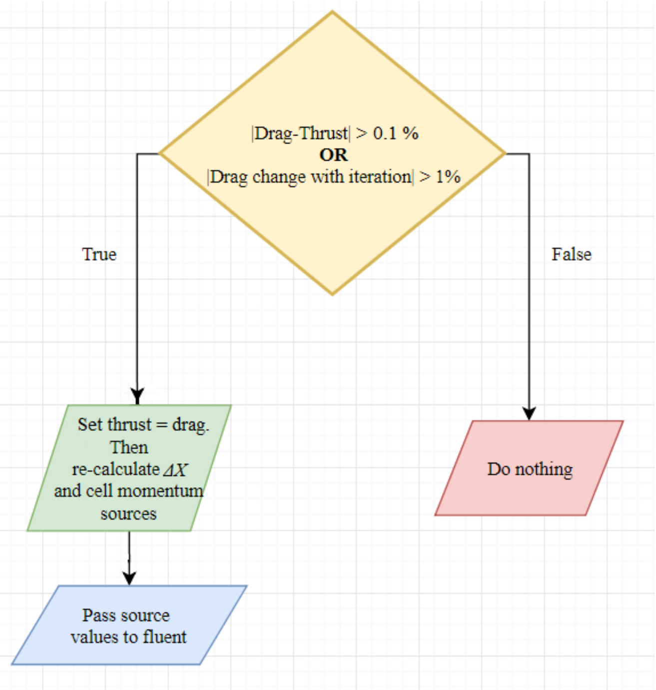

Figure C.1: Thrust-drag handling for x-momentum source values updating in UDF. Propulsor thrust is the total sum of the source values multiplied by the respective cell volumes. Drag value in Fluent is obtained by Riemann sum of pressure and viscous forces at the wall [25].

C.2.1. INCOMPRESSIBLE FLOW PROPULSOR UDF (AWF)

```
/*****************************************************************
  UDF for x−momentum source specification (Inompressible flow)
*****************************************************************/
// UDF used for Approximate wake filler (for cruise)

#include "udf.h"

#define LINESZ 100
#define v_inf 1.465700000000000
#define prop_inlet 1
#define cell1_lim 0.0005
#define n_r 49
#define rho 1.225

real U1_vals[100], P1_vals[100], source[5000], delta_x;

DEFINE_EXECUTE_AT_END(params)
{
    char buff[LINESZ];

    FILE ∗fptr;
    int line;
    int a[100000];
    real b[100000];
```

```

    real thrust, eflow, power, th_ver, sourcet;

    if (N_ITER <= 20) // Normal isolated body simulation for 20 iterations
    {
        thrust = 0;
        sourcet = 0;
        eflow = 0;
        power = 0;
        th_ver = 0;
    }

    if (N_ITER > 20)  // Propulsor effect starting after the 20th iteration
    {

        // Read drag file
        fptr = fopen("SomeDirectory/drag_force.out", "r+");
        line = 0;
        if (fptr != NULL)
        {
            while (fgets(buff, LINESZ, fptr))
            {
                line = line + 1;
                if (line > 3)
                {
                    sscanf(buff, "%d %lf", &a[line], &b[line]);
                }
            }
        }
        fclose(fptr);
        // Reading file done

        // For reading cells in a zone
        real x[ND_ND];
        Domain *domain = Get_Domain(1);
        int Cell_Zone_ID = 2;
        cell_t c;
        Thread *t = Lookup_Thread(domain, Cell_Zone_ID);
        // cell vars declared

        if ((fabs(b[line] - thrust) / b[line] > 0.001) || (fabs(b[line] - b[line - 1]) / b[line - 1] > 0.01))
        {
            Message("sourcet: %.16lf \n", sourcet);
            Message("drag: %.16lf \n", b[line]);
            Message("thrust: %.16lf \n", thrust);
            Message("th_ver: %.16lf \n", th_ver);
            Message("delta_x: %.16lf \n", delta_x);
            Message("ppower: %.16lf \n", power);
            Message("eflow: %.16lf \n", eflow);
            Message("error: %.16lf \n", fabs(b[line] - thrust) / b[line]);

            // Extract cell data
            begin_c_loop(c, t)
            {
                C_CENTROID(x, c, t);
                if (x[0] - prop_inlet < cell1_lim)
                {
                    U1_vals[c] = C_U(c, t);  // Axial velocity in the cell
                    P1_vals[c] = C_P(c, t);  // Static pressure in the cell
                }
            }
            end_c_loop(c, t)

            thrust = b[line];
            eflow = 0;  // Total energy flow at the propulsor entry cells
            th_ver = 0; // For verifying thrust value
            sourcet = 0; // Total source (ignore)
            power = 0;   // Engine power

            begin_c_loop(c, t)
            {
                eflow = eflow + ((C_VOLUME(c, t))*(-P1_vals[c % n_r] + ((rho*((v_inf*v_inf) - \
                    (U1_vals[c % n_r] * U1_vals[c % n_r]))) / 2))); // Total energy flow at the propulsor entry cells

                C_CENTROID(x, c, t);
                if (N_ITER == 29)
                {
                    Message("%d %g %g %g %g %g\n", c, x[0], x[1], U1_vals[c % n_r], P1_vals[c % n_r], source[c]); //For verification
                }
            }
            end_c_loop(c, t)

            delta_x = eflow/thrust;  // The delta_x value obtained from thrust and energy flow

            begin_c_loop(c, t)
            {
                source[c] = -((P1_vals[c % n_r])/(delta_x)) + ((rho*((v_inf*v_inf) \
                    - (U1_vals[c % n_r] * U1_vals[c % n_r]))) / (2 * delta_x));  // Actual source value per cell (same in a horizontal layer)

                th_ver = th_ver + ((C_VOLUME(c, t))*(-((P1_vals[c % n_r]) / (delta_x)) \
                    + ((rho*((v_inf*v_inf) - (U1_vals[c % n_r] * U1_vals[c % n_r]))) / (2 * delta_x))));

                sourcet = sourcet - ((P1_vals[c % n_r]) / (delta_x)) + ((rho*((v_inf*v_inf) \
                    - (U1_vals[c % n_r] * U1_vals[c % n_r]))) / (2 * delta_x));

                power = power + (((C_VOLUME(c, t))*(-((P1_vals[c % n_r]) / (delta_x)) \+ ((rho*((v_inf*v_inf) \
                    - (U1_vals[c % n_r] * U1_vals[c % n_r]))) / (2 * delta_x))))*C_U(c, t));
            }
            end_c_loop(c, t)
        }

        else
        {
            Message("sourcet: %.16lf \n", sourcet);
            Message("drag: %.16lf \n", b[line]);
            Message("thrust: %.16lf \n", thrust);
            Message("th_ver: %.16lf \n", th_ver);
            Message("delta_x: %.16lf \n", delta_x);
            Message("ppower: %.16lf \n", power);
            Message("eflow: %.16lf \n", eflow);
            Message("error: %.16lf \n", fabs(b[line] - thrust) / b[line]);
        }
```

```
    }
}

DEFINE_SOURCE(xmom_source, c, t, dS, eqn) // Add momentum source per cell
{
    return source[c];
}
```

C.2.2. COMPRESSIBLE FLOW PROPULSOR UDF (FUSELAGE)

```
/**********************************************************************
   UDF for x-momentum and energy source specification (Compressible flow)
**********************************************************************/
// UDF used for fuselage propulsor simulations (for cruise)

#include "udf.h"

#define LINESZ 100
#define pi 3.141592653589793238462643383279
real xmom, pows, powsa;

DEFINE_EXECUTE_AT_END(source_support)
{
    char buff[LINESZ];

    FILE *fptr;
    int line;
    int a[100000];
    real b[100000];
    real thrust, power, E_volume = 0;

    if (N_ITER <= 20)
    {
        thrust = 0;
        xmom = 0;
        power = 0;
        pows = 0;
    }

    if (N_ITER > 20)
    {
        // Read drag file
        fptr = fopen("SomeDirectory/drag_force.out", "r+"); // Location of Drag file output directory
        line = 0;
        if (fptr != NULL)
        {
            while (fgets(buff, LINESZ, fptr))
            {
                line = line + 1;
                if (line > 3)
                {
                    sscanf(buff, "%d %lf", &a[line], &b[line]);
                }
            }
        }
        fclose(fptr);
        // Reading file done

        // Variable declarations for looping through cells
        Domain *domain = Get_Domain(1); /* declare domain pointer since it is not passed as an argument to the DEFINE macro */
        int Cell_Zone_ID = 2;  //Needs the correct id of the engine cell zone
        cell_t c;
        Thread *t = Lookup_Thread(domain, Cell_Zone_ID);
        // end of declarations

        begin_c_loop(c, t)
        {
            E_volume = E_volume + (2 * pi * C_VOLUME(c, t)); //Engine volume (for verification)
        }
        end_c_loop(c, t)

        // Assignment of source values
        if ((fabs(b[line] - thrust) / b[line] > 0.001) || (fabs(b[line] - b[line - 1]) / b[line - 1] > 0.01))
        {
            thrust = b[line];  // Assigning thrust=drag
            xmom = thrust / E_volume;   // x-momentum source
            power = 0;
            begin_c_loop(c, t)
            {
                power = power + (xmom * 2 * pi * C_VOLUME(c, t) * C_U(c, t)); // Total engine power
            }
            end_c_loop(c, t)
            pows = power / E_volume;
            Message("%.16lf \n", E_volume);
            Message("%.16lf \n", xmom);
            Message("%.16lf \n", thrust);
            Message("%.16lf \n", pows);
            Message("%.16lf \n", power);
            Message("%.16lf \n", (b[line] - thrust) / b[line]);
        }

        else
        {
            power = 0;
            begin_c_loop(c, t)
            {
                power = power + (xmom * 2 * pi * C_VOLUME(c, t) * C_U(c, t));  // Total engine power
            }
            end_c_loop(c, t)
            pows = power / E_volume;
            Message("%.16lf \n", xmom);
            Message("%.16lf \n", thrust);
            Message("%.16lf \n", pows);
            Message("%.16lf \n", power);
            Message("%.16lf \n", (b[line] - thrust) / b[line]);
        }
    }
```

```c
}

DEFINE_SOURCE(xmom_source, c, t, dS, eqn)  // Add x-momentum source
{
    //dS[eqn] = ; //Add slope value for stablity
    return xmom;
}

DEFINE_SOURCE(pows_source, c, t, dS, eqn)  // Add power source
{
    if (C_U(c, t) >= 0)
    {
        powsa = xmom * C_U(c, t);
    }
    else
    {
        powsa = 0;
    }
    return powsa;
}
```

BIBLIOGRAPHY

[1] Drela, M., "Power Balance in Aerodynamic Flows," *AIAA Journal*, Vol. 47, No. 7, 2009, pp. 1761–1771.

[2] Arntz, A., Atinault, O., and Merlen, A., "Exergy-Based Formulation for Aircraft Aeropropulsive Performance Assessment: Theoretical Development," *AIAA Journal*, Vol. 53, No. 6, 2014, pp. 1627–1639.

[3] Ashcraft, S. W., Padron, A. S., Pascioni, K. A., Stout Jr, G. W., and Huff, D. L., "Review of propulsion technologies for N+3 subsonic vehicle concepts," *NASA technical memorandum*, 2011.

[4] Lv, P., Rao, A. G., Ragni, D., and Veldhuis, L., "Performance Analysis of Wake and Boundary-Layer Ingestion for Aircraft Design," *Journal of Aircraft*, Vol. 53, No. 5, 2016, pp. 1517–1526.

[5] Smith, L. H., "Wake ingestion propulsion benefit," *Journal of Propulsion and Power*, Vol. 9, No. 1, 1993, pp. 74–82.

[6] Hall, D. K., Huang, A. C., Uranga, A., Greitzer, E. M., Drela, M., and Sato, S., "Boundary Layer Ingestion Propulsion Benefit for Transport Aircraft," *Journal of Propulsion and Power*, Vol. 33, No. 5, 2017, pp. 1118–1129.

[7] Lv, P., and Rao, A. G., "Conceptual Analysis of Boundary-Layer Ingestion Towards Aircraft Propulsion Integration," *ISABE conference*, 2013.

[8] Kim, H., and Felder, J., "Control Volume Analysis of Boundary Layer Ingesting Propulsion Systems With or Without Shock Wave Ahead of the Inlet," *49th AIAA Aerospace Sciences Meeting including the New Horizons Forum and Aerospace Exposition*, 2011.

[9] Lv, P., Ragni, D., Hartuc, T., Veldhuis, L., and Rao, A. G., "Experimental Investigation of the Flow Mechanisms Associated with a Wake-Ingesting Propulsor," *AIAA Journal*, Vol. 55, No. 4, 2016, pp. 1332–1342.

[10] Uranga, A., Drela, M., Greitzer, E. M., Hall, D. K., Titchener, N. A., Lieu, M. K., Siu, N. M., Casses, C., Huang, A. C., Gatlin, G. M., and Hannon, J. A., "Boundary Layer Ingestion Benefit of the D8 Transport Aircraft," *AIAA Journal*, Vol. 55, No. 11, 2017, pp. 3693–3708.

[11] Carrier, G., Atinault, O., Grenon, R., and Verbecke, C., "Numerical and experimental aerodynamic investigations of boundary layer ingestion for improving propulsion efficiency of future air transport," *31st AIAA Applied Aerodynamics Conference*, 2013, p. 2406.

[12] Sabo, K. M., and Drela, M., "Benefits of Boundary Layer Ingestion Propulsion," *53rd AIAA Aerospace Sciences Meeting*, American Institute of Aeronautics and Astronautics, 2015.

[13] Gray, J. S., Mader, C. A., Kenway, G. K., and Martins, J., "Approach to modeling boundary layer ingestion using a fully coupled propulsion-RANS model," *58th AIAA/ASCE/AHS/ASC Structures, Structural Dynamics, and Materials Conference*, 2017.

[14] Elmiligui, A. A., Fredericks, W. J., Guynn, M. D., and Campbell, R. L., "Numerical investigation of a fuselage boundary layer ingestion propulsion concept," , 2013.

[15] Blumenthal, B., Elmiligui, A. A., Geiselhart, K., Campbell, R. L., Maughmer, M. D., and Schmitz, S., "Computational Investigation of a Boundary Layer Ingestion Propulsion System for the Common Research Model," *46th AIAA Fluid Dynamics Conference*, 2016, p. 3812.

[16] Kenway, G. K., and Kiris, C. C., "Aerodynamic Shape Optimization of the STARC-ABL Concept for Minimal Inlet Distortion," *2018 AIAA/ASCE/AHS/ASC Structures, Structural Dynamics, and Materials Conference*, 2018.

[17] Chappell, P., Clarke, A., and Porter, R., "Geometrical characteristics of typical bodies," *IHS ESDU*, Vol. 77028, 1977.

[18] Petrusson, A., "Aerodynamic Evaluation of Nacelles for Engines with Ultra High Bypass Ratio," Thesis (M.Sc.), Chalmers University of Technology, 2017.

[19] Arntz, A., and Atinault, O., "Exergy-Based Performance Assessment of a Blended Wing–Body with Boundary-Layer Ingestion," *AIAA Journal*, Vol. 53, No. 12, 2015, pp. 3766–3776.

[20] Drela, M., "Two-dimensional transonic aerodynamic design and analysis using the Euler equations," Thesis (Ph.D.), Massachusetts Institute of Technology, 1986.

[21] Drela, M., "A User's Guide to MTFLOW 2.01," , 2010.

[22] Isikveren, A. T., Seitz, A., Bijewitz, J., Mirzoyan, A., Isyanov, A., Grenon, R., Atinault, O., Godard, J. L., and Stückl, S., "Distributed propulsion and ultra-high by-pass rotor study at aircraft level," *The Aeronautical Journal*, Vol. 119, No. 1221, 2015, pp. 1327–1376.

[23] Cengel, Y. A., and Boles, M. A., *Thermodynamics: an engineering approach*, Tata McGraw-Hill Education, 2005.

[24] Moore, J., and Moore, J. G., "Entropy production rates from viscous flow calculations: part I—A turbulent boundary layer flow," *ASME 1983 International Gas Turbine Conference and Exhibit*, American Society of Mechanical Engineers, 1983, pp. V001T01A032–V001T01A032.

[25] ANSYS, "ANSYS FLUENT 12.0 User's Guide," 2009.

[26] Ferziger, J. H., and Peric, M., *Computational methods for fluid dynamics*, Springer Science & Business Media, 2012.

[27] Gatski, T. B., and Bonnet, J.-P., *Chapter 3 - Compressible turbulent flow*, Elsevier, 2009, pp. 39–77.

[28] Grasch, A. D., "Design of a model propulsor for a boundary layer ingesting aircraft," Thesis (M.Sc.), Massachusetts Institute of Technology, 2013.

[29] Swafford, T. W., "Analytical approximation of two-dimensional separated turbulent boundary-layer velocity profiles," *AIAA Journal*, Vol. 21, No. 6, 1983, pp. 923–926.

[30] Hanson, C. J., "Integrated lifting-surface and Euler/boundary-layer theory analysis method for marine propulsors," Thesis (M.Sc.), Massachusetts Institute of Technology, 2001.

[31] Van Ingen, J., "The e^N method for transition prediction. Historical review of work at TU Delft," *38th Fluid Dynamics Conference and Exhibit*, 2008, p. 3830.

[32] Drela, M., and Youngren, H., "XFOIL 6.9 User Primer," , 2001.

[33] Cengel, Y. A., *Fluid mechanics*, Tata McGraw-Hill Education, 2010.

[34] Anderson Jr, J. D., *Fundamentals of aerodynamics*, Tata McGraw-Hill Education, 2010.

[35] Mathworks, "MATLAB 2018b documentation," , 2018.

[36] Ku, H. H., "Notes on the use of propagation of error formulas," *Journal of Research of the National Bureau of Standards*, Vol. 70, No. 4, 1966.

[37] Stokkermans, T., Van Arnhem, N., and Veldhuis, L., "Mitigation of propeller kinetic energy losses with boundary layer ingestion and swirl recovery vanes," *Proceedings of the 2016 Applied Aerodynamics Research Conference*, 2016.

[38] Squire, H. B., and Young, A. D., *The calculation of the profile drag of aerofoils*, HSMO, 1937.

[39] Sato, S., "The power balance method for aerodynamic performance assessment," Thesis (Ph.D.), Massachusetts Institute of Technology, 2012.

[40] Menter, F. R., "Two-equation eddy-viscosity turbulence models for engineering applications," *AIAA Journal*, Vol. 32, No. 8, 1994, pp. 1598–1605.

[41] Spalart, P. R., and Rumsey, C. L., "Effective Inflow Conditions for Turbulence Models in Aerodynamic Calculations," *AIAA Journal*, Vol. 45, No. 10, 2007, pp. 2544–2553.

[42] Chappell, P. D., "Profile drag of axisymmetric bodies at zero incidence for subcritical Mach numbers," *IHS ESDU*, Vol. 78019, 1978.

[43] Kulfan, B. M., "Universal Parametric Geometry Representation Method," *Journal of Aircraft*, Vol. 45, No. 1, 2008, pp. 142–158.

[44] Whitfield, D. L., and Jameson, A., "Euler equation simulation of propeller-wing interaction in transonicflow," *Journal of Aircraft*, Vol. 21, No. 11, 1984, pp. 835–839.

[45] Stokkermans, T. C., Arnhem, N. v., Sinnige, T., and Veldhuis, L. L., "Validation and Comparison of RANS Propeller Modeling Methods for Tip-Mounted Applications," *2018 AIAA Aerospace Sciences Meeting*, 2018, p. 0542.

[46] Roskam, J., *Airplane Design: Preliminary configuration design and integration of the propulsion system*, Vol. 1, DARcorporation, 1985.

[47] Drela, M., "Development of the D8 Transport Configuration," *29th AIAA Applied Aerodynamics Conference*, 2011.

[48] NASA, "U.S. Standard Atmosphere," Report, 1976.

[49] Hicks, R. M., Vanderplaats, G. N., Murman, E. M., and Ames Research, C., "An assessment of airfoil design by numerical optimization," *NASA technical memorandum ; NASA TM X-3092*, 1974.

[50] Hicks, R. M., and Henne, P. A., "Wing Design by Numerical Optimization," *Journal of Aircraft*, Vol. 15, No. 7, 1978, pp. 407–412.

[51] Skinner, S. N., and Zare-Behtash, H., "State-of-the-art in aerodynamic shape optimisation methods," *Applied Soft Computing*, Vol. 62, 2018, pp. 933–962.

[52] Pironneau, O., *Optimal shape design for elliptic systems*, System Modeling and Optimization, Springer Berlin Heidelberg, 1982, pp. 42–66.

[53] Jameson, A., "Aerodynamic shape optimization using the adjoint method," *Lectures at the Von Karman Institute, Brussels*, 2003.

[54] Wolpert, D. H., and Macready, W. G., "No free lunch theorems for optimization," *IEEE Transactions on Evolutionary Computation*, Vol. 1, No. 1, 1997, pp. 67–82.

[55] DeGraaff, D. B., Webster, D. R., and Eaton, J. K., "The effect of Reynolds number on boundary layer turbulence," *Experimental Thermal and Fluid Science*, Vol. 18, No. 4, 1998, pp. 341–346.